

POLITECNICO DI TORINO

Master's Degree in Electronic Engineering



**Politecnico
di Torino**

Master's Degree Thesis

**Analysis and design of EMI filters for
innovative electrified agricultural
machinery**

Supervisor

Prof. Francesco Musolino

Co-Supervisor

Dr. Gianluca Botto

Candidate

Angelo Carnazzo

December 2021

Acknowledgements

In primis, dedico dei ringraziamenti sinceri, e non di circostanza, al prof. Musolino, da cui ho imparato moltissimo durante questo lavoro di tesi e di cui ho ammirato la passione e la dedizione per il proprio lavoro.

Allo stesso modo ringrazio Luca e Gianluca di FLAG, che mi hanno seguito mettendo a disposizione la loro infinita disponibilità. Vi auguro di realizzare tutte le vostre ambizioni.

Ringrazio la mia Famiglia, non esistono strumenti per misurare l'amore incondizionato che mi hanno dato. Tutto ciò che ho fatto, e che farò, esiste solo grazie a voi. Grazie anche ai ragazzi del primo piano, tra chi è passato e chi è presente, sono stato felicissimo di aver condiviso con voi questa parte della mia vita e vi porterò sempre con me.

Un ringraziamento speciale alla divisione E&E di Squadra Corse, è stata un'esperienza pazzesca, mi ha insegnato tantissimo e la ricorderò sempre con felicità e malinconia.

Infine, ma non per importanza, un ringraziamento ai miei amici terroni che, nonostante il tempo e la distanza, ho sempre sentito vicino a me.

Sono stati degli anni fantastici e spero di avervi dato almeno la metà di quello che mi avete dato voi.

Table of Contents

- List of Tables VIII

- List of Figures IX

- Acronyms XIII

- 1 Introduction** **1**

- 2 Electromagnetic compatibility** **5**
 - 2.1 Line impedance stabilization network 7
 - 2.2 Regulation E-ECE-324-Add.9-Rev.6 9
 - 2.2.1 LISN specifications 9
 - 2.2.2 Measurement setup 10
 - 2.2.3 Spectrum analyzer setup 11
 - 2.2.4 Emission limits 13
 - 2.3 Conducted emissions in switching devices 13
 - 2.3.1 Rectangular waveform spectrum 14
 - 2.3.2 Trapezoidal waveform spectrum 14
 - 2.4 Conducted emissions in AC motor drivers 16
 - 2.4.1 Characteristic issues 16
 - 2.4.2 Cable couplings 17
 - 2.4.3 Current paths 18

- 3 System overview** **21**
 - 3.1 Inverters 21
 - 3.1.1 Space vector pulse width modulation 25
 - 3.1.2 Tedder inverter 26
 - 3.1.3 Ditcher inverter 30
 - 3.2 Electrical motors 32

4	Basic system model	37
4.1	SVPWM model	38
4.2	Motor and control data	39
4.3	Ideal inverter model	41
4.4	Solver configurations	43
4.5	Spectrum analyzer configurations	45
5	Advanced system model	49
5.1	Elimination of initial transient	49
5.2	Choice of the MOSFET model	51
5.3	Contribution of PCB traces	53
5.4	Cables model	56
5.4.1	Cables effect	62
5.5	Worst case analysis	67
5.5.1	Motor speed	67
5.5.2	Carrier frequency	67
5.5.3	Shields grounding	70
5.5.4	Line sections	70
5.5.5	Sampling rate	72
6	Simulation of the systems	75
6.1	Carriers phase shift	75
6.2	Distance between cables	81
6.3	Final model setup	81
6.4	DM emission on time domain	88
6.5	Model of the ditcher system	90
7	Design of EMI filters	93
7.1	Topology	93
7.1.1	Review of basic magnetics	95
7.1.2	Common-mode choke	96
7.1.3	X and Y capacitors	98
7.2	Stability	99
7.3	Components selection	102
7.4	Equivalent model of filter components	105
7.5	Model validation	108
7.6	Some considerations on how mounting the EMI filter	113
8	Conclusions and outlooks	117
A	Tedder data definition	119

B Tedder system model	125
C Ditcher data definiton	135
D Ditcher system model	141
Bibliography	145

List of Tables

2.1	Normative LISN parameters.	10
2.2	Conducted emission measurement setup legend.	11
2.3	Spectrum analyzer parameters.	13
2.4	Maximum allowed radio frequency conducted disturbances on DC power lines.	13
3.1	Dc-link capacitor main parameters [8].	28
3.2	SiC MOSFET main parameters [11].	30
3.3	SiC power module main parameters [15].	32
3.4	Tedder and ditcher PMSM main parameters.	35
5.1	Equivalent inductances of drain and source of SiC MOSFET [11].	51
5.2	Power cables main geometry parameters [21].	57
5.3	Power cables main electrical parameters.	58
5.4	Number of line sections for each power cable.	59
5.5	Results of PUL cables model parameters.	61
5.6	Values used for motor speed tuning.	67
6.1	Phase shift of the carriers.	78
7.1	Solutions proposed for the selection of the common-mode choke.	103
7.2	ESR and ESL of the X and Y capacitors.	107

List of Figures

2.1	Electromagnetic emission frequency bands defined by EMC standards [1].	6
2.2	LISN measurement setup.	7
2.3	LISN circuit.	8
2.4	DM and CM currents in a LISN measurement.	9
2.5	Normative HV-AN schematic [2].	10
2.6	Conducted emission measurement setup [2].	11
2.7	Spectrum analyser scheme [4].	12
2.8	Spectrum envelope of single rectangular pulse [1].	15
2.9	Spectrum envelope of trapezoidal waveform.	15
2.10	Per-unit-length MTL.	17
2.11	DM current paths at motor side of a frequency converter [1].	19
2.12	CM current paths at motor side of a frequency converter [1].	19
3.1	Generic three-phase voltage sourced inverter.	22
3.2	Switching power pole [5].	23
3.3	Classic pulse width modulator.	24
3.4	The eight basic space vectors with their magnitude and direction [6].	27
3.5	Concept scheme of the tedder system quadruple configuration.	28
3.6	Dc-link capacitor impedance versus frequency [8].	29
3.7	Gate driving of a MOSFET [14].	31
3.8	SiC power module [15].	31
3.9	Rotating machines classification.	33
3.10	Per phase PMSM stator equivalent circuit.	34
4.1	SVPWM modulating voltages.	39
4.2	SVPWM unitary switching function of the first leg.	39
4.3	Three-phase stator equivalent circuit.	40
4.4	Implementation of ideal inverter model.	42
4.5	Configurations of the ideal switch block.	42
4.6	Time-domain behavior of the basic model.	43

4.7	Block diagram of the basic model including SVPWM, inverter, LISNs, and PMSM	44
4.8	Effect of the overlap on LISN measurement.	46
4.9	Effect of the windowing on LISN measurement.	47
4.10	Effect of the number of averages on LISN measurement.	48
5.1	Precharge of the capacitor blocks.	50
5.2	Transient effect on line-to-line and LISN voltages.	50
5.3	Schematic of the MOSFET models comparison.	51
5.4	Parameters of N-channel MOSFET [11].	53
5.5	Behavior of <i>Ideal</i> and <i>N-channel</i> MOSFET output voltages.	54
5.6	Insertion of MOSFET and gate driver models in inverter model.	54
5.7	Comparison of <i>Ideal</i> and <i>N-channel</i> MOSFETs on the LISN measurement.	55
5.8	Insertion of PCB traces parasitics on the inverter model.	55
5.9	Effect of the PCB traces parasitics on the LISN measurement.	56
5.10	Typical cross section of power cables [22].	57
5.11	Power cables disposition.	58
5.12	DC side cables and their parasitic elements.	60
5.13	Parameters of <i>Transmission Line</i> block.	62
5.14	Effect of cables model on voltage measured at motor terminals.	63
5.15	Effect of DC cables and ESL on the DM current path.	63
5.16	Separation of the DM and CM emission spectra.	64
5.17	Effect of cables model and dc-link capacitor ESL on the DM emission measurement.	64
5.18	Effect of dc-link capacitor ESL value on the DM emission.	65
5.19	DM and CM emissions including cables model and dc-link capacitor ESL.	66
5.20	LISN measurement including cables model and dc-link capacitor ESL.	66
5.21	Effect of the motor speed on positive envelope of the DM and CM emissions.	68
5.22	Effect of the switching frequency on positive envelope of the DM and CM emissions.	69
5.23	Effect of the connection between shield and reference on the DM and CM emissions.	71
5.24	Effect of the line section length on the DM and CM emissions.	72
5.25	Effect of the solver sample rate on the DM and CM emissions.	73
6.1	Comparison of the DM and CM emissions between single and quadruple configurations.	76

6.2	Three parallel inverters with common supply and driving a common induction motor [26].	77
6.3	Generic carrier signals for a) symmetric interleaving, b) regular asymmetric interleaving and c) irregular asymmetric interleaving [26].	78
6.4	Emission comparison between no phase shift and a,b) Symmetric shift, c,d) Symmetric shift "in pairs" and e,f) Asymmetric shift. . . .	79
6.5	Comparison between symmetric and asymmetric phase shift on the DM and CM emissions.	80
6.6	Effect of the distance between cables on the DM and CM emissions.	82
6.7	Measurement setup with the insertion of the insulator and enclosures.	83
6.8	Effect of the insulating support and device enclosures on the DM and CM emissions.	86
6.9	LISN measurement of the tedder system.	87
6.10	Effect of the distance between cable shields and inverter case on the CM spectrum.	87
6.11	Effect of the shield connection to DC- instead of inverter case on the DM and CM emissions.	88
6.12	DM emission and its peaks.	89
6.13	Behavior of "U" phase voltage and input current.	89
6.14	Model of the ditcher inverter.	90
6.15	Stray inductance of the SiC power module.	91
6.16	DM and CM emissions measured on ditcher system.	92
6.17	LISN measurement on ditcher system.	92
7.1	Insertion loss required for DM and CM emissions.	94
7.2	Generic typical EMI filter topology.	94
7.3	Inductor geometry [34].	95
7.4	Modeling the effect of a CMC on (a) the currents of a two-wire line, (b) the DM components, and (c) the CM components[3].	97
7.5	Power-line filter showing the leakage inductance of the common-mode choke [30].	98
7.6	Parallel damped filter	101
7.7	Series damped filter	101
7.8	Simulation setup for the measurement of the filter output impedance.	102
7.9	Effect of the parallel damping on the output impedance of an ideal filter.	102
7.10	3D view of the CM-161U-60A common-mode choke.	104
7.11	Equivalent circuit of a common mode choke.	106
7.12	Setup for the measurement of the CMC impedance.	107
7.13	CM-161U-60A impedance measured with $R_{core} = 800 \text{ k}\Omega$	108
7.14	One stage EMI filter with input capacitors.	108

7.15	Setting parameters for the CMC model.	109
7.16	LISN measurements without and with a one-stage filter.	110
7.17	Model of the two stages EMI filter.	110
7.18	Comparison between the LISN measurement without filter and with a two stage filter.	111
7.19	Setup for the EMI filter characterization in DM (left) and CM (right).111	
7.20	Comparison of the DM insertion losses measured on a generic 50 Ω /50 Ω system.	112
7.21	Comparison of the CM insertion losses measured on a generic 50 Ω /50 Ω system.	112
7.22	LISN measurements without and with two-stage filter on ditcher system.	113
7.23	EMI filter mounting and grounding improperly (left) and properly (right) [30].	114
7.24	Effect of the improper grounding of the Y capacitors.	115
B.1	Model of the tedder system.	125
B.2	SVPWM algorithm.	126
B.3	LISN schematic.	127
B.4	DC cables model.	128
B.5	DC cables line section.	129
B.6	EMI filter schematic.	130
B.7	Single inverter system model.	131
B.8	Single inverter model.	132
B.9	Three-phase cables model.	133
B.10	Three-phase cables line section.	134
D.1	Model of the ditcher system.	141
D.2	Inverter model.	142
D.3	Three-phase cables model.	143

Acronyms

AC Alternating Current

ASD Adjustable Speed Driver

BEV Electrical Vehicle

CISPR Comité International Spécial des Perturbations Radioélectriques

CM Common-Mode

CMC Common-Mode Choke

CSI Current Sourced Inverter

DC Direct Current

DM Differential-Mode

DUT Device Under Test

ECE Economic Commission for Europe

EMC Electromagnetic Compatibility

EMI Electromagnetic Interference

ESA Electronic Sub-Assembly

FFT Fast Fourier Transform

HV-AN High Voltage Artificial Network

ICEV Internal Combustion Engine Vehicle

IEC International Electrotechnical Commission

IF Intermediate Frequency

LISN Line Impedance Stabilization Network

LF Low-Frequency

MEP Measurement Port

MTL Multiple Transmission Line

MVDC Medium Voltage Direct Current

PCB Printed Circuit Board

PMSM Permanent Magnet Synchronous Motor

PUL Per-Unit-Length

PWM Pulse Width Modulation

RBW Resolution Bandwidth

RF Radio-Frequency

RMS Root-Mean-Square

SA Spectrum Analyzer

SMD Surface Mounted Device

SMPC Switch-Mode Power Converter

SMPS Switch-Mode Power Supply

SOC State Of Charge

ST Sweep Time

THD Total Harmonic Distortion

TL Transmission Line

TEM Transverse Electromagnetic

UN United Nations

VSI Voltage Sourced Inverter

Chapter 1

Introduction

A crucial need for today's society is the development of sustainable machinery through electrically operated machines and equipment. The environmental impact of machinery powered by fossil fuels is increasingly evident and is the cause of public debate. Adding the concern about the imminent end of these resources, the need to find alternatives becomes a common primary, especially in the automotive sector.

MARcEL project

Accordingly, the MARcEL project falls into the field of agricultural electrification to develop a fully integrated system, consisting of a tractor equipped with a generation unit and a series of fully electrically operated equipment. The project intends to develop the technologies for the control of motors and electric actuators, the architectures dedicated to the integration between the machines and the relative sensors, the preparation of the tractor, the generation system, and data acquisition systems. The MARcEL project adopts some of the key elements of the Horizon 2020 and Horizon Europe 2027 programs, in particular concerning sustainable agriculture and energy efficiency. Considering the strong interest in this type of product and the strong competitiveness that will arise from it in the next few years, the results obtained with the MARcEL project will have very important repercussions. The project involves 17 partners including leading companies in the production of tractors, engines, agricultural machinery, the DET (Department of Electronics and Telecommunications) of the Polytechnic of Turin, and the DISAFA (Department of Agricultural, Forestry and Food Sciences) of the University of Turin.

The agricultural machinery realized in the project is of different types. The implemented low voltage machinery, such as a straddle sprayer, a leveler, and a sheeter, use a 48V battery and they don't require a power electronic unit to drive

them. The maximum power involved is experimentally evaluated between 4.5 kW and 6.5 kW . On the other side, the high voltage machinery, the ones covered in this thesis work, operate with a 700 V supply, and custom inverters have been designed to drive the electric motors. In particular, these machinery are:

- A ditchers: the maximum power involved is around 47 kW in excavation mode and 40 kW in cleaning mode.
- A tedder: the maximum power involved is around 25 kW in normal conditions and 48 kW in "extreme" conditions.

The motors designed for these applications are driven by two voltage-sourced three-phase inverters, realized by FLAG-MS. They will be classified during this thesis as "ditcher inverter" and "tedder inverter": the first one is a single high power inverter while the second one is composed of four low power inverters put together to drive four separate Permanent Magnet Synchronous Motors (PMSMs). In general, these inverters belong to the so-called ditcher and tedder systems.

Thesis work

These inverters, as every electric or electronic device, to be properly marketed, must ensure its Electromagnetic Compatibility (EMC) with the surrounding environment and must comply with the reference normative regarding its emission limits. This thesis work is focused on the conducted emissions of these inverters, defined for frequency below 30 MHz . Switching devices like three-phase inverters are based on fast switching of power electronic switches, to decrease switching time and loss. Nevertheless, these solutions usually increase potential EM emissions. In addition to this, conducted emission on Adjustable Speed Drives (ASDs) is influenced by large parasitic capacitances and inductances and AC motor feeding cables [1]. The normative used in this thesis work is regulation number 10 of the Economic Commission for Europe of the United Nations (UN/ECE), which provides the uniform provisions concerning the approval of vehicles with regards to EMC [2]. The normative specifies a measurement setup to be used for the evaluation of the conducted emission of the Device Under Test (DUT), which must stay below an emission limit. To satisfy the EMC criteria, several design rules can be employed on both the emitter and receiver sides. Nevertheless, these techniques are often not enough to comply with the regulation, especially in switch-mode circuits where the spectral content is very large. In this case, the insertion of one or more Electromagnetic Interference (EMI) filters is mandatory.

The goal of this thesis is to design the EMI filters to place at the input of the inverters so that the requirements of the normative are satisfied. This design must be performed by predicting the conducted emission level of the system when placed on the measurement setup specified by the normative. First, the EMC theory is

explained, with particular attention to the typical sources of conducted emissions in the ASDs and illustrating the normative specifications. Second, the analysis is focused on the tedder and ditcher systems, including the three-phase inverters and the PMSMs, and provides all the information needed to understand the system design. Third, to correctly predict the conducted emission of the devices, it is necessary to realize a model of the measurement setup. The model is realized using the *Simscape* tool available on Simulink environment for each ditcher and tedder system. The model has been refined modeling the modulation technique, the stator, a detailed model of the inverters with real switching waveforms, the DC and three-phase cables with the Multiple Transmission Line (MTL) theory, and the final measurement setup, including all the parasitic contributes due to the physical implementation. The model is supported by a MATLAB script which allows establishing the operating point of the system. The conducted emission spectrum, found in the worst condition of the system in terms of EMC, allows predicting the Insertion Loss (IL) required by the filter. Finally, the filter has been designed starting from the required IL and defining the filter topology and components. The filter has been validated on both tedder and ditcher models, providing some mounting indication to ensure its correct behavior.

Chapter 2

Electromagnetic compatibility

One of the key aspects when designing any electronic system or equipment regards the necessity to ensure its electromagnetic compatibility with the surrounding environment. In fact, the unwanted generation of electromagnetic waves, typically rich in spectral content, can cause interference or noise on itself or with other devices. By definition [3], a system is electromagnetically compatible with its environment if it satisfies the following three criteria:

- It does not cause interference with other systems;
- It does not cause interference with itself;
- It is not susceptible to emission coming from other systems.

Any electronic device must comply with the reference legislation regarding its emission limits, otherwise it cannot be placed on the market. In order to satisfy the EMC criteria, several design rules can be employed both on the emitter and the receiver side. For example:

- The first solution is by increasing the rise/fall times of voltages and currents of the emitter. However, as far as switching power converters are considered, large fall and rise times also provides a large power dissipation during switch, causing an efficiency decreasing on the system and, sometimes, cooling issues.
- An alternative solution is to act directly on the device that is susceptible to EM noise by putting a metal enclosure around the receptor. The amount of emission reduction depend upon the material used, its thickness and the frequency of the EM fields to be shielded. This technique is very effective against radiated emissions but it is typically quite expensive.

- The previous techniques are often not enough to comply with the regulation, especially in switch-mode circuits where the spectral content is very large. In this case, the insertion of one or more EMI filters is mandatory. Of course, it adds both weight and volume and thus also overall cost.

According to the current standard definitions, electromagnetic emissions are classified into four categories based on two characteristic frequency ranges, as shown in Figure 2.1. The frequency range above 9 kHz has been established as Radio Frequencies (RF) and most of EMC issues localized in this range are identified as Electromagnetic Interference (EMI). The second range categorizes EMC phenomena for conducted emission below 30 MHz and radiated emission above 30 MHz. This split is based on the assumption that, very often, unintended emission occurs for frequencies lower than 30 MHz and the predominant part of electromagnetic energy is transferred via cable connections or other conductive components. Above 30 MHz, instead, the dominating part of electromagnetic energy is propagated through space in the form of electromagnetic waves.

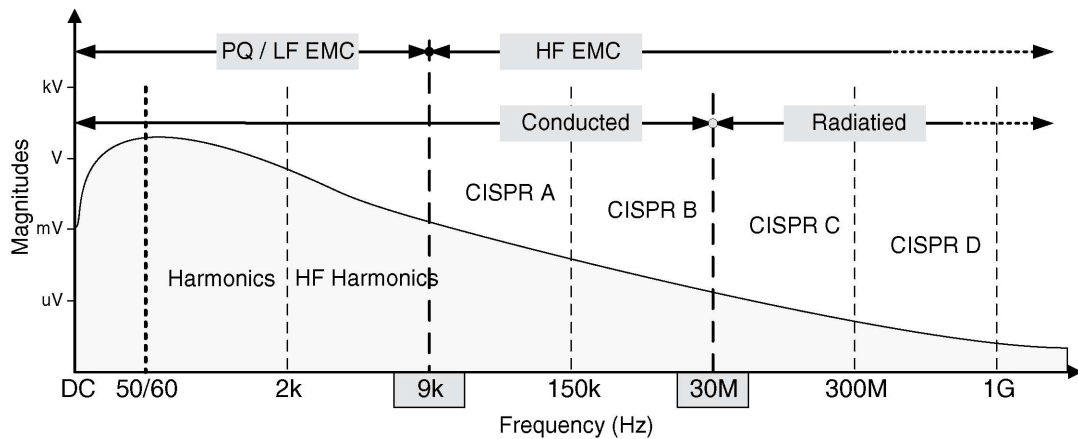


Figure 2.1: Electromagnetic emission frequency bands defined by EMC standards [1].

As noted above, regulatory agencies impose limits on conducted emissions because they superimpose on power system nets, the so-called power grids. In fact, in typical commercial and domestic applications the power distribution system can be seen as a large array of wires connecting the various power outlets together, from which each electronic system in the installation receives its power. The power distribution network represents a large antenna from which these conducted emissions can radiate quite efficiently, possibly causing interference to other systems.

2.1 Line impedance stabilization network

The intent of the conducted emission normative is to limit the noise current through the product's supply cables, which flow on the common power net of the installation, producing interference. The test has to be carried out by inserting a Line Impedance Stabilization Network (LISN) in series with the power cord of the product. The LISN measurement setup on the power cables is shown in Figure 2.2. The LISN must be inserted between the the Device Under Test (DUT) and the power supply. Furthermore, it has an output port which provides the noise measurement to a receiver, typically a Spectrum Analyzer (SA), which allow to evaluate the spectral content of the conducted emission.

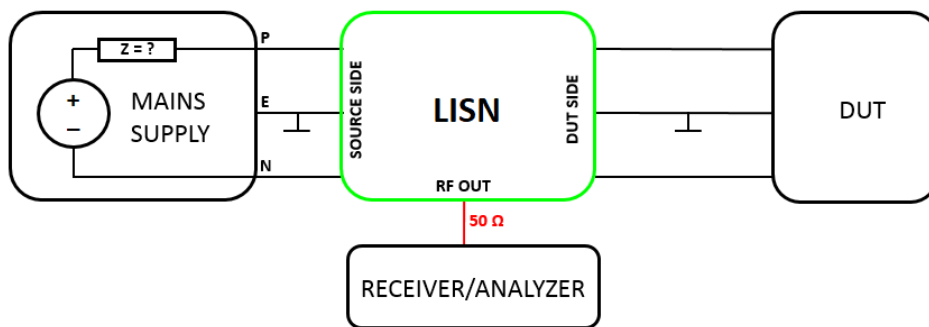


Figure 2.2: LISN measurement setup.

The LISN circuit, shown in the Figure 2.3, has the following purpose:

- The first is to prevent external noise to the test from contaminating the measurement, blocking conducted emissions that are not due to the product being tested. The inductor L and capacitor C_2 are placed to provide an high impedance at RF noise while allowing the Low Frequency (LF) power to flow through to the EUT, ensuring the correct nominal operation of the device.
- The second purpose of the LISN is to ensure that the measurement is independent on the measurement site, assuming that the impedance seen can vary from site to site. In order to do this, the LISN presents a constant impedance within the measurement frequency range, independently from the installation site. The capacitor C_1 prevents any dc from overloading the test receiver, while R is used to make a discharge path for C_1 in the event that the test receiver is disconnected.

Summarizing, the impedance seen between conductors and reference by DUT is essentially 50Ω , which represents the standard input impedance of the spectrum analyzer or the generic receiver that is used to make the measurement.

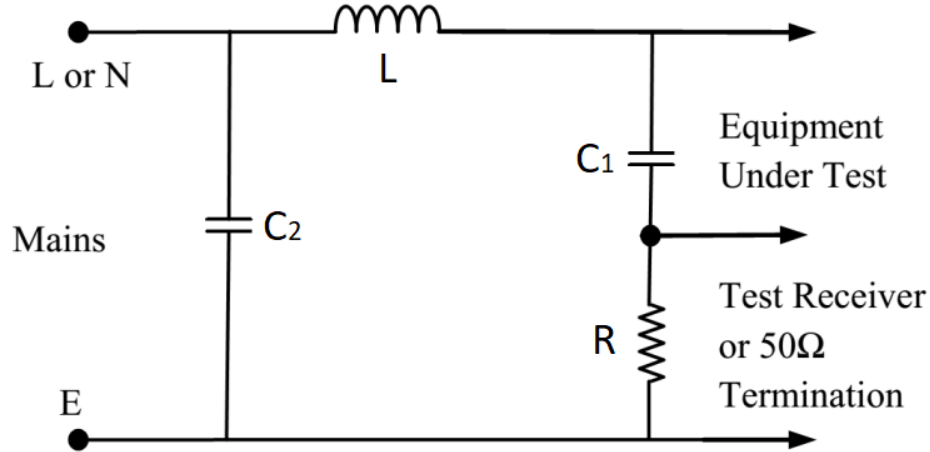


Figure 2.3: LISN circuit.

At this point, it is useful to differentiate the current contributions in overall conduction emission. In fact, in every three-conductor system the current can be decomposed into Differential-Mode (DM) and Common-Mode (CM). Figure 2.4 shows the contributions of DM and CM current components on the measured conducted emissions with the equivalent model of a LISN within the interest frequency band. The DM current is the intended current and it is part of the nominal behavior of the DUT. It is simply given by:

$$I_D = \frac{1}{2} (I_P - I_N) \quad (2.1)$$

The CM current, instead, is an unintentional current that may not be seen looking only at the functional schematic. It is mathematically given by:

$$I_C = \frac{1}{2} (I_P + I_N) \quad (2.2)$$

As a consequence, the measured voltages at the LISN terminals are:

$$\begin{aligned} V_P &= 50 (I_C + I_D) \\ V_N &= 50 (I_C - I_D) \end{aligned} \quad (2.3)$$

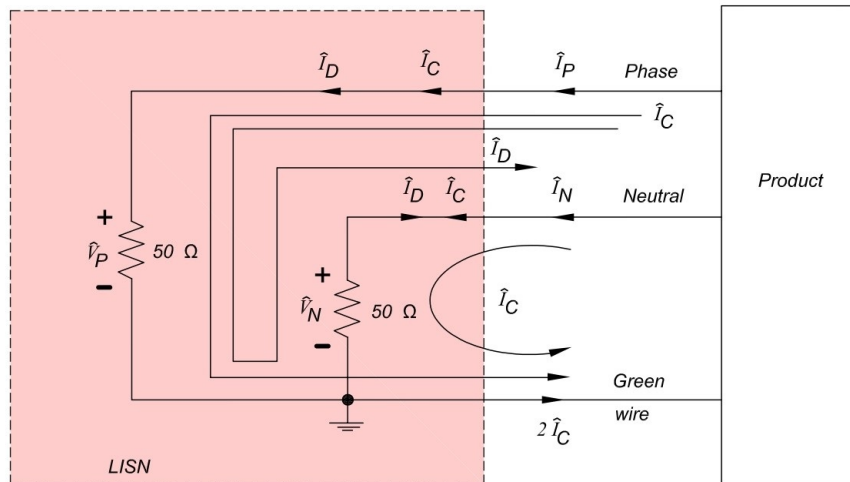


Figure 2.4: DM and CM currents in a LISN measurement.

2.2 Regulation E-ECE-324-Add.9-Rev.6

The UN regulations have made EMC a critical aspect in the marketability of every electronic product, since if the product does not comply with specific limits about emissions, it cannot be sold. In 1933, a meeting of the International Electrotechnical Commission (IEC) in Paris has formed the International Special Committee on Radio Interference (CISPR) to face up the problem of EMI.

The reference normative used in this thesis work is the regulation number 10 of the Economic Commission for Europe of the United Nations (UN/ECE), which provides the uniform provisions concerning the approval of vehicles with regard to EMC [2]. The section of normative under interest regards the specifications about radio frequency conducted emission on DC power lines from Electric/Electronic Sub-Assembly (ESA). The ESA is a device intended to be part of a vehicle, together with the associated electrical connections and wirings, which performs one or more specialized functions. Below, the main information about the emission limits and measurement setup constrains are reported.

2.2.1 LISN specifications

It was previously seen that the conducted emission measurement has to be performed by using a LISN, or the so-called High Voltage Artificial Network (HV-AN). The normative imposes to use a $5 \mu H$ and 50Ω HV-AN as shown in Figure 2.5, where

MEP indicates the Measurement Port. The two HV-ANs, one on the positive and one on the negative conductor, shall be mounted directly on the ground plane. In

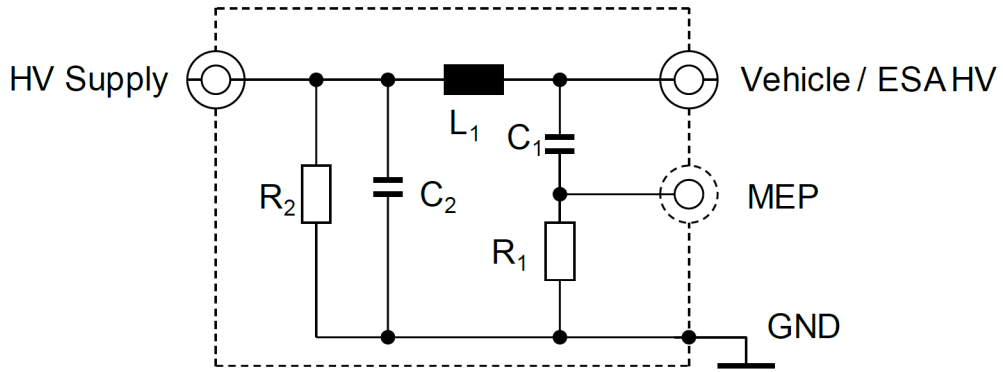


Figure 2.5: Normative HV-AN schematic [2].

particular, the component values have been reported in Table 2.1.

Component	Value
L_1	$5 \mu H$
C_1	$0.1 \mu F$
C_2	$1 \mu F$
R_1	$1 k\Omega$
R_2	$1 M\Omega$

Table 2.1: Normative LISN parameters.

2.2.2 Measurement setup

The emission test is intended to measure the level of radio frequency conducted disturbances generated by ESA through its AC or DC power lines in order to ensure it is compatible with residential, commercial and light industrial environments. The test shall be performed according to CISPR 16-2-1, which provides specification for radio disturbances and immunity measuring apparatus and methods. The complete test setup for the connection of the ESA is shown in Figure 2.6. The corresponding legend is reported in Table 2.2.

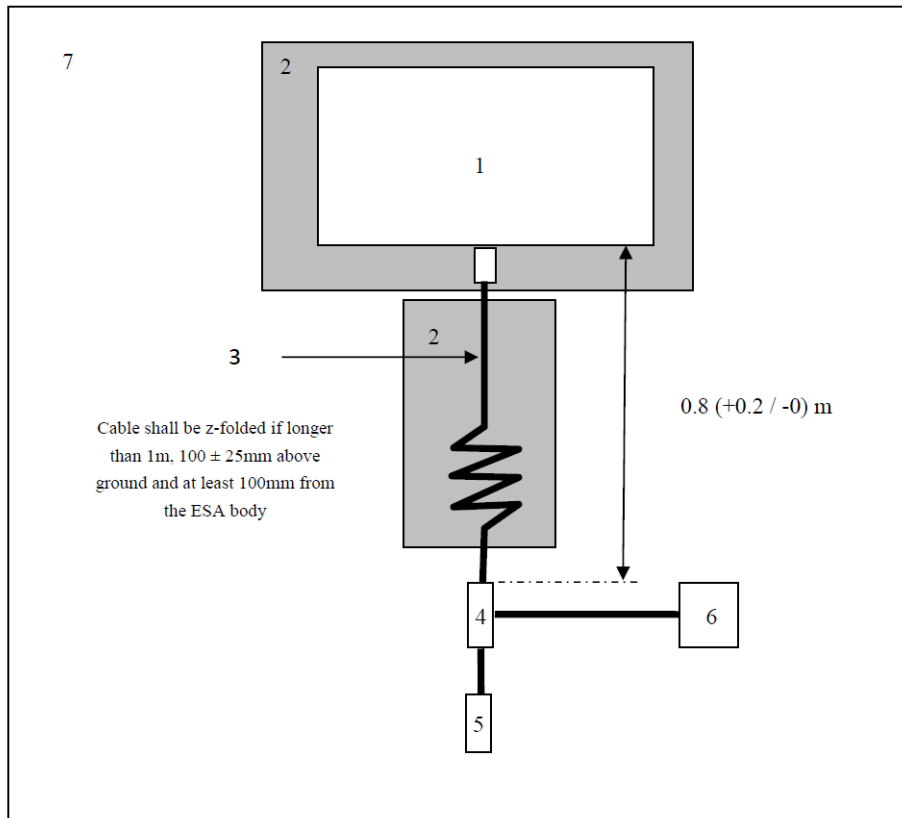


Figure 2.6: Conducted emission measurement setup [2].

Number	Description
1	ESA under test
2	Insulating support
3	Charging harness
4	LISN grounded
5	Power mains socket
6	Measuring receiver
7	Ground plane

Table 2.2: Conducted emission measurement setup legend.

2.2.3 Spectrum analyzer setup

The measurements shall be performed with a Spectrum Analyser (SA) or a scanning receiver, as long as in both cases the tests have to be done in the frequency range between 150 kHz and 30 MHz.

The complete scheme of a classical SA is shown in Figure 2.7. The frequency

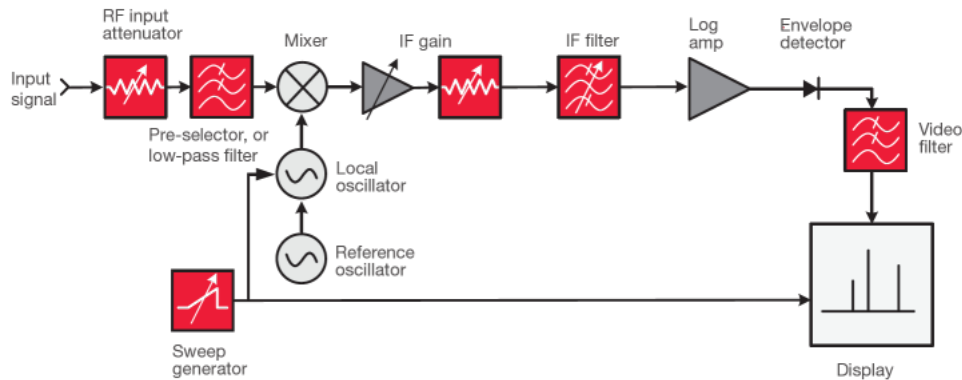


Figure 2.7: Spectrum analyser scheme [4].

scan of a SA is typically performed by a mixer and a narrow band filter, which central frequency is called Intermediate Frequency (IF). Ideally, a mixer works as a multiplier and at the output of a mixer we have two sinusoidal signals at $f_{RF} + f_{LO}$ and $f_{RF} - f_{LO}$. In particular, the Resolution Bandwidth (RBW) is defined as the frequency span of the IF filter that is applied to the input signal. Smaller RBW provides finer frequency resolution and more ability to differentiate signals that have frequencies that are closer together. However, it is closely related to the Sweep Time (ST), which is the length of time that SA takes to sweep the detector from the start to the stop frequency:

$$ST = \frac{k \cdot \text{Span}}{RBW^2} \quad (2.4)$$

For filters used in many analog analyzers, the value of k is in the 2 to 3 range. Furthermore, the sample detection can be done with different detector types:

- Peak detection: the easiest way to ensure that all signals are reported properly is to display the maximum value measured in each bucket. Peak is the default mode offered on many spectrum analyzers because it ensures that no sinusoid is missed.
- Quasi-peak detection is a weighted form of peak detection. The measured value of the quasi-peak detection drops as the repetition rate of the measured signal decreases.
- An averaging detector acts averaging the linear voltage data of the envelope signal measured during the bucket interval.

The parameters to be set on the Spectrum Analyzer are defined in Table 2.3.

Peak detector		Quasi-peak detector		Average detector	
RBW at -3 dB	Minimum scan time	RBW at -6 dB	Minimum scan time	RBW at -3 dB	Minimum scan time
9/10 kHz	10 s/MHz	9 kHz	200 s/MHz	9/10 kHz	10 s/MHz

Table 2.3: Spectrum analyzer parameters.

2.2.4 Emission limits

Finally, let's look at the emission limits of radio frequency conducted disturbances on DC power lines from ESA imposed by the current normative. If measurements are made using the method described in previous sections, the limits on DC power lines are those defined in IEC 61000-6-3 and reported in Table 2.4.

Frequency [MHz]	Limits and detector
0.15 to 0.5	79 dBuV (quasi-peak) 66 dBuV (average)
0.5 to 30	73 dBuV (quasi-peak) 60 dBuV (average)

Table 2.4: Maximum allowed radio frequency conducted disturbances on DC power lines.

2.3 Conducted emissions in switching devices

Switch-Mode Power Converter (SMPC) are based on fast switching of power electronics switches that allows controlling averaged values of voltages and currents easily with much higher efficiency than linear regulators. Various methods are used to decrease switching losses for the given switching duration, based on appropriate shaping of voltage and current waveforms during switching process [1]. Nevertheless, all these solutions usually result in increase of time derivatives of voltages and currents. From EMC point of view, any voltage and current arising in SMPC results in potential electromagnetic emission that has to be maintained within normative limits. This interdependence imposes to find a tradeoff between converter's efficiency and electromagnetic emission during the SMPC design.

The determination of spectrum contents of voltage and current switching waveforms allows to predict emission levels and evaluate influence of switching shapes on expected spectra content. Unfortunately, the real switching waveforms change in switching devices typically used in contemporary converters. For this reason, the following analysis will include the most common and simple cases.

2.3.1 Rectangular waveform spectrum

Fourier transform of a periodic rectangular waveform allows to determine magnitudes c_k and angle coefficient θ_k of its spectrum in function of the amplitude $X(k)$ of individual harmonic:

$$x(t) = c_0 + \sum_{k=1}^{\infty} c_k \cdot \cos\left(k \frac{2\pi}{T} t + \theta_k\right) \quad (2.5)$$

where:

$$\begin{aligned} c_k &= |X(k)| \\ \theta_k &= \angle X(k) \end{aligned} \quad (2.6)$$

The magnitude envelope of spectral components c_n for a rectangular waveform can be formulated using the sinc function:

$$|c_n| = V_{DC} \frac{t_{on}}{T} \left| \frac{\sin(n\pi t_{on} f_1)}{n\pi t_{on} f_1} \right| \quad (2.7)$$

where $f_1 = 1/T$ is the frequency of the rectangular waveform and t_{on} is the time period in which the waveform is at the high value. Analytic calculation of Fourier transform, even for simplified switch-mode waveforms like the one of rectangular shape, is rather complex. However, the properties of sinc function significantly simplify determination of the envelope, which is most essential for EMC analysis:

$$|\text{sinc}(x)| = \left| \frac{\sin(x)}{x} \right| \leq \begin{cases} 1, & \text{for } x \ll 1 \\ \frac{1}{|x|}, & \text{for } x \gg 1 \end{cases} \quad (2.8)$$

Using this upper boundary representation, the resulting spectrum envelope is the one shown in Figure 2.8. By looking at this result, it follows that

- Magnitude of spectrum components generally follows the form of $\sin(x)/x$ function;
- Zero spectrum amplitudes will occur for frequencies equal to multiples of $f_{on} = n/t_{on}$.
- Maximum values of these bounds can be enveloped by the asymptote $1/x$, which slop is -20 dB per decade.

2.3.2 Trapezoidal waveform spectrum

For a more accurate analysis, trapezoidal approximations of switching waveforms is used, since it consider also switch-on and switch-off times, which are essential in

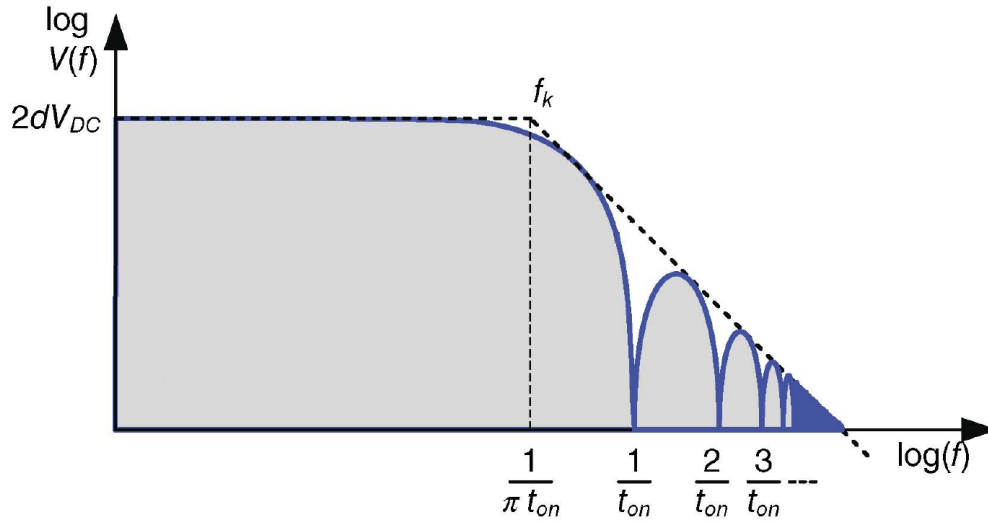


Figure 2.8: Spectrum envelope of single rectangular pulse [1].

spectrum analysis. Making the same procedure as before and supposing equal rise and fall times, the formula for estimation of trapezoidal waveform spectra envelope is:

$$|c_n| = 2V_{DC} \frac{t_{on}}{T} \left| \frac{\sin(n\pi t_{on} f_1)}{n\pi t_{on} f_1} \right| \left| \frac{\sin(n\pi t_r f_1)}{n\pi t_r f_1} \right| \quad (2.9)$$

Supposing instead different rise and fall times, a graphical representation of trapezoidal waveform spectrum envelope is shown in Figure 2.9. The figure suggests

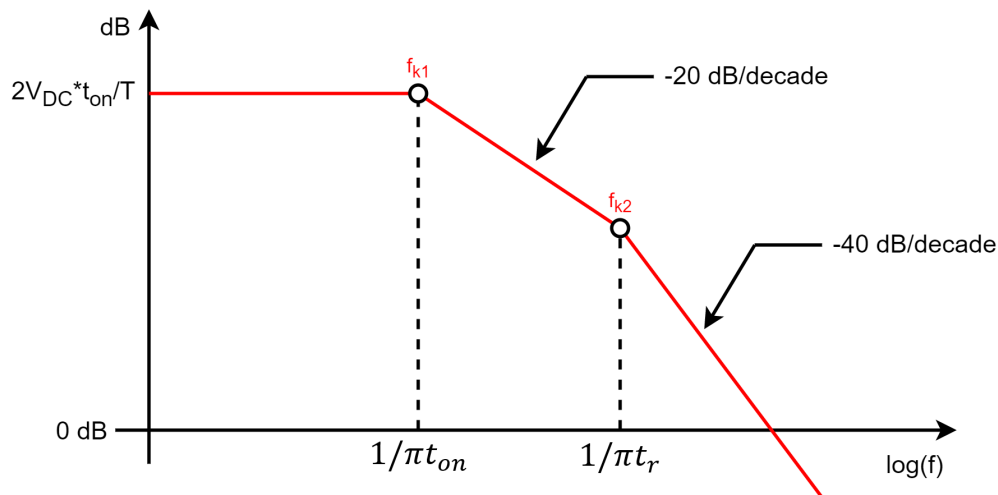


Figure 2.9: Spectrum envelope of trapezoidal waveform.

that the shape of the trapezoidal envelope is the same of the rectangular one plus a contribute due to the not null rise and fall times, which provides benefits on spectral content since allows a decreasing of -40 dB slope. This result confirms one important propriety mentioned above: using large rise/fall times allows to decrease the spectral content of these switching waveforms and then also of the overall emissions.

2.4 Conducted emissions in AC motor drivers

One of the topic points concerns the analysis of emission source in the application considered in this thesis work, namely what is called an Adjustable Speed Driver (ASD). ASDs, consisting of AC motors and Voltage Sourced Inverters (VSI) controlled by Pulse Width Modulation (PWM) patterns, are one of the most critical cases from the EMC point of view.

2.4.1 Characteristic issues

In recent years, the total power of ASD used in commercial and industrial applications has been increased a lot, resulting in commutation at high DC voltages and in increased generation of conducted emission. In addition to this, currently used semiconductor switches commute in shorter and shorter times, by decreasing switching losses and by using higher modulation carrier frequencies. Also, high power transistors exhibit relatively large parasitic capacitances between substrate and reference plane, resulting in significant increase of conducted emission generation and propagation [1].

Subsequently, the EM influence of AC motor feeding cables is not typically considered at the design stage, because it is widely dependent on requirements of singular application. The physical length of feeding cables is usually comparable to the wavelength of transmitted harmonic components, resulting in effective propagation of generated conducted emission toward other adjacent systems. High levels of CM currents at converter's output caused by wire-to-ground parasitic capacitances have a strong influence on the emission spectrum and sometimes they can damage the motor. Also, there are several ASD applications functioning successfully without any output filtering applied. Since the motor cables are very often placed along other power cables, there is the creation of a propagation path that enables efficient coupling toward power system, bypassing converter input EMI filters [1].

2.4.2 Cable couplings

One of the main problems of this analysis refers to the unintended EM coupling between wires or Printed Circuit Board (PCB) lands that are in close proximity. In particular, the source and receptor of the electromagnetic emission are within the same system and this reflects the third concern in EMC: the design of the product such that it does not interfere with itself. If the coupling occurs to the power cord of the product, it may cause to fail the conducted emission regulatory requirements.

This analysis is based on Multiconductor Transmission Lines (MTL) concept, which is the extension of the two-conductors line into a three or more conductors case, which takes into account the presence of two conductor wires above a reference. The main assumption on the MTL analysis is the Transverse Electromagnetic (TEM) mode of propagation of field present on the lines. Under this assumption, the electric and magnetic fields do not have a component along the line axis. To predict the crosstalk effect, it is possible to construct a PUL equivalent circuit for a Δz section, as shown in Figure 2.10. The generator and receptor circuits have PUL

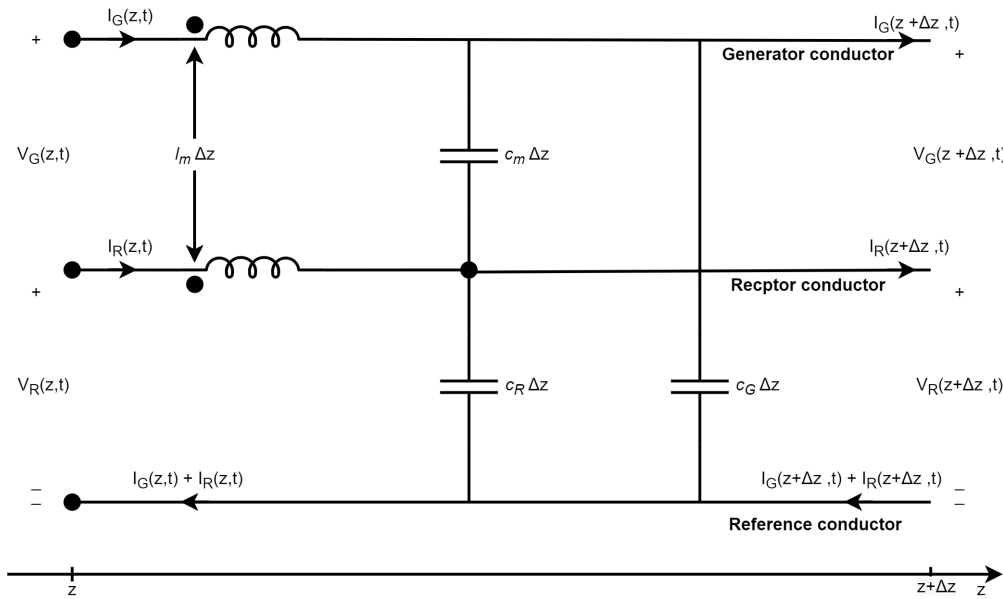


Figure 2.10: Per-unit-length MTL.

self inductances l_G and l_R , respectively, and a PUL mutual inductance l_m between them. The inductive coupling is due to the magnetic flux generated by the current flowing on the first conductor, which generates a current on the second one via Faraday’s law, and vice versa. On the other side, the PUL self capacitances between the generator/receptor and the reference conductor are represented by c_G and c_R ,

respectively, while the PUL mutual capacitance between the generator and receptor conductors is represented by C_m . Capacitive coupling is due to charges produced by line voltages on the conductors, that generate electric fields between each pair of conductors.

One of the typical methods for reducing this parasitic effect is by using shielded wire for generator and/or receptor. In particular, on this work shielded cables are used for both power supply and three-phase sides. A shielded cable can include one or more conductors enclosed by a common conductive layer. The shield acts as a Faraday cage to reduce EMI with other cables or devices. One of the main constraints is that the shield must be grounded to be effective, otherwise a floating shield provides no protection against interference. Subsequently, it will be shown how to compute the capacitive and inductive coupling elements as a function of type of wire and their distance, highlighting their impact on the LISN emission measurement.

2.4.3 Current paths

Differential mode output currents of a VSI can be divided into two spectral components: low frequency DM currents and high frequency DM currents. Low frequency DM current components flow through the entire length of the motor windings, generate motor torque at different rotor speeds and are the fundamental functionality of power conversion in AC motor drives. High frequency components flowing in AC motor, instead, are induced by high-speed voltage changes produced by inverter during switching transients and are shunted by parasitic capacitances of motor feeding cable. A graphical distribution of high-frequency DM current paths in a typical ASD application is represented in Figure 2.11.

Low frequency CM currents are very low and are typically neglected. High frequency CM currents, instead, are induced by high-speed voltage changes between converter's terminals and the reference. These CM parasitic capacitances are usually significantly higher than corresponding wire-to-wire DM capacitances. Furthermore, CM currents in relation to DM ones can be potentially more disturbing and its flow paths are more difficult to predict and control. An example of CM currents distribution in typical ASD application is presented in Figure 2.12. Note that, in the example shown, a single shield is used for all three-phase conductors: this is not the case that will be presented later for the thesis work, where each conductor has its own shield.

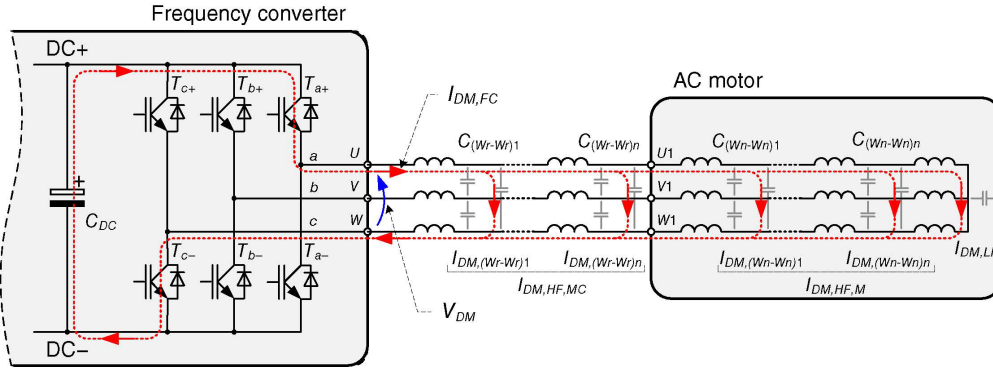


Figure 2.11: DM current paths at motor side of a frequency converter [1].

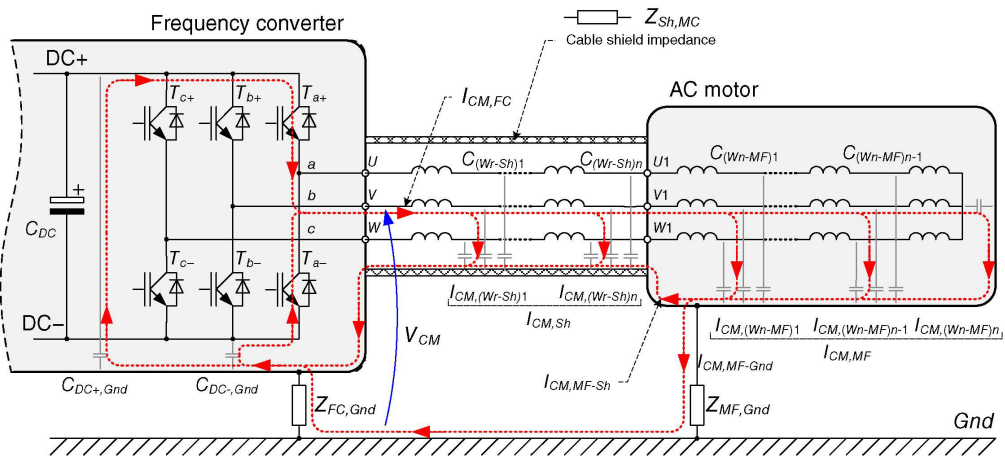


Figure 2.12: CM current paths at motor side of a frequency converter [1].

Chapter 3

System overview

This chapter aims to present the electronic and electrical devices that will be included in the implemented model. More precisely, the LISN measurement is performed on a system that includes the inverter(s), the power cables on both DC and three-phase sides, and the electric motor of both tedder and ditcher applications. The inverters and the motors will be analyzed starting from their objective up to the definition of the components, while the power cables will be shown and modeled in the next section.

3.1 Inverters

An inverter allows converting a DC input voltage into an AC output voltage. More precisely, they convert a DC voltage to a sequence of rectangular AC pulses, which is non-sinusoidal and hence has a high harmonic content. To do this, it works in the so-called "switching mode" thanks to the action of its switching devices. The main advantage of this kind of operation is the high efficiency, since only passive and switching devices are used, instead of resistive or dissipative ones.

It is useful to provide a classification of the inverter based on its structure or function. Both the ditcher and tedder inverters have the following characteristics:

- Three-phase inverters: three different outputs shifted by 120° each other.
- Voltage Sourced Inverters (VSI): the DC input is a constant voltage and the energy is stored on a parallel DC bus capacitor. The alternative configuration is the Current Sourced Inverter (CSI), which is not employed in this work.
- A Space Vector Pulse Width Modulation (SVPWM) is employed to control both amplitude and frequency of the output AC voltage by a specific modulation scheme.

The generic topology of this kind of inverters is shown in Figure 3.1 and it includes an ideal battery, which provides the constant DC power at the input. Nevertheless, a dc-link capacitor is always needed to provide a more stable DC voltage, limiting fluctuations of the heavy current demanded by the inverter. Good dc-link capacitors should have low Equivalent Series Inductance (ESL), very low Equivalent Series Resistance (ESR), and high ripple current tolerance. The DC power is then provided to the three legs of the inverter, which define three switching nodes of the inverter (U,V,W), highlighted in red in Figure 3.1. The three output voltages, instead, are defined as line-to-line voltages and are given by the difference between the outputs of each leg.

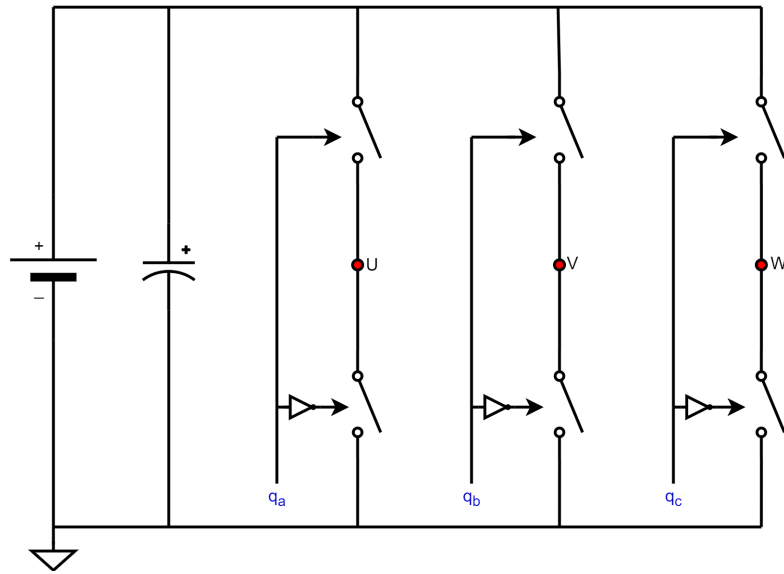


Figure 3.1: Generic three-phase voltage sourced inverter.

Each leg is composed of a switching power pole, whose concept schematic is represented in Figure 3.2. The practical implementation of a bi-positional switch is done with two switches and two free-wheeling diodes. In MOSFETs, these diodes are the so-called body diode, intrinsically present due to the construction, while in IGBT they have to be externally added. The switch's position is controlled by the so-called unitary switching function q_a , which can be seen as an ON/OFF command. Looking at Figure 3.2, when q_a is high, then the top switch is ON and the bottom switch is OFF, and then the output voltage is $V_{AN} = V_d$. If the command q_a is low, instead, the behavior of the switches is the opposite and the output is $V_{AN} = 0$. In other words, the instantaneous output of each leg is related to the command signal as:

$$V_{an}(t) = V_d \cdot q_a(t) \quad (3.1)$$

Since q_a is an ON/OFF command, the output voltage has a square wave shape,

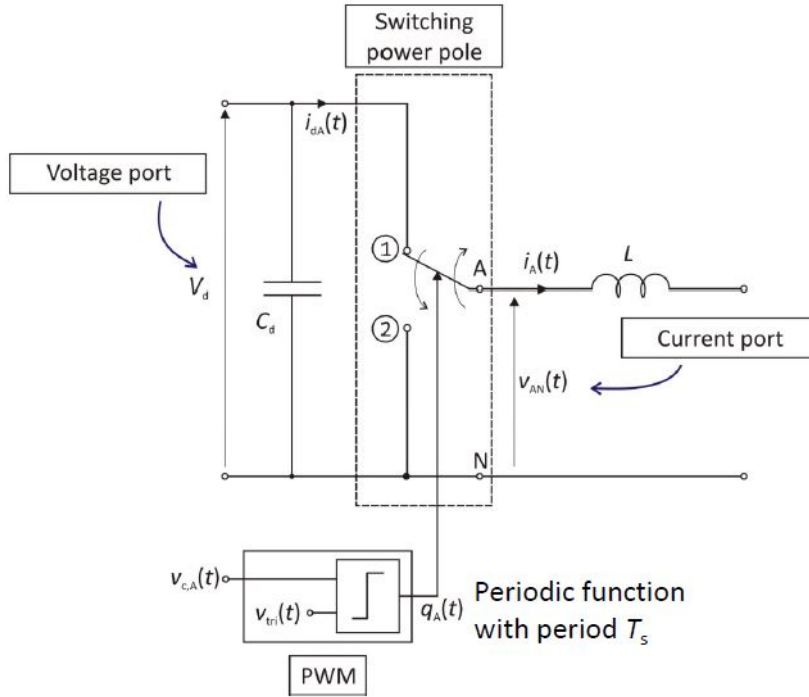


Figure 3.2: Switching power pole [5].

and to obtain the desired output the common solution is to use a low pass filter to extract only the average value:

$$\overline{V_{an}} = V_d \cdot d_a(t) \quad (3.2)$$

where $d_a(t)$ is the duty cycle of the unitary switching function and it is defined as the ratio between the ON and the total switching period.

The easiest way to generate a unitary switching function is by using the naturally sampled Pulse-Width (PWM), as illustrated in Figure 3.3. The implementation requires the generation of a triangular carrier and the use of an analog comparator. Its goal is to convert the analog control signal into a pulse-width modulated drive command for the switches. The modulating signal then is compared to the carrier to determine the logical value of the unitary switching function as follow:

- When $v_{c,a}(t) \geq v_{tri}(t)$, then the unitary switching function of the high side switch is high;
- When $v_{c,a}(t) < v_{tri}(t)$, then the unitary switching function of the high side switch is low.

Note that the control signal provides a variable duty cycle (sinusoidal modulated) on the unitary switching function and consequentially on the output of the switching

power pole. In particular, the average value of this square wave is sinusoidal and the positive/negative peaks correspond to the areas of the greater/lesser density of "1" command.

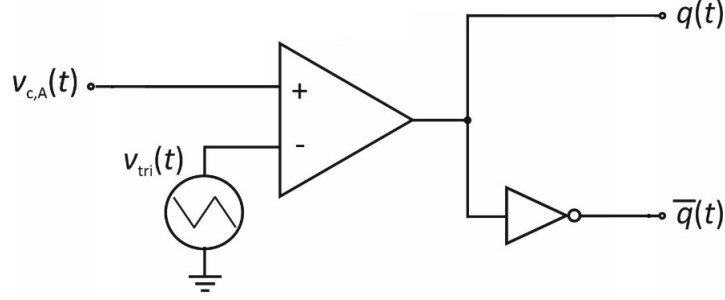


Figure 3.3: Classic pulse width modulator.

Based on these concepts, it is possible to provide some useful figures of merit of the inverters and how they have been set on this work. Defining \hat{V}_{tri} as the peak value of the triangular carrier and $V_{c,a}$ as the peak value of the control signal, it is possible to define the amplitude modulation factor m_a as:

$$m_a = \frac{V_{c,a}}{\hat{V}_{tri}} \quad (3.3)$$

In particular:

- When $0 < m_a < 1$ the modulator operates within the linear region and the output voltage amplitude vary linearly with m_a ;
- When $m_a > 1$ the modulator enters in the so-called overmodulation region. It follows that the amplitude of the output fundamental component does not vary anymore linearly with m_a .
- When m_a becomes so large that the control voltage waveform intersects with the carrier only at $\hat{V}_{tri}/2$, a square wave modulation occurs. The output voltage is independent of m_a .

In this work, both the inverters work in the linear region, and then a modulation factor higher than 1 will be not considered in the next sections. Furthermore, the frequency modulation factor is defined as the ratio between the carrier switching frequency and fundamental component of the output voltage:

$$m_f = \frac{f_{sw}}{f_1} \quad (3.4)$$

In particular, the switching frequency of both applications is expected to be between 10 kHz and 15 kHz. Finally, a topic point on inverter analysis is that two switches of the same leg cannot be closed at the same, otherwise a short circuit of the supply occurs and the device could be permanently damaged. For this reason, a dead time must be inserted between the complementary commands of the two switches, defining a period in which both switches of the same leg are off at the same time. In particular, the dead time set on this work is:

$$t_d = 1\mu s \quad (3.5)$$

3.1.1 Space vector pulse width modulation

The modulation method used for both the inverters of this thesis work is a Space Vector Pulse Width Modulation (SVPWM), which is a variant of the classic PWM and it has become a popular PWM technique for three-phase VSI. It is an improved technique for generating less distortion on output and provides more efficient use of the supply voltage in comparison to the classical sinusoidal modulation techniques. Also, the SVPWM is an inherently digital modulation method and it may be implemented easily with a modern DSP-based control system. The SVPWM is based on Park's transform concept applied on three variables having the following characteristics:

- Arbitrary;
- Independent;
- Reals;
- Dimensionally homogeneous;
- Their sum must be always zero.

In this case, they can be represented in a bidimensional vectorial space as:

$$\vec{u}(t) = C \left[u_a(t) + u_b(t)e^{j\gamma} + u_c(t)e^{2j\gamma} \right] \quad (3.6)$$

where $\gamma = 120^\circ$, C is a scalar constant and $\vec{u}(t)$ is the so-called space vector. This equation can be manipulated considering that:

- The exponential terms can be written in Euler's representation;
- The space vector can be written as sum of real ($u_\alpha(t)$) and imaginary ($u_\beta(t)$) component.

After some manipulation, the following matrix is found:

$$\begin{bmatrix} u_\alpha \\ u_\beta \end{bmatrix} = C \begin{bmatrix} 1 & -1/2 & -1/2 \\ 0 & \sqrt{3}/2 & -\sqrt{3}/2 \end{bmatrix} \begin{bmatrix} u_a \\ u_b \\ u_c \end{bmatrix} \quad (3.7)$$

This matrix allows converting a system with 3 variables in a vector with a real and an imaginary part. Considering the three variables as three cosine waveforms with 120° of shift each other, the following expression is found:

$$\vec{u}(t) = C \hat{u} \frac{3}{2} e^{j\omega t} \quad (3.8)$$

Here, the most common choice for C value is $C = 2/3$. In this case, space vector is said in the "amplitude invariant form":

$$\vec{u}(t) = \hat{u} e^{j\omega t} \quad (3.9)$$

Now, it is possible to apply this concept to a three-phase inverter. Since there are eight switch combinations, the line-to-line voltages can assume eight different combinations based on the input commands of each switch. In particular, the input commands are represented by three variables since the switches on the same leg cannot be closed at the same time. In this way, based on the status combination of these variables, eight different positions of the space vector are defined as shown in Figure 3.4. Looking at Figure 3.4, the following statements hold:

- For each of the eight combinations of the switches, a space vector \vec{V}_i can be computed;
- Each space vector is identified by a three-digit binary sequence, the so-called switching word;
- Six of these space vectors (the active ones) lie in the complex plane and are separated by 60° to adjacent vectors, dividing the space into six sectors;
- Two null vectors are located at the origin and can be used to define a dead time;

Obviously, all the figures of merit defined for the classical PWM are valid by using the SVPWM.

3.1.2 Tedder inverter

As seen before, the two inverters fall within the same scope but they are used in different systems. Nevertheless, the two inverter projects followed the same

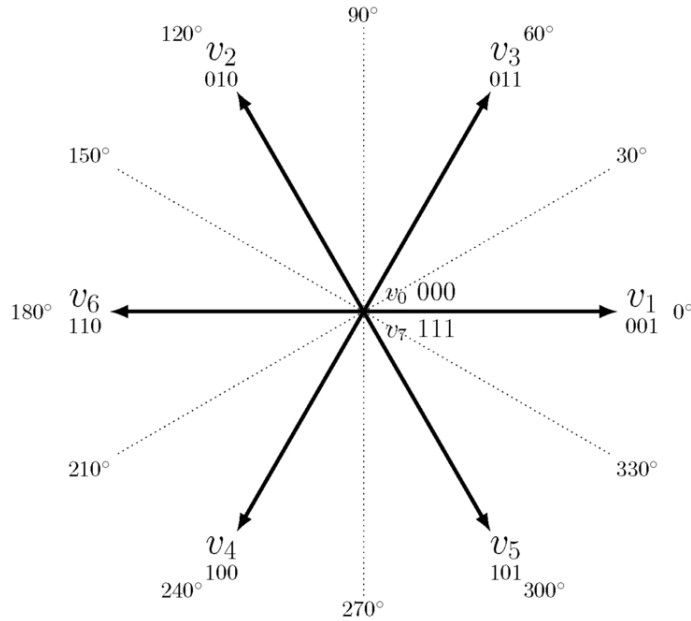


Figure 3.4: The eight basic space vectors with their magnitude and direction [6].

process, taking into account the differences in terms of rated power, application and functionality. For this reason, a very detailed description of the tedder inverter will be made, while for the ditcher one just the project differences will be highlighted.

Since the tedder inverter has to drive four different motors, it has been divided into 4 single inverters all equal to each others. The structure has been designed to make a device as compact as possible: starting from the single configuration, the quadruple one is extracted by doubling and mirroring the structure, getting the structure shown in Figure 3.5. The inverter is designed to be supplied by 700 V, which will be considered ideal for this work. A good rule is to put a dc-link capacitor at the inverter input side for more effective stabilization of the dc-link voltage. As the required capacitance can be large, any optimization in terms of the number of capacitors required is important [7]. In this application, four high-voltage capacitors are used in parallel, allowing to increase the equivalent total capacitance and to reduce the total ESL and ESR. The main characteristics of the employed capacitor are reported in Table 3.1. A ceramic capacitor is never employed as a dc-link capacitor due to the need for high capacitance values. Choosing between electrolytic or film capacitors, instead, depends on the requirements. Electrolytic capacitors have a higher stored energy density, lower cost, and allow to maintain ripple current rating at higher temperatures. The film capacitors, instead, exhibit lower ESR and higher voltage ratings [9]. Looking at the 700 V supply, the choice of film capacitor looks to be the most reasonable. The frequency behavior of the

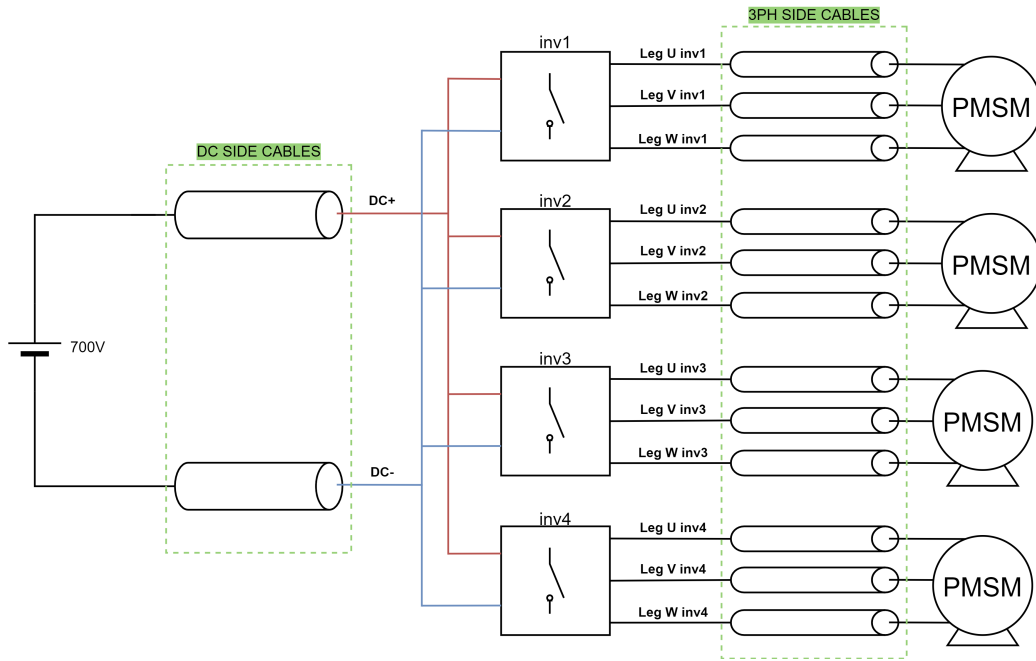


Figure 3.5: Concept scheme of the tedder system quadruple configuration.

Maximum voltage	900 V
Capacitance	50 μ F
ESR	5.6 m Ω
ESL	15 nH

Table 3.1: Dc-link capacitor main parameters [8].

selected capacitor is shown on the device datasheet and reported in Figure 3.6, where it can be seen that the resonant frequency is at around 100 kHz and define the upper frequency at which the capacitor is still working properly, while after that value the resistive and inductive behaviors become dominant. The selection of the dc-link capacitors is very important from the EMC point of view. It represent the component of the EMI filter which is closer to the inverter, allowing a reduction of the ripple on the supply and of the DM current entering on the LISN. Nevertheless, in high-power and high-speed devices, the presence of this capacitor is not enough to reach the desired attenuation to be compliant with the normative and the design of an EMI filter is still mandatory.

Moreover, a 100 nF capacitor is placed in parallel to each leg and as close as it possible to the legs, minimizing the area formed by the capacitor and the leg. In this case, a simple SMD capacitor with a voltage rating of 1 kV is used for each leg.

The switches employed are Silicon Carbide (SiC) Power MOSFETs belonging to

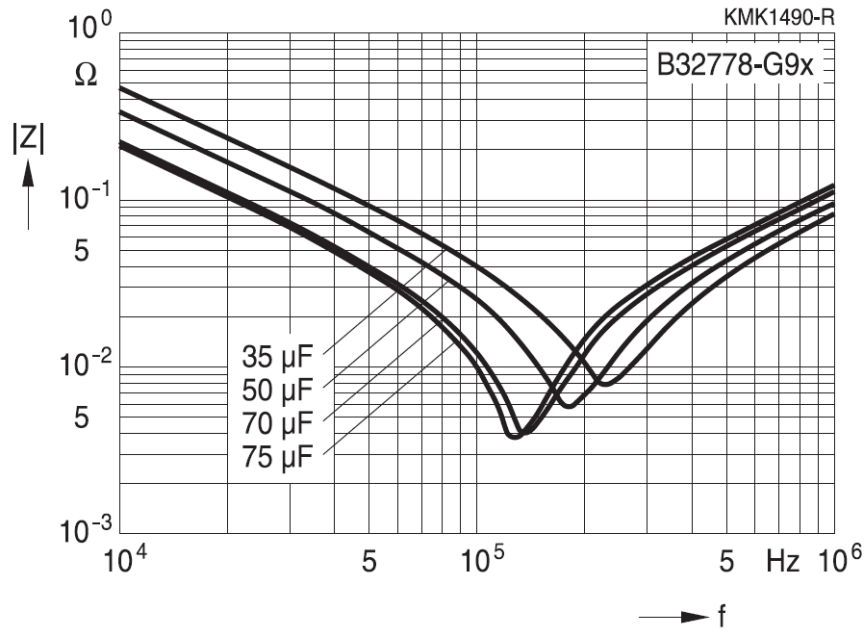


Figure 3.6: Dc-link capacitor impedance versus frequency [8].

the Cree family. Generally, Using SiC MOSFETs instead of classical Silicon ones, leads to the following advantages [10]:

- Reduced switching losses;
- Higher switching frequencies;
- Critical breakdown strength increased of around 10 times;
- Higher temperature operation and easier cooling mechanism.

The switch main electrical parameters are reported in Table 3.2. In particular, the current and voltage ratings respect the need of this application and the gate-source operating voltages are coherent with the gate driver specifications which will be shown below. Using a SiC MOSFET as a switch has the great advantage of obtaining a freewheeling diode "for free". In fact, as a consequence of the MOSFET structure, a body diode is formed by the PN junction between the source and drain. This body diode can conduct all the MOSFET rated current, but typically its switching speed is not optimized and its behaviour is quite slow.

Sometimes, a snubber is used acting as damping for the switch. It can be passive (formed of resistors, diodes, capacitors, or inductors) or active (formed of transistors or other active elements). In this work, it was initially thought to use an RC snubber in parallel to the switches to reduce both voltage overshoot

$V_{DS,max}$	1200 V
$V_{GS,op}$	-4 / + 15 V
I_D	115 A
$V_{TH,typ}$	2 V
$R_{DS,on,typ}$	16 m Ω

Table 3.2: SiC MOSFET main parameters [11].

and settling time [12]. In fact, the snubbers offer optimized protection against voltage transients during the normal turn-on and turn-off switching. Usage of such protection circuits allows containing the operating point within the boundaries of the rated Safe Operating Area (SOA) [13]. The snubbers were designed with $C_s = 1$ nF and $R_s = 10$ Ω , but subsequently it was decided to not integrate them on the device.

Since the devices used as switches are rated for high voltage applications, their commands have to be provided with the necessary power required to make the device turn ON/OFF properly. For this reason, the gate drivers have typically been used to convert a low-power command coming from a controller into a high-current input for the gate of high-power transistors. The applications described in this work foresee the use of a gate driver with these ON/OFF values:

$$\begin{cases} V_{on} = 15 \text{ V} \\ V_{off} = -3 \text{ V} \end{cases} \quad (3.10)$$

Finally, adding external gate drive resistors play a crucial part in limiting noise and ringing in the gate drive path. Parasitic inductances and capacitances and high dv/dt and di/dt can cause unwanted behavior without an appropriately sized gate resistor. To be precise, this resistance is in series with the gate driver output resistance, the MOSFET gate input resistance, and the inherent resistance of the PCB trace. A representation of gate driver and MOSFET, including some parasitics contributes, is shown in Figure 3.7.

3.1.3 Ditcher inverter

The design of the ditcher inverter follows the same procedure of the tedder one just described with some substantial differences. For example, only one electric motor needs to be driven, and using a single inverter is enough. This inverter, compared with the single of the tedder application, has to be rated to a higher power. The single tedder inverter is rated to drive an 8.6 kW motor, while the ditcher inverter for an 18 kW motor, in terms of nominal powers.

Most of the concepts explained for the tedder inverter are also valid in the ditcher one. Where possible, it was preferred to keep the same components and

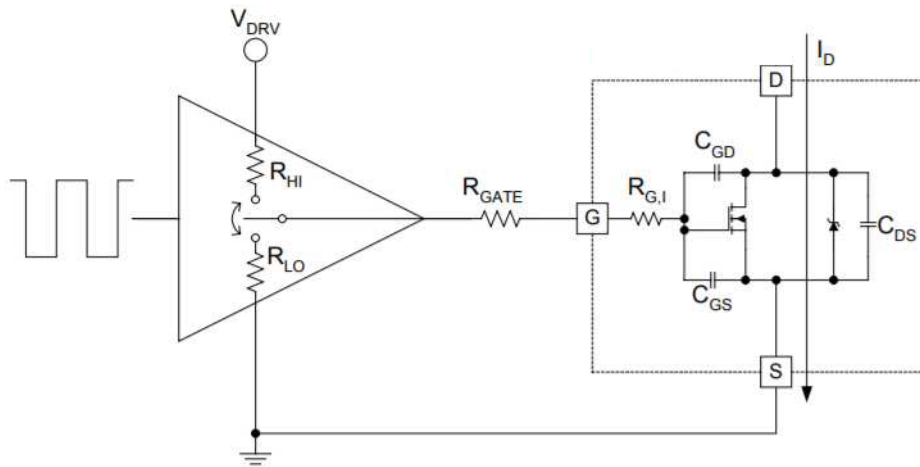


Figure 3.7: Gate driving of a MOSFET [14].

techniques used. For example, the dc-link capacitors and the SMD capacitors were maintained the same, while the switching devices are different. Three SiC modules of the Infineon family are used and they are not single MOSFETs as the ones of the tedder application, but they include the two switches internally. This kind of device is commonly known as a power module and its structure is shown in Figure 3.8. These modules are composed of two SiC MOSFETs and, since the inverter must



Figure 3.8: SiC power module [15].

be rated for a higher power, the switching modules have been chosen in order to work with a higher nominal current than tedder SiC MOSFET. The main electrical parameters are very similar to the previous application and reported in Table 3.3.

$V_{DS,max}$	1200 V
$V_{GS,op}$	-5 / + 15 V
I_D	200 A
$V_{TH,typ}$	4.5 V
$R_{DS,on,typ}$	5.63 m Ω

Table 3.3: SiC power module main parameters [15].

3.2 Electrical motors

Both motors employed on tedder and ditcher systems belong to the Permanent Magnet Synchronous Motor (PMSM) category but have substantial differences in terms of rated power, speed, current, and torque between each other. Below are presented the different solutions in terms of electric motor construction and application and an in-depth view of the PMSM employed.

In Figure 3.9 it is shown a classification of the most common rotating machines. In all cases, an electric motor is formed by a stator and a rotor and the categorization depends on the type of stator and rotor polarization, on the different performances, and on type of applications:

- The first categorization is done by looking at the motor physical construction. The reluctance motors present windings only on the stator and use the torque produced by the variation of the reluctance of the magnetic path. They are simple in construction but the developed torque is very small. The cylindrical motors, instead, have windings on both stator and rotor and exploit the torque by varying the mutual inductance between these windings. They are more complex in construction but allow to get a larger torque than the reluctance motor.
- One of the most common reluctance machines is the stepper motor. They have precise rotor positioning, excellent dynamic response, and very high reliability due to the brush's absence, but on the other side they don't operate at high speeds, are noisy, and develop a low torques.
- The cylindrical motors, instead, can be differentiated based on the kind of polarization of the stator and rotor. The Direct Current motors have stator windings excited with DC power. They require mechanical commutation devices, cause EM and acoustic noise, need periodical maintenance, and a maximum torque per ampere can be obtained. The Alternate Current motors, instead, have stator windings excited with AC power. Also, they are divided into synchronous motors if the rotor winding is excited in DC and induction motors if are excited in AC. The synchronous motors are better in terms of

efficiency, power density, and dynamic response, while the induction ones have simpler construction, lower cost, and higher speed operations.

- Finally, the third category of cylindrical motor is composed of brushless motors. They are hard to be classified since their construction is similar to that of an AC permanent magnet motor while the electrical characteristic is similar to those of a DC motor.

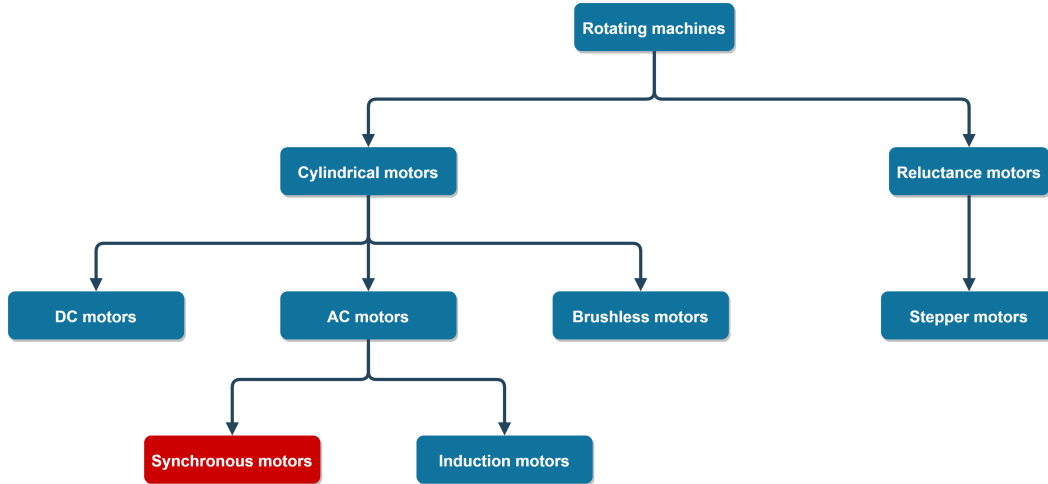


Figure 3.9: Rotating machines classification.

The PMSM is an AC motor which stator runs with a three-phase AC excitation, while its rotor is a permanent magnet. In this way, it doesn't need an extra DC power source for the rotor and, in addition, it is possible to get higher efficiency and power density with lower size and maintenance cost. On the other side, changing the stator current is the only way to control the motor and a complex control system is needed. In AC motors, when a three-phase voltage is applied to the stator windings a rotating magnetic field is generated. Most of the stator flux links to the rotor windings (the magnetizing flux) and contributes to the torque production, while a small portion of the stator flux links to the stator winding itself (the leakage flux). The equivalent circuit of each stator winding is shown in Figure 3.10. Here, the stator resistance R_s and leakage inductance L_{ls} depend on the physical construction of the winding. The voltage equation for the stator winding, instead, consists of:

$$v_s = R_s i_s + \frac{d\lambda_{ls}}{dt} + \frac{d\lambda_m}{dt} \quad (3.11)$$

The stator voltage depends on the rate of change over time of the stator leakage and magnetizing fluxes. In particular, this latter term can be also be expressed

in terms of the back-emf e_a , which represents the induced voltage on the stator winding:

$$e_s = \frac{d\lambda_m}{dt} = E_{max} \sin(2\pi f_s t) \quad (3.12)$$

On this definition, f_s is the stator excitation frequency and $E_{max} = 2\pi f_s N_s \phi$, where N_s is the total number of the series turns per phase.

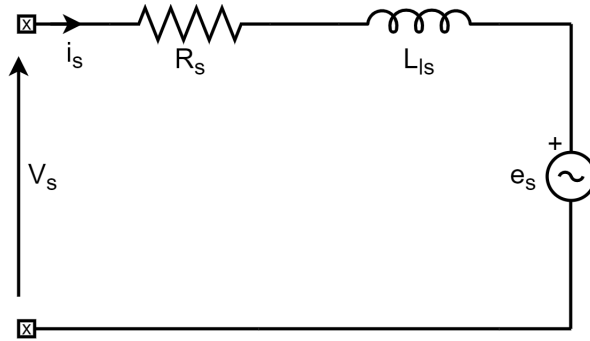


Figure 3.10: Per phase PMSM stator equivalent circuit.

Tedder application requires a quadruple inverter to drive four physically separated AC motors. Each of these PMSMs has been realized for the specific application and it is designed for a 700 V supply of the inverter and a 8.6 kW nominal power. The other main electrical parameters are reported in Table 3.4. The ditcher motor, instead, is used on the single application and it is designed for a 700 V supply for the inverter, with the difference that the nominal power now is 18 kW. The other parameters are reported in Table 3.4.

	Tedder motors	Ditcher motor
n_{nom}	250 rpm	3000 rpm
$f(2p)$	54.16 Hz (26)	200 Hz (8)
n_{max}	300 rpm	3500 rpm
K_e	1600 V _{rms} /K _{rpm}	140 V _{rms} /K _{rpm}
K_t	26 Nm/A _{rms}	2.3 Nm/A _{rms}
T_{nom}	330 Nm	60 Nm
I_{nom}	13 A _{rms}	27 A _{rms}
T_{max}	1000 Nm	170 Nm
I_{max}	45 A _{rms}	81 A _{rms}
R_{ff}	2.1 Ω	0.2 Ω
L_{ff}	80 mH	-
L_d	-	3.8 mH
L_d	-	3.6 mH

Table 3.4: Tedder and ditcher PMSM main parameters.

Chapter 4

Basic system model

The EMI filters must be designed by deriving the specifications about the required attenuation for both the differential and the common mode emission spectra. This can be done by modeling the entire systems for predicting the emission levels and the required attenuation necessary to stay within the regulation limits. Being the tedder and ditcher systems very similar, except for some differences, the model has been developed in this thesis first for the tedder system and later replicated for the ditcher one. One of the reasons is that the tedder inverter is the more complicated one and then modeling it allows to replicate the model easily on the ditcher inverter. In addition to this, during the realization of the model, the physical implementation of the tedder inverter was more forward than the ditcher one, allowing to have immediately more reliable information on its geometry. As a consequence, all the choices about the modeling and the impact of the parameters on EMI measurement are related to the tedder model, while for the ditcher one they are just replicated with the opportune differences.

A very reliable model needs very precise components behavior, resulting in a large amount of data to be processed. For this reason, in the beginning, it was planned to use LTSpice to realize the model, until realizing that it did not allow to refine the model more than a certain point. The rather limited computational capacity of this software did not allow to introduce a refinement necessary in this type of analysis. For this reason, this path has soon left and there has been no further extension on this type of modeling. It was therefore decided to use the Simscape tool available in the Simulink environment. Simscape allows the creation of accurate models of physical systems by defining and assembling all its components. In particular, the Simscape Electrical tool provides component libraries for modeling electronic, mechatronic, and power supply systems. The environment is very adaptable to the specific application, allowing the selection of simple models to get even faster simulations or non-linear models to capture detailed transient behavior and predict losses.

Since the quality of the results depends on the accuracy of the model realized, one of the main goals has been focused on the implementation of a model close to the real measurement setup, but considering a trade-off with the computational weight of the simulator. The model was refined until it was seen that in terms of emissions there were no longer major differences and therefore there was no longer the need to introduce new complications. All the steps that led to the creation of an increasingly reliable and complex model have been reported below, focusing on the effect that the main system parameters have in terms of EMI.

4.1 SVPWM model

First of all, a simple SVPWM algorithm has been implemented to properly drive the inverter models. The practical implementation of this modulation technique starts, as for the classic PWM, from the comparison between three sinusoidal waveforms shifted by 120° each other and the carrier triangular waveform. The main difference between the PWM and SVPWM implementation resides in the algorithm employed for the generation of the unitary switching function.

Simscape provides a *Space Vector Generator* block which generates the space vector modulation signals v_{ao} , v_{bo} and v_{co} starting from stator reference voltages $\alpha - \beta$. These have been mathematically extrapolated from the matrix on Equation 3.7 starting from the three shifted sinusoidal waveforms u_a , u_b and u_c . In this first analysis, the three sinusoidal waveforms have been set with an amplitude modulation factor of 0.9 and with the nominal rotating frequency of 54.16 Hz. The resulting three modulation voltages are shown in Figure 4.1. These three voltages are then compared with the carrier triangular waveform, set with $f_{sw} = 10$ kHz and amplitude between $[-1,1]$ V. A dead time of $1 \mu s$ has been introduced to avoid the supply short circuit. Considering only the first leg (for the other two legs the same discussion is valid), the unitary switching function was generated with the following rule:

$$\begin{cases} \text{if } v_{ao}(t) - f_{sw} \cdot t_d > v_{tri}(t) \implies UH_{inv1}(t) = 1 \\ \text{if } v_{ao}(t) + f_{sw} \cdot t_d < v_{tri}(t) \implies UL_{inv1}(t) = 1 \end{cases} \quad (4.1)$$

where UH_{inv1} and UL_{inv1} are, respectively, the commands to turn ON the upper and bottom switches of the first leg (the so-called "U" leg). Their behavior, shown in Figure 4.2, confirms that the dead time and the transistors commutation act correctly. The same procedure is valid for the other two legs (the so-called "V" and "W" legs) with 120° phase shift between each adjacent phase. The complete schematic of the complete SVWPM algorithm realized in this work is shown in Figure B.2 in Appendices B and D, where are also reported the schematics of the complete tedder and ditcher models.

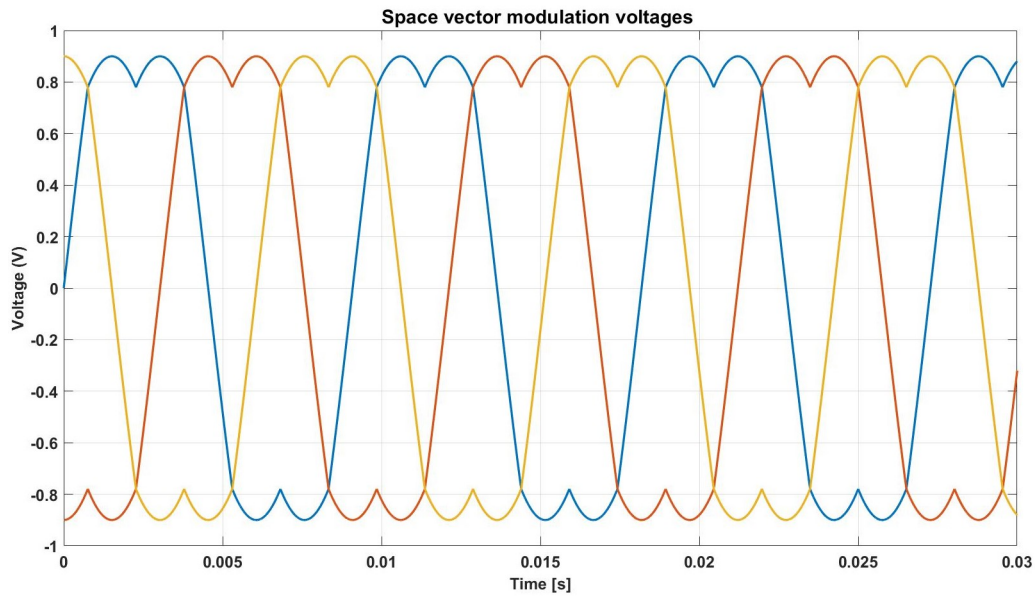


Figure 4.1: SVPWM modulating voltages.

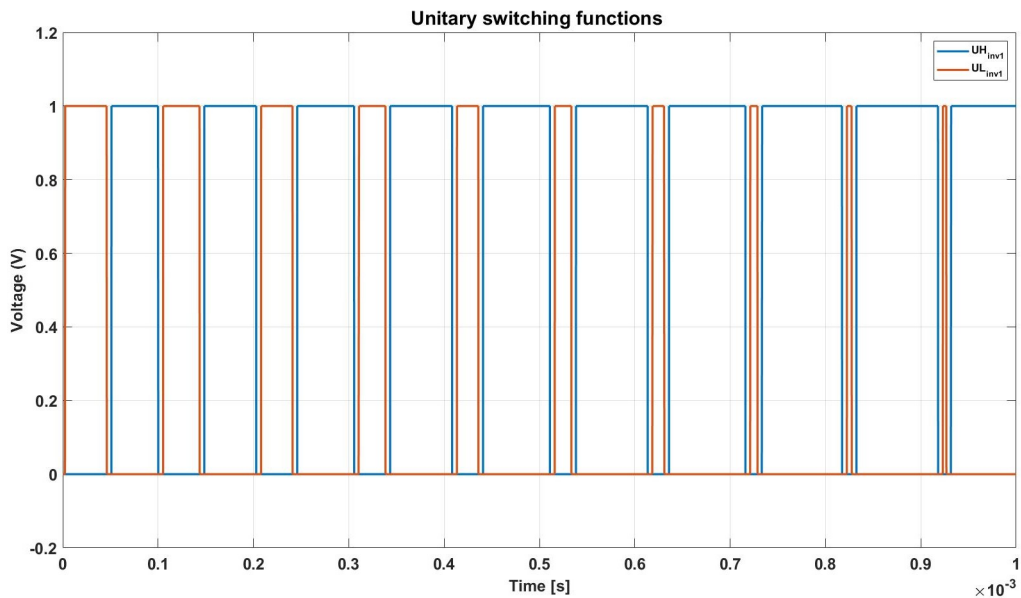


Figure 4.2: SVPWM unitary switching function of the first leg.

4.2 Motor and control data

Since in this work the analysis is focused on conducted emissions, the models have been implemented in an open-loop configuration. However, some equations

have been implemented to get the main control data of the system and to fix the operating point. If a more deep systems analysis is needed, then control feedback should be added to the model.

The steady-state equations have been implemented on a MATLAB script as shown in Appendix A and C. In particular, the simulation data are just related to the maximum and minimum frequency band of the normative, the switching frequency of the carrier, the dead time, and the resolution bandwidth of the spectrum analyzer. The motor data are the ones already shown in Table 3.4, with the difference that the torque constant T_e is extracted by the generated magnetic flux Φ_{Mp} and depends on the pole pairs PP and the phase current I_a :

$$\Phi_{Mp} \simeq \frac{2}{3} \frac{T_e}{PP \cdot I_a} \quad (4.2)$$

The computed value is then adjusted in order to provide voltage and torque constant as much as possible similar to the ones indicated on datasheets.

Each stator has been modeled as previously described and its three-phases representation is shown in Figure 4.3, where the three conductors are connected to the output of each inverter leg. To make a more deep representation, on a PMSM it

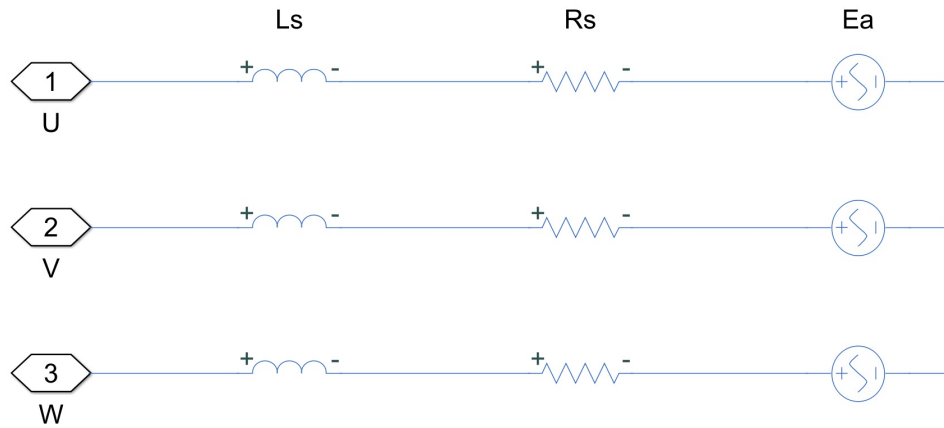


Figure 4.3: Three-phase stator equivalent circuit.

can be defined the D-axis (direct-axis) as the component of the stator magnetic field that is in phase with the rotor magnetic field, while the Q-axis (Quadrature-axis) as the component with 90° out of phase between these fields. Since the tedder motor datasheet reportes the phase-to-phase resistance and inductance, the L_q and L_d are supposed to be equal between them. The stator model needs the line-to-line resistance and inductances, given by the half of the phase-to-phase ones [16]. The R_S value as been increased by adding the 10 % of its nominal value, taking into account the so-called "hot resistance" equivalent. The back-emf voltages, instead,

are 120° out-of-phase each others, with frequency equal to the fundamental one and amplitude equal to $\Phi_{Mp} \cdot \text{Speed} \cdot \text{PP} \cdot \pi/30$.

Regarding the control data, the motor current and speed have been left variable when desired and, later on, they will be tuned looking at their effect on the conducted emission measurement. The others parameters, instead, are bounded by being dependent on them. The fundamental frequency (the frequency of the sinusoidal modulators) depends on the pole pairs, which is a fixed technology parameter, and on the speed, which is variable, as follow:

$$f_m = \text{PP} \cdot \frac{\text{Speed}}{60} \quad (4.3)$$

The amplitude modulation factor (the amplitude of the sinusoidal modulators), instead, depends on the kind of modulation used and on the D-axis and Q-axis voltage components:

$$m_a = \sqrt{V_q^2 + V_d^2} \cdot \frac{\text{mod}}{V_{dc}} \quad (4.4)$$

where $\text{mod} = 2$ is used for sinusoidal modulation and $\text{mod} = \sqrt{3}$ for SVPWM, and:

$$\begin{aligned} V_q &= R_s I_q + \Phi_{Mp} \cdot \text{Speed} \cdot \text{PP} \cdot \frac{\pi}{30} + L_d I_d \cdot \text{Speed} \cdot \text{PP} \cdot \frac{\pi}{30} \\ V_d &= R_s I_d - L_q I_q \cdot \text{Speed} \cdot \text{PP} \cdot \frac{\pi}{30} \end{aligned} \quad (4.5)$$

4.3 Ideal inverter model

After defining the parameters necessary to fix the operating point, a first simple model of the inverter has been realized looking at the time domain waveforms and verifying the correct system behavior. This starting model has been realized by including the 200 μF dc-link capacitor, the 100 nF capacitors at the input of each leg, and the *Ideal Switches* available on Simscape, as shown in Figure 4.4. The DC+ and DC- labels are connected to an ideal 700V battery and the leg outputs to the stator model as already shown in Figure 4.3. At the moment, the dc-link capacitor has been included defining only its nominal value and its ESR, as shown in Table 3.1. Being the 100 nF ceramic capacitors, instead, their ESR has been neglected, while the ideal switches have been configured as shown in Figure 4.5. This model doesn't include any turn-on and turn-off dynamic, then its influence on measured emission is still unreliable, but it allows for the evaluation of the time domain systems behavior. For example, the behavior of the UV line-to-line voltage, of the input current, and of the phase current are represented in Figure 4.6. The waveforms shown are obtained after the end of the transient phase. The LTL

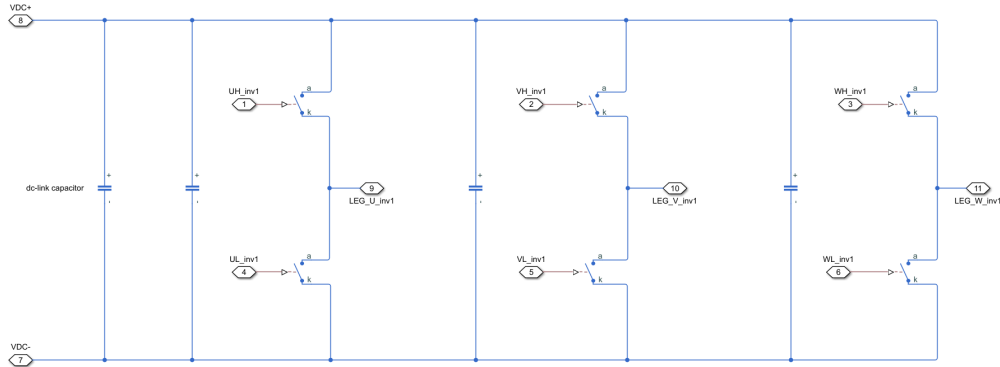


Figure 4.4: Implementation of ideal inverter model.

Main	Integral Diode	
On-state resistance:	16e-3	Ohm
Off-state conductance:	1e-5	1/Ohm
Threshold voltage, Vth:	0.5	V

Main	Integral Diode	
Integral protection diode:	Protection diode with no dynamics	
Forward voltage:	4.6	V
On resistance:	0.001	Ohm
Off conductance:	1e-5	1/Ohm

Figure 4.5: Configurations of the ideal switch block.

voltage behaves as expected, having a fundamental frequency of around $f_m = 43$ Hz, which is the expected one using Speed = 200 rpm on Equation 4.3. The waveform has a variable duty cycle so that its mean value is sinusoidal. Also, the phase current has, as expected, a period defined by the modulating frequency, while the input current is pulsed with a frequency equal to $6 \cdot f_m$. In particular, the pulsing behavior is due to the action of each switch and its envelope follows the shape of the modulating signals.

At this point, the LISN circuit has been inserted between the supply and the inverter mains, connecting its ground to the system reference as indicated on the normative. In particular, two LISNs have been included for both the positive

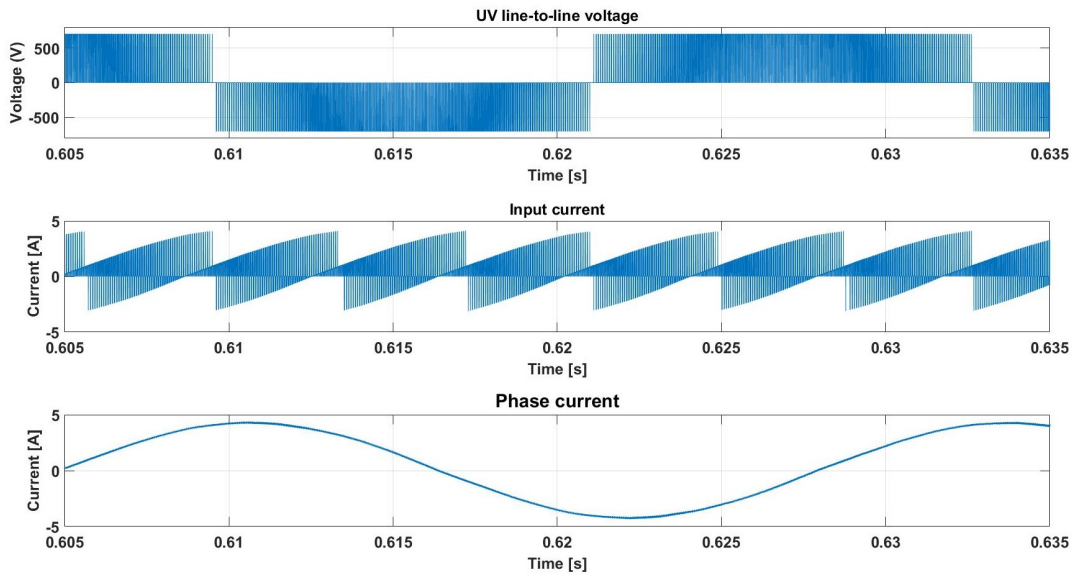


Figure 4.6: Time-domain behavior of the basic model.

and the negative conductors and the circuit topology following the normative specifications, as shown in Figure 4.7. On the LISN schematic, a $50\ \Omega$ resistance has been included on the measurement port to represent the input impedance of the spectrum analyzer used to perform the measurement. However, to properly see the emission spectrum, it is necessary to make an overview of the solver and SA configuration settings.

4.4 Solver configurations

One of the issues of the first simulations concerned understanding the use of the solvers made available on Simulink. In general, it is possible to make a distinction between global and local solvers. The global solver is the one available on the *Model Settings* section and it refers to all the libraries present in the Simscape environment. It allows choosing between fixed-step and variable-step simulations. The variable step is the most efficient one since the simulator changes the step size based on the system's behavior. In this case, maximum and minimum step sizes can be fixed. For the fixed-step simulation, instead, the step size is always the same and specified on a predisposed field. Also, several kinds of the solver are available and their functionality depends on the kind of model to be realized. However, the configurations of the global solver remained unchanged since it has not been used.

On the other side, using the local solver is mandatory for the components

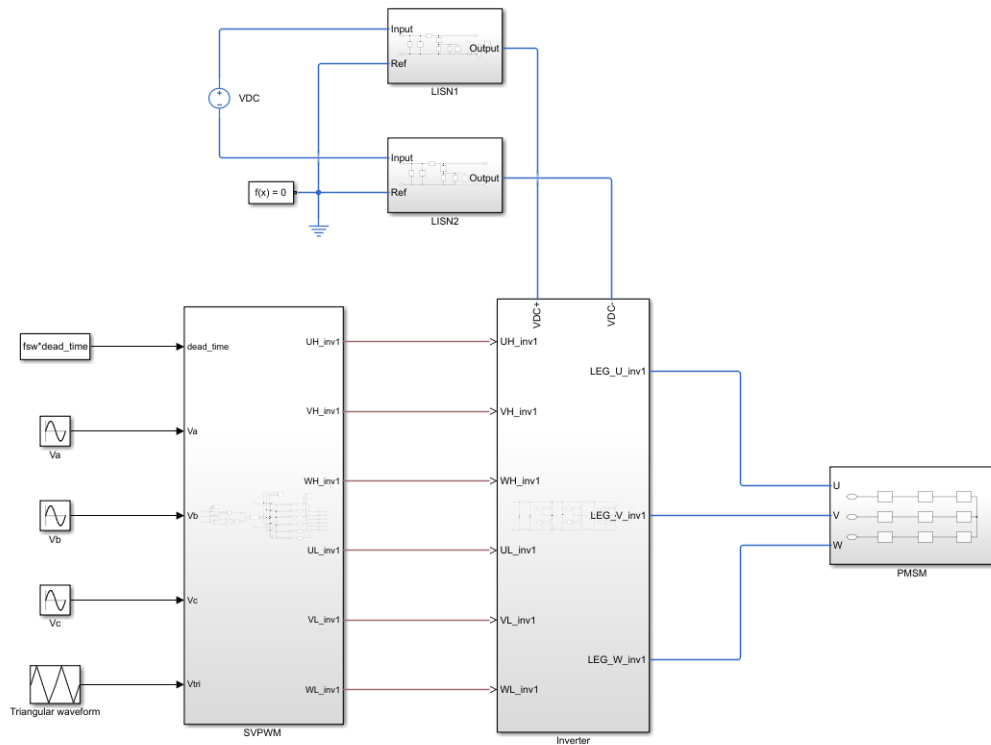


Figure 4.7: Block diagram of the basic model including SVPWM, inverter, LISNs, and PMSM

available on Simscape electrical tool. The *Solver Configuration* block allows specifying the solver parameters that the Simscape model needs before starting the simulation. Each Simscape block diagram requires a solver configuration block attached and, for this reason, a common solution is to connect it directly to the system reference block. The main parameters included in this block have been set as follows.

The *Start simulation from steady state* box must be checked if the steady-state research is desired. It acts by keeping the inputs constant for a sufficiently large time for starting the simulation from the computed steady-state. However, sometimes this configuration greatly lengthens the simulation times when the steady-state point is not found immediately. For this reason, a different solution will be presented later for the transient elimination.

The *Consistency tolerance* value affects the initial conditions computation determining how accurately the algebraic constraints are to be satisfied at the beginning of the simulation. Decreasing this parameter value allows obtaining more reliable initial conditions while increasing it is useful if the starting computation

failed to converge if reducing the simulation time is necessary. Since the initial condition is very simple, as it will be seen later on, this parameter has practically no influence on results and it can be chosen large enough to reduce simulation time. For this reason, in this work, it has been set to $1e - 3$, while the default value is $1e - 9$.

The *Solver type* box proposes the solver typology used for updating the states between Backward Euler, trapezoidal rule, or partitioning. To use it, the *Use local solver* box must be selected. In this case, the Trapezoidal Rule has been selected since it is the one that allows eliminating the transient as quickly as possible. The *Sample time* specifies the discretization time for the local solver and it is a very important parameter in this analysis. It defines also the maximum frequency viewable on the SA. Considering $f_{max} = 30$ MHz, which is the maximum frequency of the normative, the spectrum can be plotted until 30 MHz only if the sampling frequency is set at least equal to the Nyquist frequency:

$$f_{Nyquist} = 2 \cdot f_{max} \quad (4.6)$$

To make an adequate frequency analysis, the lower limit for the sampling time has been set at $t_{sampling} = 0.5/f_{max}$. However, to get more reliable results, it is good to work at sampling times that are quite higher than those of Nyquist, as $t_{sampling} = 0.1/f_{max}$.

4.5 Spectrum analyzer configurations

Other important configuration settings are the ones for the spectrum estimation on the LISN measurement port. It is important to use a spectrum analyzer as imposed by the normative, following the characteristics previously shown in Table 2.3. Fortunately, the *Spectrum Analyzer* block available on Simulink can be set properly to have the required characteristics and it has been used at the LISN measurement port to evaluate the conducted emission spectrum. In particular, the SA can be configured as follows.

The *Input domain* has been set to the time domain and then the frequency spectrum is calculated with the algorithm specified by the *Method* field. This field allows to choose between Welch and filter bank algorithm for the spectrum estimation. The filter bank approach, generally, produces a precise peaks detection but it leads to increased computation time and slower tracking. Since the spectrum is detected with averaging type, the Welch method is the more suitable for this work.

The *Type of spectrum to display* allows choosing between power, power density, and Root Mean Squared (RMS) spectrum to be visualized. The RMS type has been set as it corresponds to the display identified as "averaging" in the normative

description, being one of the options available on the average detection of a SA [17]. The *RBW*, instead, has been set to 9 kHz as indicated by the normative specifications.

The *Overlap* field allows setting the amount of overlap, in percentage, between the previous and current data windows. In other words, for the definition of Welch's method, the spectrum is estimated by splitting the time domain signal into overlapping segments. When the data are split up into overlapping segments, each data segment has a measurement window applied on it [18]. Increasing the overlap between the adjacent segments allows getting a more reliable average spectrum estimation, at the price of a longer simulation time. On Figure 4.8 the effect of the overlap is evaluated by using overlap equal to 0%, 50% and 75% on the LISN measurement. It can be seen that the difference between 50% and 75% is not too large, but both provide a higher emission measurement than the 0% overlap case. To get a trade-off between the accuracy and the simulation time, this parameter has been set to 50%.

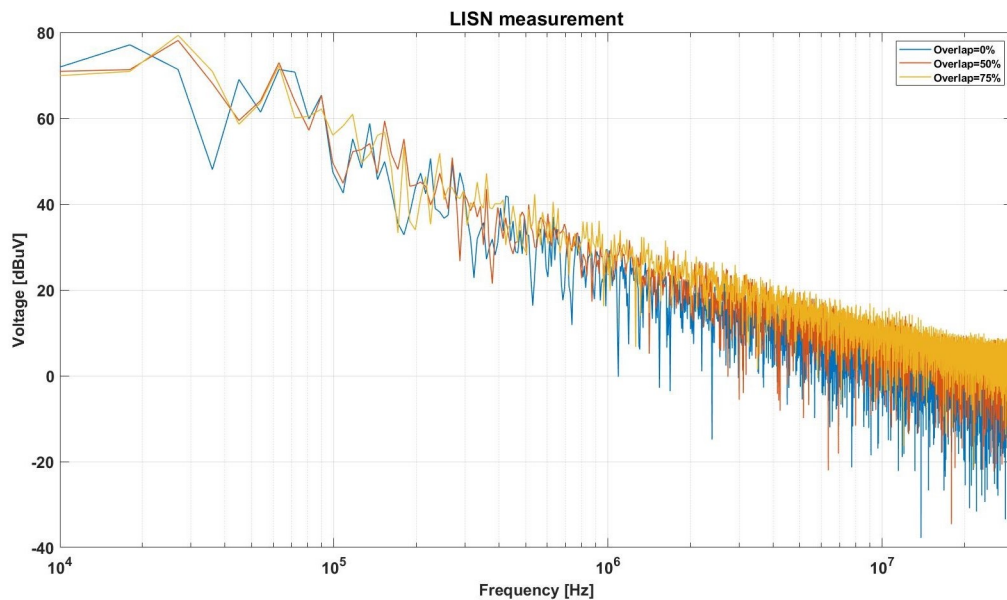


Figure 4.8: Effect of the overlap on LISN measurement.

The *Window* field allows choosing the windowing method for the spectrum estimation. The default window is the rectangular one, which "weighs" in the same way all the points within the data segment. A common alternative is the Hamming window, which acts by "tapering" the segment smoothly to zero at the start and end of the window. In particular, the window has a cosine shape that starts at 0.08, rises to 1 in the middle of the segment, and then goes down to 0.08 at the end.

This windowing technique is very useful on narrowband signals and can be suitable in this measurement since an overlap has been applied [19]. Fixing the overlap to 50%, a comparison between the rectangular and Hamming window measurement is shown in Figure 4.9, looking that the differences are not so evident. However, the Hamming windowing has been chosen because during the SA simulation the spectrum displaying is clearly more stable rather than the rectangular windowing.

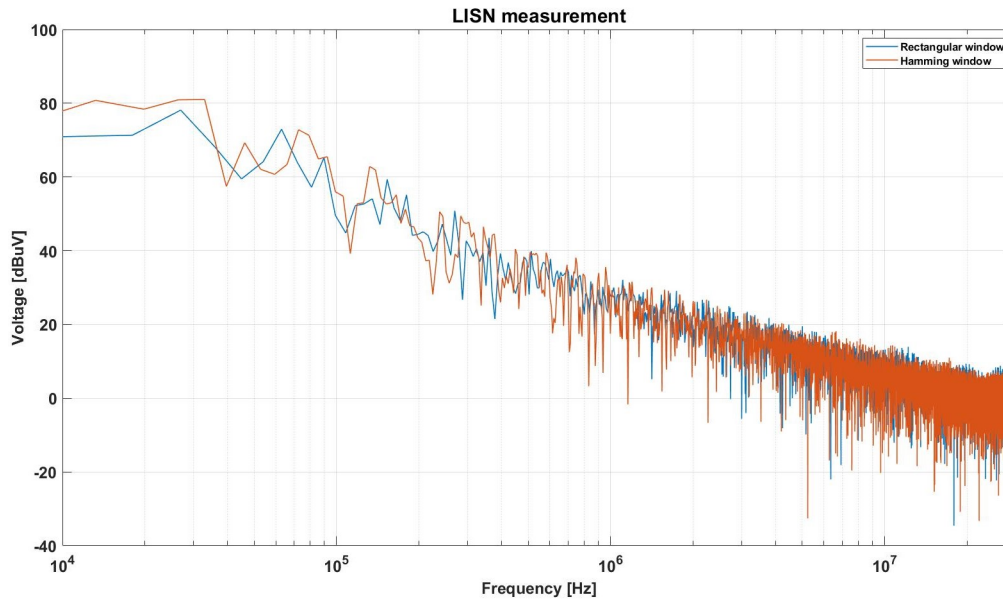


Figure 4.9: Effect of the windowing on LISN measurement.

Finally, the parameter *Averages* defines the number of spectra estimation "N" to be performed for each data segment so that its spectrum estimation is given by the average of the "N" measurement. Increasing it, the results will be more precise but the simulation time is increased by around "N" times. This is confirmed by the results shown in Figure 4.10 where, after fixing the Hamming windowing and 50% overlap, the number of averages has been swept looking at their effect on spectrum estimation. Again, being the difference between $N = 5$ and $N = 10$ quite small, but relevant compared to $N = 1$, the number of averages has been fixed to $N = 5$, getting a trade-off between results reliability and simulation time.

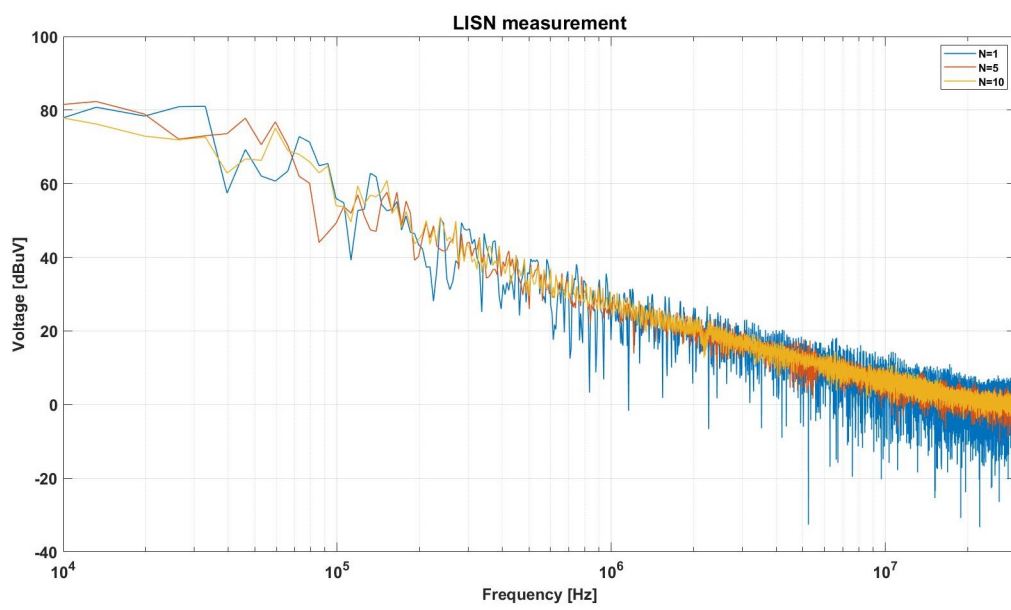


Figure 4.10: Effect of the number of averages on LISN measurement.

Chapter 5

Advanced system model

After the analysis of the basic system model and the setting of the main parameters, the model has been further refined by including all the non-idealities. The main goal is to predict the emission sources, including them within the model as efficiently as possible, and then evaluate their influence on the LISN measurement. This phase is important not only to predict the required attenuation for the EMI filter design but also to find some system design indications from the EMC point of view by looking at the emission "weight" of each parameter. Also, following the philosophy adopted until now, it was tried to complicate the model always keeping in mind the efficiency and timing of the simulator.

5.1 Elimination of initial transient

The results shown in the previous chapter are related to the regime response of the system, which is reached only waiting until the end of the transient time. As long as a very simple system is analyzed this is not a big issue since the simulation time is quite short, but complicating the model it represents a limitation that is best to remove. In addition to this, the transient phase influences the LISN measurement until its contribution becomes negligible compared to the one given by the regime phase. For this reason, eliminating the transient phase is important for both the simulation time and the result's reliability.

Simscape provides more than one solution for this issue. One of them, as seen before, is provided by the *Solver configuration* block that makes available the *Start simulation from steady state* option for the steady-state computation. Nevertheless, this functionality allows to compute the steady-state and then start the simulation: this would allow to plot results related only to the regime phase, as desired, but would not reduce too much the simulation time. For this reason, a different approach has been used. The Simscape *Capacitor* block allows setting its

initial voltage to make a sort of precharge. Since the $200\ \mu\text{F}$ and 100nF capacitors are placed between DC+ and DC- conductors, they have been simply precharged at 700 V as shown in Figure 5.1. This setting is as simple as effective since almost all

Parameters		Variables		
Override	Variable	Priority	Beginning Value	Unit
<input type="checkbox"/>	Current	None	0	A
<input type="checkbox"/>	Voltage	None	0	V
<input checked="" type="checkbox"/>	Capacitor voltage	High	700	V

Figure 5.1: Precharge of the capacitor blocks.

the transient has been eliminated during simulations, as shown in Figure 5.2. The benefits of the transient elimination are evident mostly by looking at the voltage on the LISN measurement port. Since this is the waveform used by the SA to make the spectrum estimation, its reliability is fundamental.

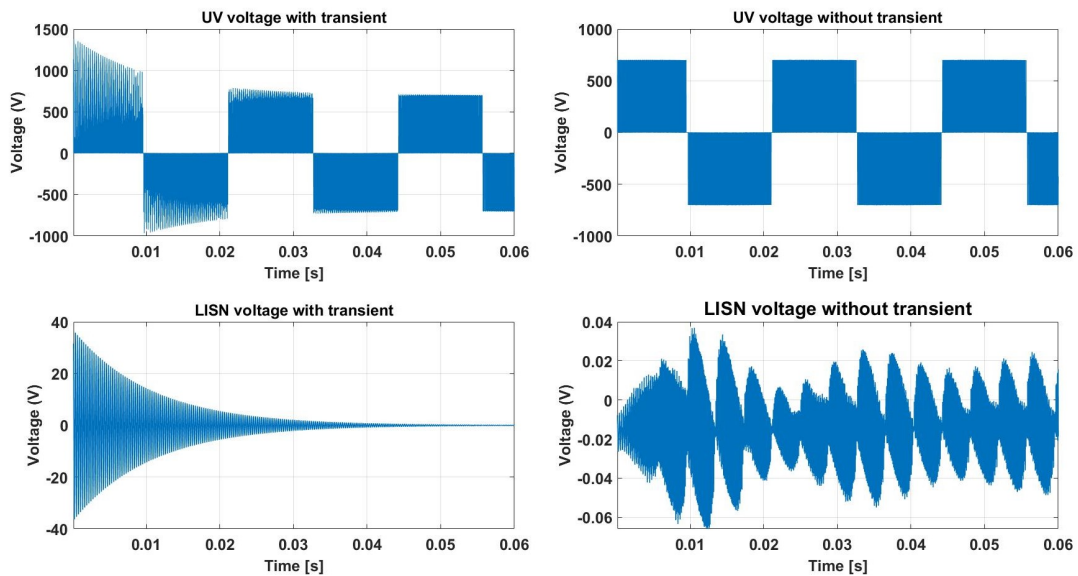


Figure 5.2: Transient effect on line-to-line and LISN voltages.

5.2 Choice of the MOSFET model

The next step regards the substitution of the ideal switches shown in Figure 4.4 with MOSFET models which include all the main parameters of the employed SiC devices. In particular, Simscape provides two solutions for the MOSFETs: the *MOSFET (Ideal, switching)* and the *N-channel MOSFET*. To perform a comparison between their behavior, the schematic shown in Figure 5.3 has been realized. The

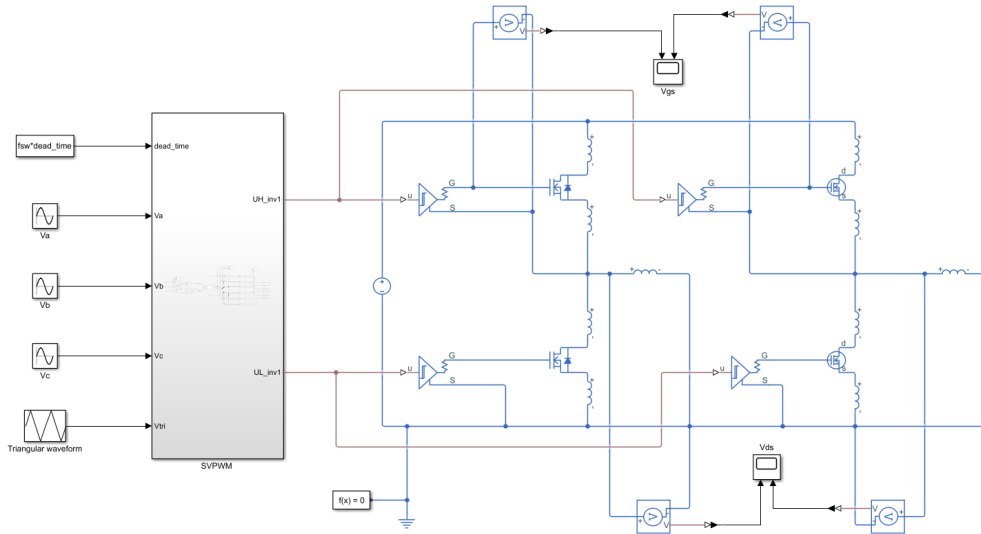


Figure 5.3: Schematic of the MOSFET models comparison.

schematic includes a 700 V supply and an SVPWM control only for the "U" leg, implemented two times with the two available models. In both cases, each leg includes also the gate drivers and the device drain and source inductances. The gate drivers have been configured with the levels previously indicated in Equation 7.16 to properly turn on and turn off the MOSFETs. Following the datasheet information, the output pull-up resistance has been set at 2.5Ω while the output pull-down resistance at 0.3Ω [20]. The inductances, instead, represent the inherent connection of the MOSFET source and drain with the external PCB. They have been extracted by the LTSpice model made available by the SiC device and their values are reported in Table 5.1.

L_s	2.4 nH
L_d	4.4 nH

Table 5.1: Equivalent inductances of drain and source of SiC MOSFET [11].

The *Ideal MOSFET* is a very simple component and has the same functionality of an ideal switch, allowing the definition of the on-state resistance, the threshold voltage, and the characteristics of the freewheeling diode. The *N-channel MOSFET*, instead, is very accurate since allows the definition of several parameters such as the resistive and capacitive non-idealities of the device. In particular, its parameters have been set as shown in Figure 5.4 by looking at both device datasheet and the LTSpice model. To evaluate the time-domain behavior of the two models, four voltages sensors have been used: two for the input commands which drive the "top" MOSFETs and two for the voltages at the output nodes. Figure 5.5 show a zoomed view around the transitions of these measurements. As expected, the *Ideal* model behaves as the already used ideal switches. From the EMC point of view, it doesn't define the dv/dt transition necessary to predict the emission level. On the other side, the *N-channel* MOSFET present a very satisfying behavior in terms of non-idealities on both command and switching voltages. The overshoot and the oscillation before the stabilization are very common in switching applications due to the resonance of the non-idealities. These parasitic effects are then included in initializing the model parameters as shown in Figure 5.4. This model allows also to define a delay between the command and the switching voltage and a quite precise dv/dt of the waveform, allowing a reliable EMC analysis. Using such a precise model of the MOSFET means increasing considerably the simulator computation weight and the overall simulation time. However, having found a way to eliminate the transient from the simulation allows choosing the *N-channel MOSFET* for more accurate analysis without many simulation troubles.

Once the time-domain behavior of the two MOSFET models has been evaluated, they have been also inserted on the inverter model as shown in Figure 5.6 to see their difference on LISN measurement. The schematic, now, includes all the three legs of the inverter, each one controlled by a separated SVPWM control signal. The gate drivers and the drain/source inductances have been also imported and also the gate resistances have been included and set to $5\ \Omega$, taking care of the PCB trace inherent resistance, the output of the gate drivers, the more or less $1\ \Omega$ SMD (Surface Mounted Device) resistance present and the $2.6\ \Omega$ input resistance on the gate of the transistor [11]. At this point, the system has been simulated with both the MOSFET models to see their difference in spectrum estimation, getting the results are shown in Figure 5.7. The two spectra exhibit the same behavior at low frequencies ($f < 1\ \text{MHz}$), where the MOSFET non-idealities are still not acting. For $f > 1\ \text{MHz}$, as expected, the spectrum obtained using the *N-channel MOSFETs* has an higher spectral content due to their parasitic effects. At the moment, it is not a big constrain since in both cases the normative limit is not reached yet, but other parasitic and coupling contributions have to be added to the current model.

Main	Ohmic Resistance	Capacitance	Body Diode	Temperature Dependence
Number of terminals:	Three			
Parameterization:	Specify from a datasheet			
Drain-source on resistance, $R_{DS(on)}$:	16e-3	Ohm		
Drain current, I_{ds} , for $R_{DS(on)}$:	75	A		
Gate-source voltage, V_{gs} , for $R_{DS(on)}$:	15	V		
Gate-source threshold voltage, V_{th} :	2.5	V		
Channel modulation, L :	0	1/V		
Measurement temperature:	25	degC		

Main	Ohmic Resistance	Capacitance	Body Diode	Temperature Dependence
Source ohmic resistance:	8.4e-3	Ohm		
Drain ohmic resistance:	87.4e-6	Ohm		

Main	Ohmic Resistance	Capacitance	Body Diode	Temperature Dependence
Parameterization:	Specify fixed input, reverse transfer, and output capacitance			
Input capacitance, C_{iss} :	6085	pF		
Reverse transfer capacitance, C_{rss} :	13	pF		
Output capacitance, C_{oss} :	230	pF		
Gate-drain charge-voltage linearity:	Gate-drain capacitance is constant			

Main	Ohmic Resistance	Capacitance	Body Diode	Temperature Dependence
Model body diode:	Exponential			
Reverse saturation current:	400e-9	A		
Built-in voltage:	0.7	V		
Ideality factor:	1			
Zero-bias junction capacitance:	5179	pF		
Transit time:	10e-9	s		

Figure 5.4: Parameters of N-channel MOSFET [11].

5.3 Contribution of PCB traces

The accurate inverter model can be further refined by considering the parasitic effects introduced by the physical traces on the inverter PCB. Generally, every wire or PCB trace can be modeled as a series of resistance and inductance. The equivalent resistance has been simply measured experimentally with a multimeter

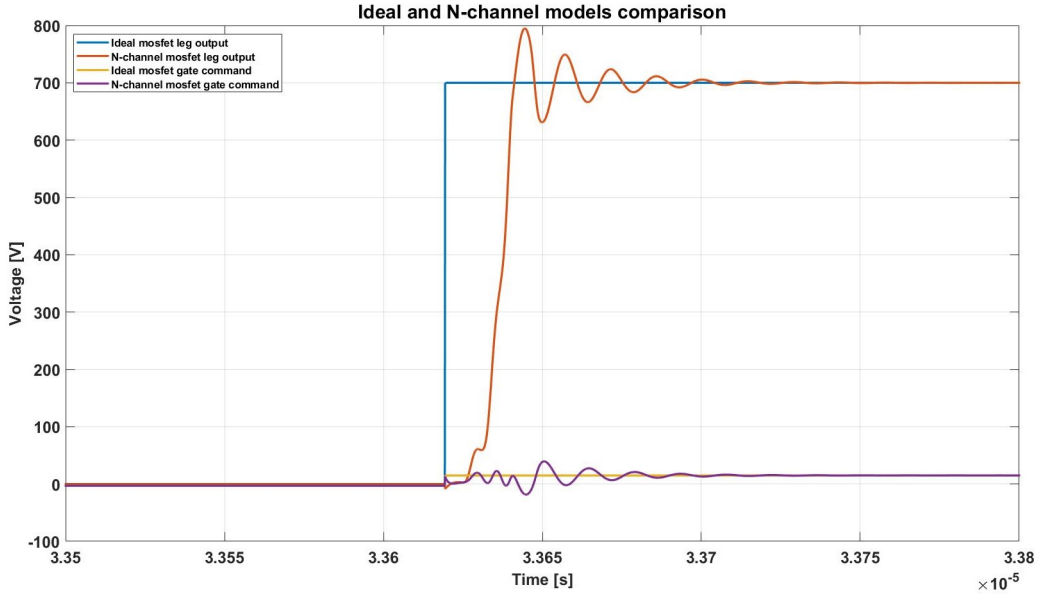


Figure 5.5: Behavior of *Ideal* and *N-channel* MOSFET output voltages.

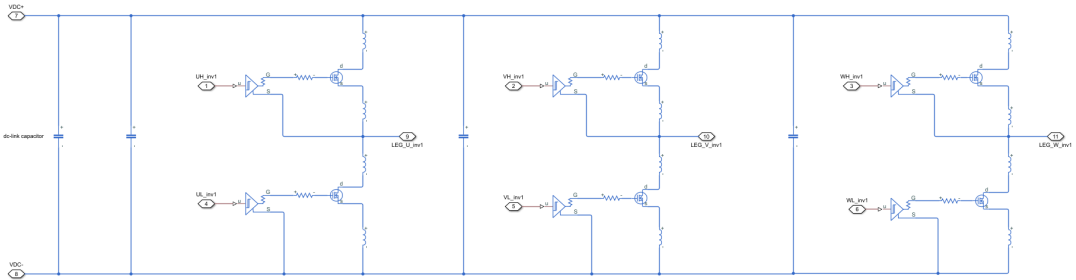


Figure 5.6: Insertion of MOSFET and gate driver models in inverter model.

on the board and it has been fixed to $300 \mu\Omega$. The equivalent inductance, instead, is a topic point on the ECM analysis because it is a source of resonance with the parasitic capacitances and its value has been estimated at 10 nH. The equivalent resistance and inductance are then included in the inverter model as shown in Figure 5.8. Then, a LISN measurement has been performed and compared to the one without these parasitics contributions, getting the result is shown in Figure 5.9. The two spectra have the same behavior until around 500 kHz and then a peak is formed at around 1 MHz. This peak is due to the resonance between the inductance of PCB traces and the MOSFET drain/source inductances, and the output capacitance C_{oss} of the MOSFET itself. On the other side, after the peak,

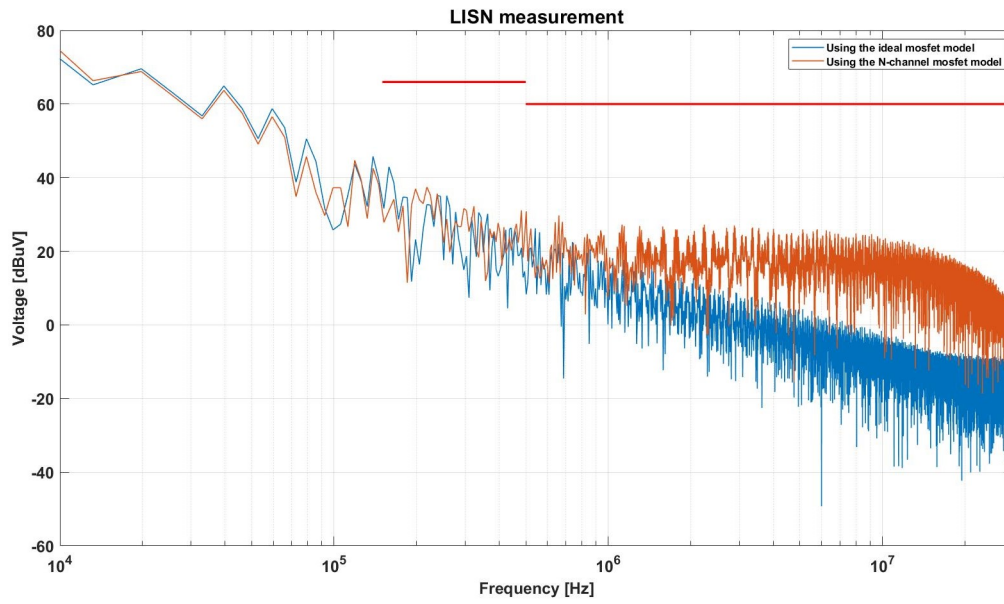


Figure 5.7: Comparison of *Ideal* and *N-channel* MOSFETs on the LISN measurement.

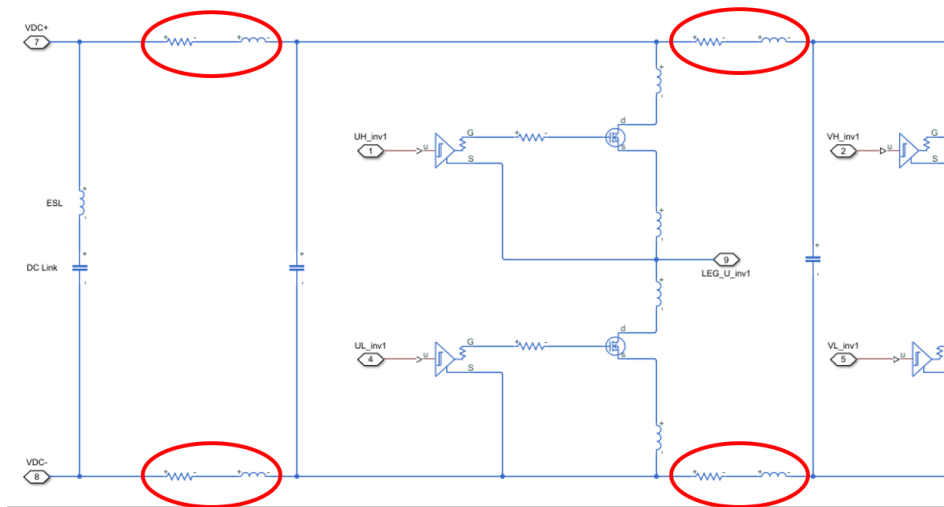


Figure 5.8: Insertion of PCB traces parasitics on the inverter model.

the spectrum goes down with a -20 dB/decade slope since, for the same reason, a low-pass LC filter is formed.

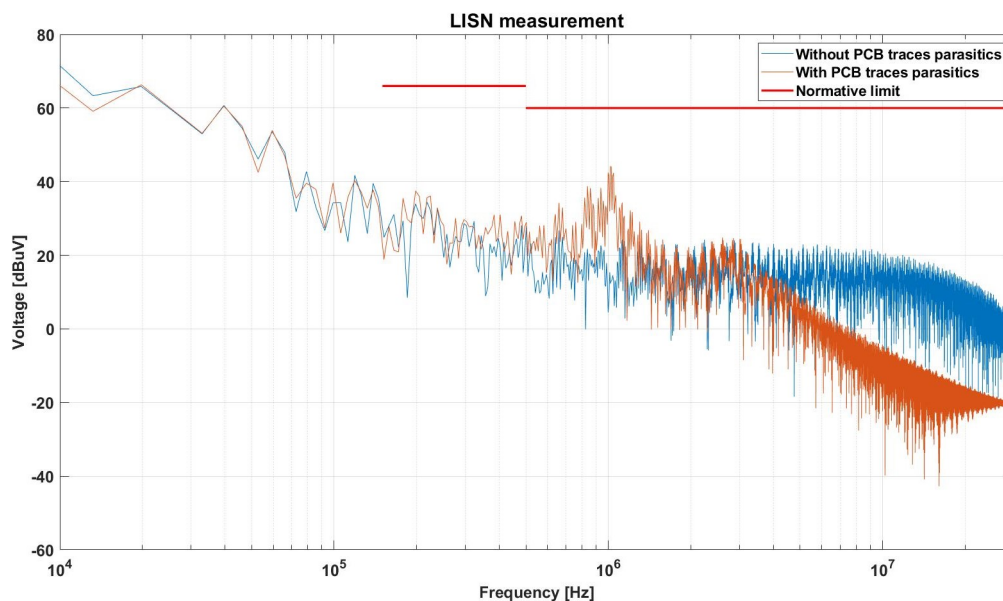


Figure 5.9: Effect of the PCB traces parasitics on the LISN measurement.

5.4 Cables model

The power supply, the inverter, and the motor are physically connected to each other with power cables. To include them in the current model, a cable modeling procedure is exploited, looking at their effects on both time and frequency domains. In this section, the connection cables between the battery and the inverter will be labeled as "DC side cables" and they have to carry all the current required by the inverters. The cables connecting the inverter with the motors, instead, carry the three-phase current needed by the PMSM and, for this reason, they will be labeled as "three-phase side cables".

The cables employed on these applications are chosen firstly by looking at their power ratings. The cables cross-section is chosen to look at the maximum current that should flow on DC and three-phase sides. The selected cables for these applications belong to the E-mobility family of the "Coroplast", which are optimized for automotive connection of HV batteries and electric motors [21]. A simplified view of their cross-section is represented in Figure 5.10 and allows to understand how a typical power cable is internally realized. In particular, the employed cables are screened, silicone-insulated and single-core, with a voltage rating of $600VAC/1000VDC$ [21]. On the DC side, the same cables are employed for both tedder and ditchers applications, while different cross-sections are needed for the three-phase side. The DC length of the "DC side cables", on the final

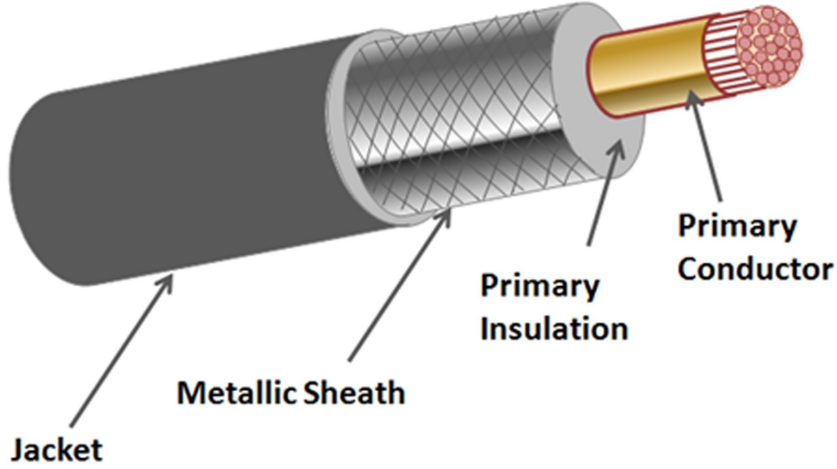


Figure 5.10: Typical cross section of power cables [22].

application, could be even 10 m; however, on the model, it has been set to 1 m in accordance with the instruction imposed by the measurement setup regarding the connection between the LISN and the DUT. Also, by looking at the cables datasheet, it has been calculated the measures of the output radius (at the end of the jacket), the inner one (of the conductor), and the shield thickness and radius, as reported in Table 5.2.

	DC side	Tedder 3ph side	Ditcher 3ph side
l_{max}	1 m	2 m	1.5 m
r_{out}	7.9 mm	2.9 mm	5.1 mm
r_{in}	5.3 mm	1.4 mm	2.9 mm
t_{sh}	0.105 mm	0.08 mm	0.08 mm
r_{sh}	7.2 mm	2.3 mm	4.4 mm

Table 5.2: Power cables main geometry parameters [21].

The distance between the DC cables and the reference plane is imposed by the normative at $h = 0.1$ m. For sake of simplicity, the same distance has been used for the separation between the three-phase cables and the reference. The distance D between the cables among them, for both DC and three-phase sides, must satisfy the large separation hypothesis, according to which D should be sufficiently larger than the wire diameter. Looking at the r_{out} values on Table 5.2, $D = 0.1$ m has been chosen. These geometrical parameters were necessary to realize the cables model and they have been illustrated in Figure 5.11, considering the DC side case.

The three-phase side representation is the same but with three conductors instead of two.

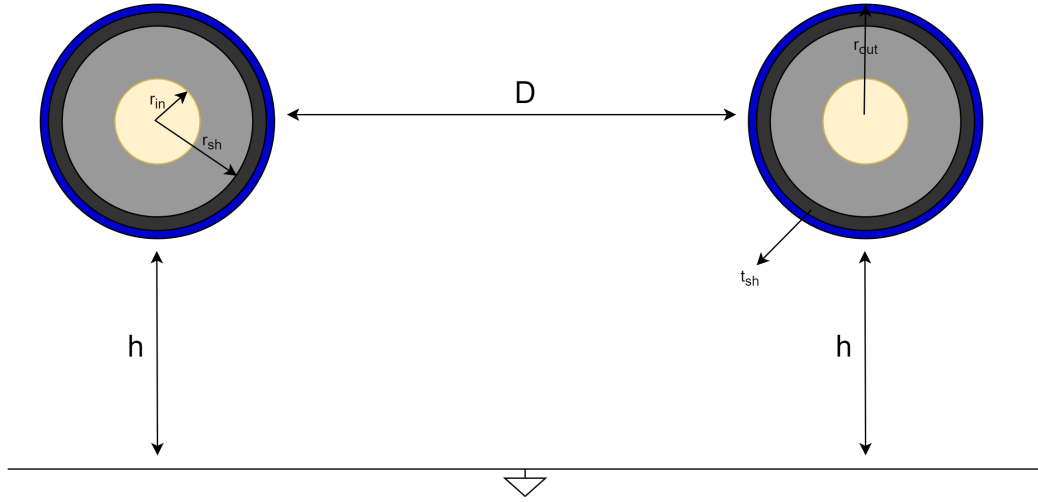


Figure 5.11: Power cables disposition.

It is also necessary to look at the main electrical parameters of the materials used for the cables realization. The primary conductor is a single-core classic copper, the insulator is silicon rubber and outside of the jacket, there is air. For this reason, the electrical parameters needed to properly model the cable parasitics are reported in Table 5.3.

Parameter	Symbol	Value
Copper resistivity	ρ_c	$1.68 \cdot 10^{-8} \Omega\text{m}$
Copper conductivity	σ_c	$5.98 \cdot 10^7 \text{ S/m}$
Silicone rubber conductivity	k	$3.16 \cdot 10^{-12} \text{ W/mK}$
Silicone rubber relative dielectric constant	ϵ_r	4
Vacuum dielectric constant	ϵ_0	$8.85 \cdot 10^{-12} \text{ F/m}$
Vacuum magnetic permeability	u_0	$1.26 \cdot 10^{-6} \text{ H/m}$
Relative permeability	u_r	$\simeq 1$

Table 5.3: Power cables main electrical parameters.

The cables model has been realized with the MTL approach as shown in Chapter 2. In order to find out the value of the Δ_z line section, the wavelength has been calculated starting from the phase speed:

$$v_{ph} = \frac{c}{\sqrt{\epsilon_r}} = 1.5 \cdot 10^8 \text{ m/s} \quad (5.1)$$

Considering $f = 30$ MHz, since it is the maximum frequency of the normative limit, the wavelength is:

$$\lambda = \frac{v_{ph}}{f} = 5 \text{ m} \quad (5.2)$$

To make a reliable model, any line section length should be several times smaller than the wavelength. For this reason, it has been fixed to:

$$\Delta_z = \frac{\lambda}{10} = 0.5 \text{ m} \quad (5.3)$$

Comparing the Δ_z with the total length of the cables, the number of section needed for each cable are reported in Table 5.4. The cables model have been implemented by connecting together all the line sections among them.

	DC side	Tedder 3ph side	Ditcher 3ph side
Cable length	1 m	2 m	1.5 m
n° of sections	2	4	3

Table 5.4: Number of line sections for each power cable.

Having found all the necessary geometry and electrical data of the cables, now it's possible to implement their model. In this section, only the DC side case will be explained, while the AC one is the same with different geometry data and one more conductor. Anyway, the data and computation of both side cables are shown in Appendix A. The goal is to define the MTL elements as described in Chapter 2. The only difference, in this case, is given by the presence of the shields around the conductors. In this way, the couplings of the conductor act only on its shield, which is externally coupled with the other shield and the reference. A graphical representation of the DC side cables including the parasitic elements is shown in Figure 5.12. The PUL wire resistance is indicated on cables datasheet [21]. The other conductor parasitics can be computed by using the widely known modeling formulas of coaxial cables. The PUL conductor inductance is given by:

$$L_{wire} = \frac{\mu_0 \mu_r}{2\pi} \ln \left(\frac{r_{out}}{r_{in}} \right) \quad (5.4)$$

The capacitive effect between the conductor and the shield is influenced by the presence of the silicone rubber insulator and its PUL value is given by:

$$C_{cs} = \frac{2\pi \epsilon_0 \epsilon_r}{\ln \left(\frac{r_{sh}}{r_{in}} \right)} \quad (5.5)$$

The PUL conductor to shield conductance, instead, is:

$$G_{cs} = \frac{2\pi k}{\ln \left(\frac{r_{sh}}{r_{in}} \right)} \quad (5.6)$$

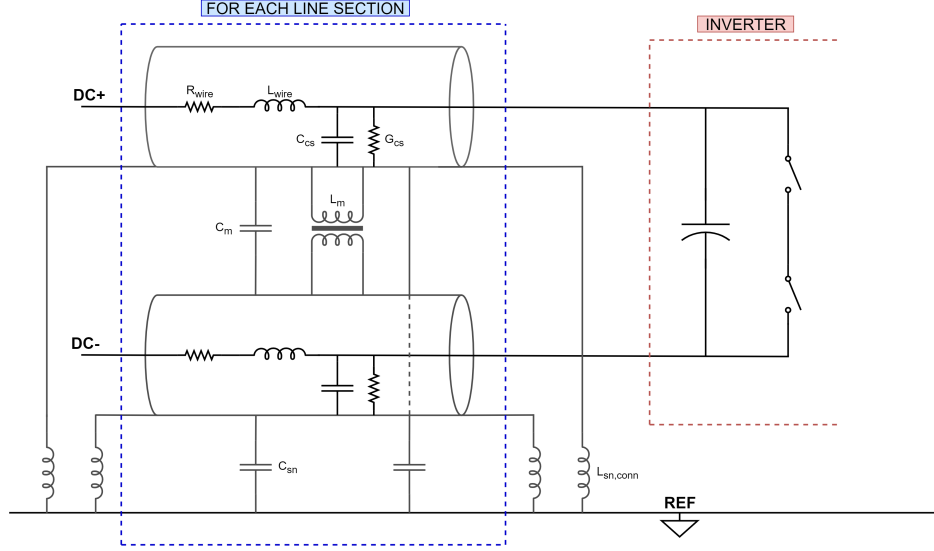


Figure 5.12: DC side cables and their parasitic elements.

Also the shield, as the conductor, can be modeled as a series of an inductance and a resistance. Since the cables are screened-copper, the PUL resistance is given by:

$$R_{sh} = \rho_c \frac{1}{\pi(r_{out}^2 - r_{sh}^2)} \quad (5.7)$$

The PUL inductance of the shield, instead, is given by [23]:

$$L_{sh} = \frac{\mu_0 \mu_r}{2\pi} \ln \left(\frac{2h}{r_{out}} \right) \quad (5.8)$$

The coupling effects of the shields are obtained under the hypothesis of wires above infinite ground plane [23]. The shields exhibit a capacitive and an inductive coupling among them. The PUL shield-to-shield inductive coupling is given by:

$$L_m = \frac{\mu_0 \mu_r}{4\pi} \ln \left(1 + 4 \frac{h^2}{D^2} \right) \quad (5.9)$$

The PUL mutual inductance and capacitance are related by [23]:

$$C_m = \frac{L_m}{v^2 (L_{sh}^2 - L_m^2)} \quad (5.10)$$

where:

$$v = \frac{1}{\sqrt{\mu\epsilon}} \quad (5.11)$$

Each shield has also a capacitive coupling with the reference plane, given by [24]:

$$C_{sn} = \frac{2\pi\epsilon_0\epsilon_r}{\operatorname{acosh}\left(\frac{h}{r_{out}}\right)} \quad (5.12)$$

Since all these elements are PUL, the structure on figure 5.12 must be reproduced 2 times on the DC side. The shield to reference connections, instead, are defined externally for all the sections. In particular, it is supposed to directly connect them to the ground plane, which is 10 cm below the cables. The shields are connected both on left and right sides to obtain a more effective shielding. At first approximation, these connections have been modeled with 1 nH/mm, obtaining:

$$L_{sn,conn} = 1 \cdot 10^{-6} \cdot h = 100 \text{ nH} \quad (5.13)$$

The PUL results obtained from this analysis have been reported on Table 5.5. On

	DC side	Tedder 3ph side	Ditcher 3ph side
R_{wire} [mΩ/m]	0.368	4.71	4.71
L_{wire} [nH/m]	81.7	145.6	112.9
C_{cs} [pF/m]	705	440.3	528
G_{cs} [pS/m]	63	39.3	47.2
R_{sh} [mΩ/m]	0.2	0.8	0.3
L_{sh} [nH/m]	662	884	758.9
L_m [nH/m]	160	161	160.9
C_m [pF/m]	17.3	9.5	13
C_{sn} [pF/m]	68.8	52.5	60.6

Table 5.5: Results of PUL cables model parameters.

the AC side, the same situation should be reproduced by using three conductors instead of two and looking at the geometry differences. The implementation formula, instead, remains the same. The PUL model, in that case, must be replicated 4 times, and the shield to reference connections has been modeled similarly to the DC side case.

The results have been reported on the model by reproducing the line sections shown in Figure 5.12. The coupling elements between the shields and the reference and between the shields themselves have been directly implemented with their respective blocks. The conductor couplings with the shields, instead, have been represented by using the *Transmission Line* block available on Simscape. The "lumped parameter L-section" has been selected as the configuration of the block to properly model the computed elements. The block has four ports, two for the input/output of the inner conductor and two for the external shielding connection. The parameters of the TL on the DC side have been defined as shown in Figure 5.13.

Parameters	
Model Type:	Lumped parameter L-section
Parameterization:	By inductance and capacitance
Inductance per unit length:	L_wire_DC*1e6 uH/m
Capacitance per unit length:	C_cs_DC*1e12 pF/m
Resistance per unit length:	R_wire_DC Ohm/m
Insulation conductance per unit length:	G_cs_DC S/m
Line length:	piece_l m
Number of segments:	1

Figure 5.13: Parameters of *Transmission Line* block.

5.4.1 Cables effect

Once model of the cables have been integrated on the system model, it is important to see their influence on emission measurement. The cable effects on power switching converters have been widely covered in literature, mostly focused on the time domain behavior of phase voltages. For example, one of the main issues regards the motor overvoltage in SiC-based cable-fed drives. The fast switching speed results in high dv/dt , causing excessive oscillations and large overvoltage across the motor terminals. This effect is known as the reflected wave phenomenon and it is related to wave propagation in transmission lines [25]. This phenomenon has been verified on the model as shown in Figure 5.14. The label "inverter side" is related to a measurement performed by putting a scope on the inverter output, then before the AC cables. The "motor side", instead, is the measurement at the motor terminals. As expected, the motor fed cables cause large overshoot and oscillations on phase voltage.

Moreover, the DM current is also influenced by the DC side cables and, in particular, by the amount of current entering into the LISN measurement port as shown in Figure 5.15. This current is given by the partition of the inverter input current between the impedance seen on the dc-link capacitor and the one seen towards the LISN. The first impedance is given by the ESL of the dc-link capacitor, which so far has been neglected while now assuming an important role. The second impedance, instead, is the one seen on the DC cables. The resulting current is delivered to the LISN and measured as DM emission. For this reason, the model is not complete just inserting the cables model and it is mandatory to also insert the ESL of the dc-link capacitor. The nominal value of the ESL for

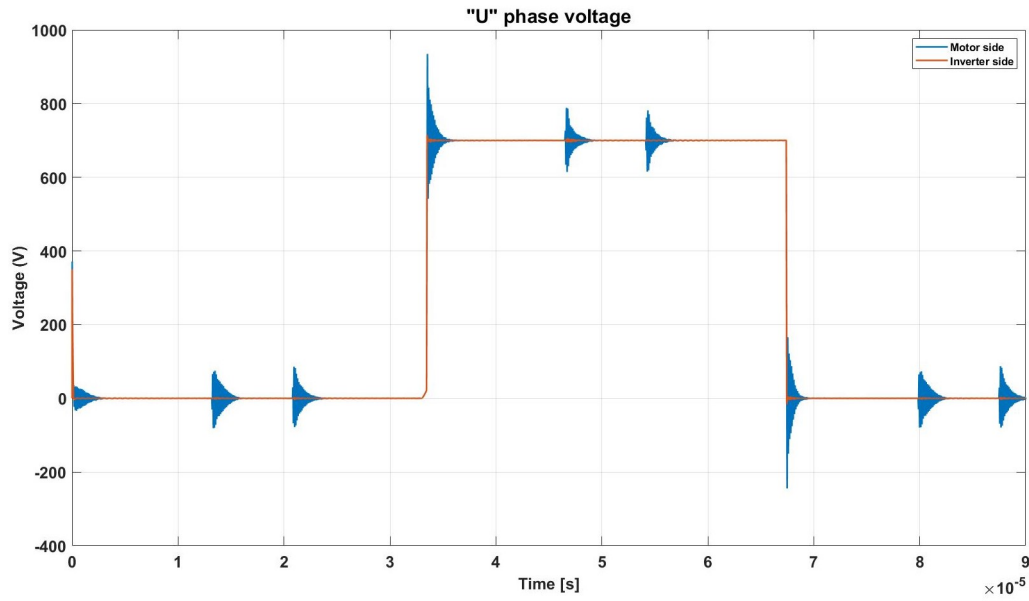


Figure 5.14: Effect of cables model on voltage measured at motor terminals.

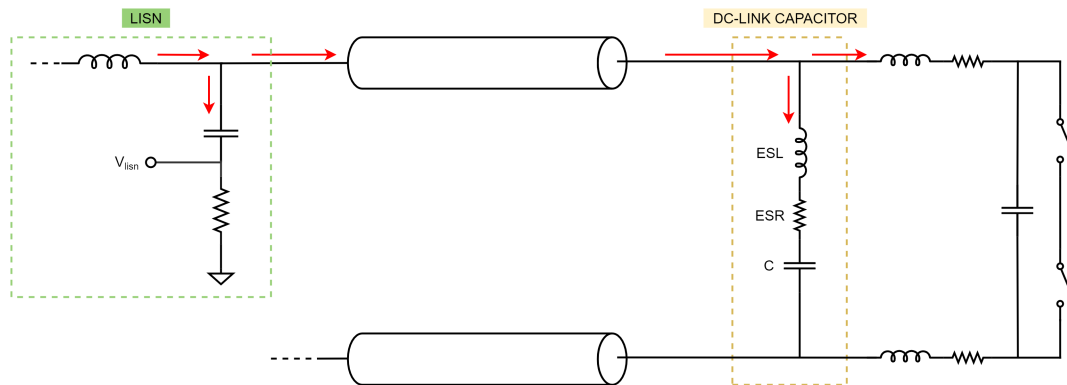


Figure 5.15: Effect of DC cables and ESL on the DM current path.

each $50 \mu\text{F}$ capacitor is 15 nH , but 3 nH have been also added to consider any other possible inductive contribute on the same conductive path, finding an equivalent ESL contribution given by:

$$ESL_{eq} = \frac{15 \text{ nH} + 3 \text{ nH}}{4} \quad (5.14)$$

As a consequence of these effects, the shape of the LISN spectrum measurement is remarkably changed. From now on, it will be evaluated the DM and CM emissions separately by using the schematic shown in Figure 5.16. The "SensePlus" and

"SenseMinus" labels are connected, respectively, to the measurement port of the LISNs. Figure 5.17 shows a comparison between the DM emission measured with

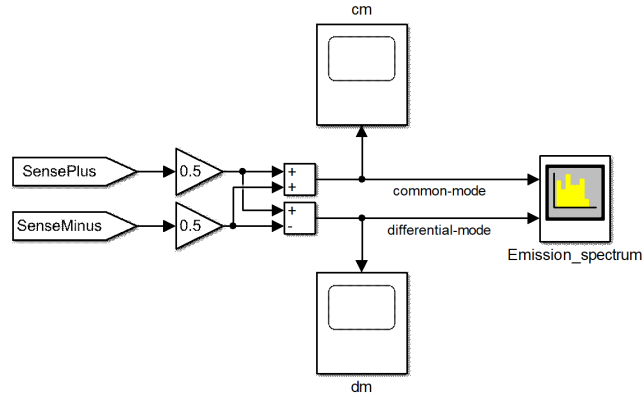


Figure 5.16: Separation of the DM and CM emission spectra.

and without the cables and the ESL. This is a very important result since, for the

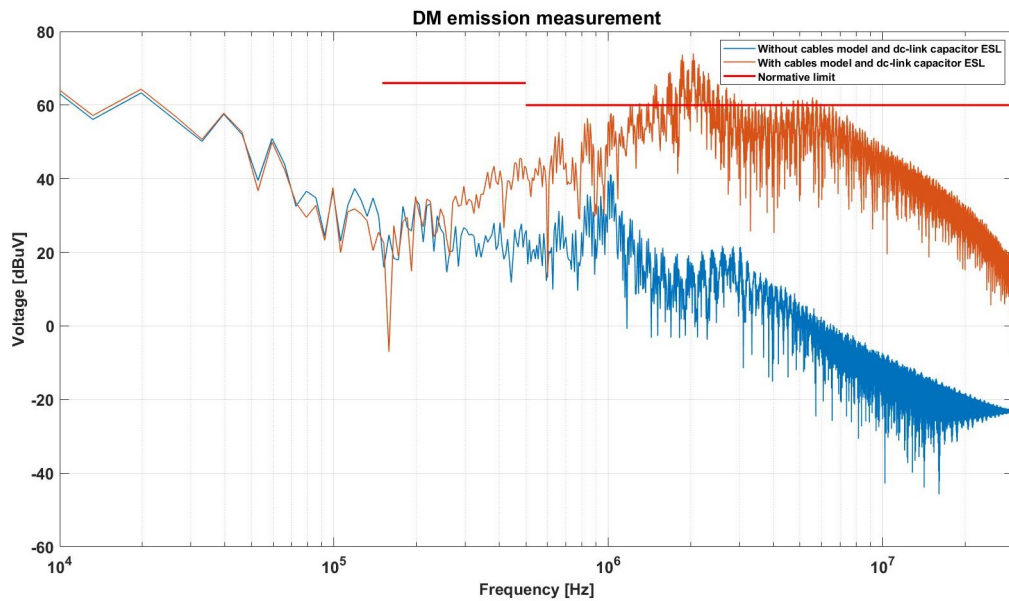


Figure 5.17: Effect of cables model and dc-link capacitor ESL on the DM emission measurement.

first time, the measured spectrum exceeds the normative limit. Even though other emissions contributions are still missing, a filtering action is already needed.

Since the presence of the dc-link ESL is fundamental on the DM spectrum, it has been conducted a parametric analysis of its value and its influence on DM emission is shown in Figure 5.18. The spectra show that in absence of ESL much

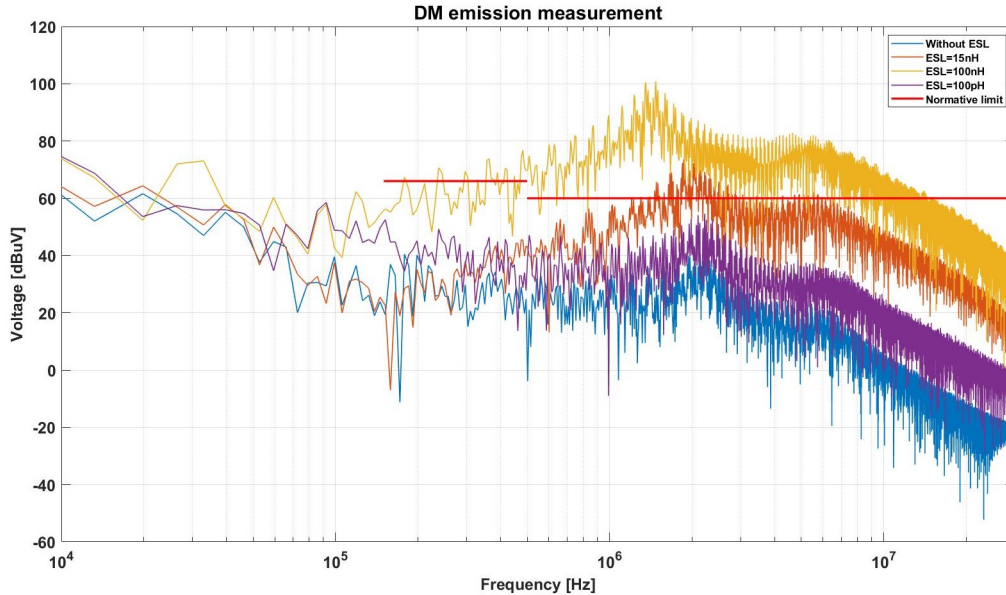


Figure 5.18: Effect of dc-link capacitor ESL value on the DM emission.

more current went to dc-link rather than entering into the LISN. By increasing the ESL value, instead, a higher current is provided to the LISN and a higher DM emission is measured.

The cables model does not only affect DM disturbances but, on the contrary, the CM emission became dominant. As seen before, the CM emission is related to the parasitic current flowing towards the reference. The cables insertion on the model takes into account the coupling paths introduced between the cable shields and the reference. In particular, these paths are due to the capacitive coupling C_{sn} and the physical connection $L_{sn,conn}$. Until now, the CM contribution was negligible, but now the CM emission is dominant over the DM one as shown in Figure 5.19, where both the DM and CM spectra have been reported. In literature, is quite common to find CM emission levels higher than around 20 dBuV the ones of DM emission. It follows that the total spectrum seen on the LISN measurement port is almost identical to the CM, as shown in Figure 5.20. As a consequence, it is expected that during the filter design the CM attenuation will be more critical than the DM one.

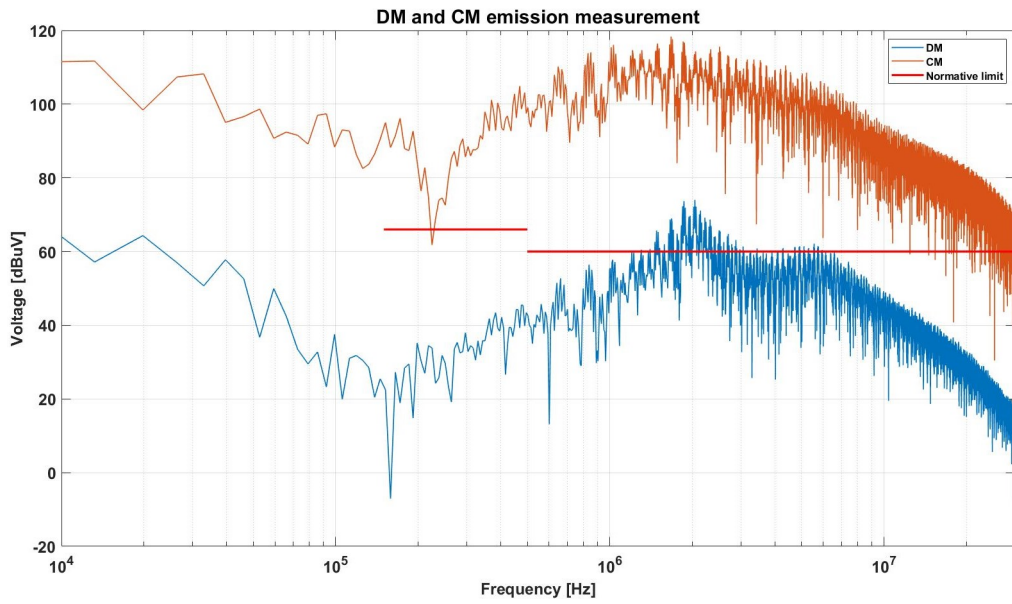


Figure 5.19: DM and CM emissions including cables model and dc-link capacitor ESL.

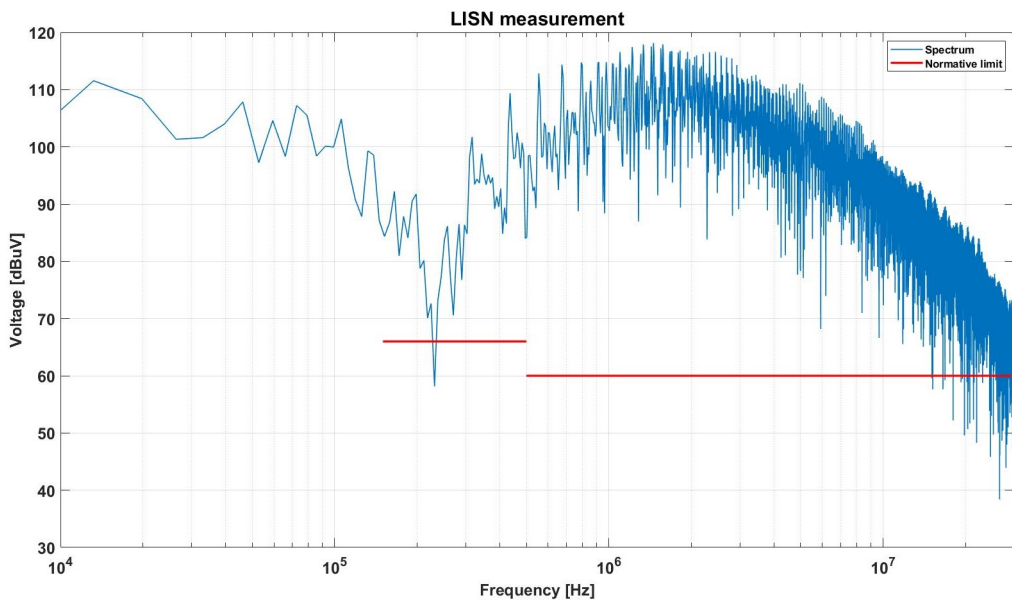


Figure 5.20: LISN measurement including cables model and dc-link capacitor ESL.

5.5 Worst case analysis

The insertion of the cables inside the model was a fundamental step for the prediction of the emission spectrum. On the other side, it could depend also on the operating point settings. For this reason, a parametric analysis has been conducted looking at the effect of the system parameters on both DM and CM measurements. In this way, it is possible to fix the operating point and to design the filter considering the worst case in terms of conducted emissions.

5.5.1 Motor speed

First of all, it was seen the influence of the motor speed remembering that it is a tunable parameter in the script on Appendix A, while the amplitude modulation factor m_a is computed in the function of the speed. For this reason, the spectrum has been evaluated in the three situations reported in Table 5.6, where the speed has been tuned while m_a is changed accordingly. These values have been chosen considering that the inverter should not operate in an overmodulation region and then a speed higher than 200 rpm (nominal speed) has been not considered. Since

Speed	m_a
50 rpm	0.22
125 rpm	0.5
200 rpm	0.77

Table 5.6: Values used for motor speed tuning.

the compared spectra are very close to each other, their positive envelopes are shown for both DM and CM contributions in Figure 5.21. The envelopes of spectra have been calculated by using the envelope function on Matlab setting the windows with 5 samples each. The result shows that the motor speed is not one of the key parameters for the EMC analysis. The CM spectrum is practically numb on the speed variation since it is not related to the nominal behavior of the system. Also, the DM spectrum does not suffer from big differences in the three cases, but the 200 rpm case seems to exhibit higher peaks than the other two cases. Nevertheless, its influence is quite negligible given the final design of the filter.

5.5.2 Carrier frequency

Further analysis has been performed by looking at the influence of the carrier frequency. Remembering that the carrier frequency, in this work, is variable between 10 kHz and 15 kHz, these two values have been selected. The envelopes

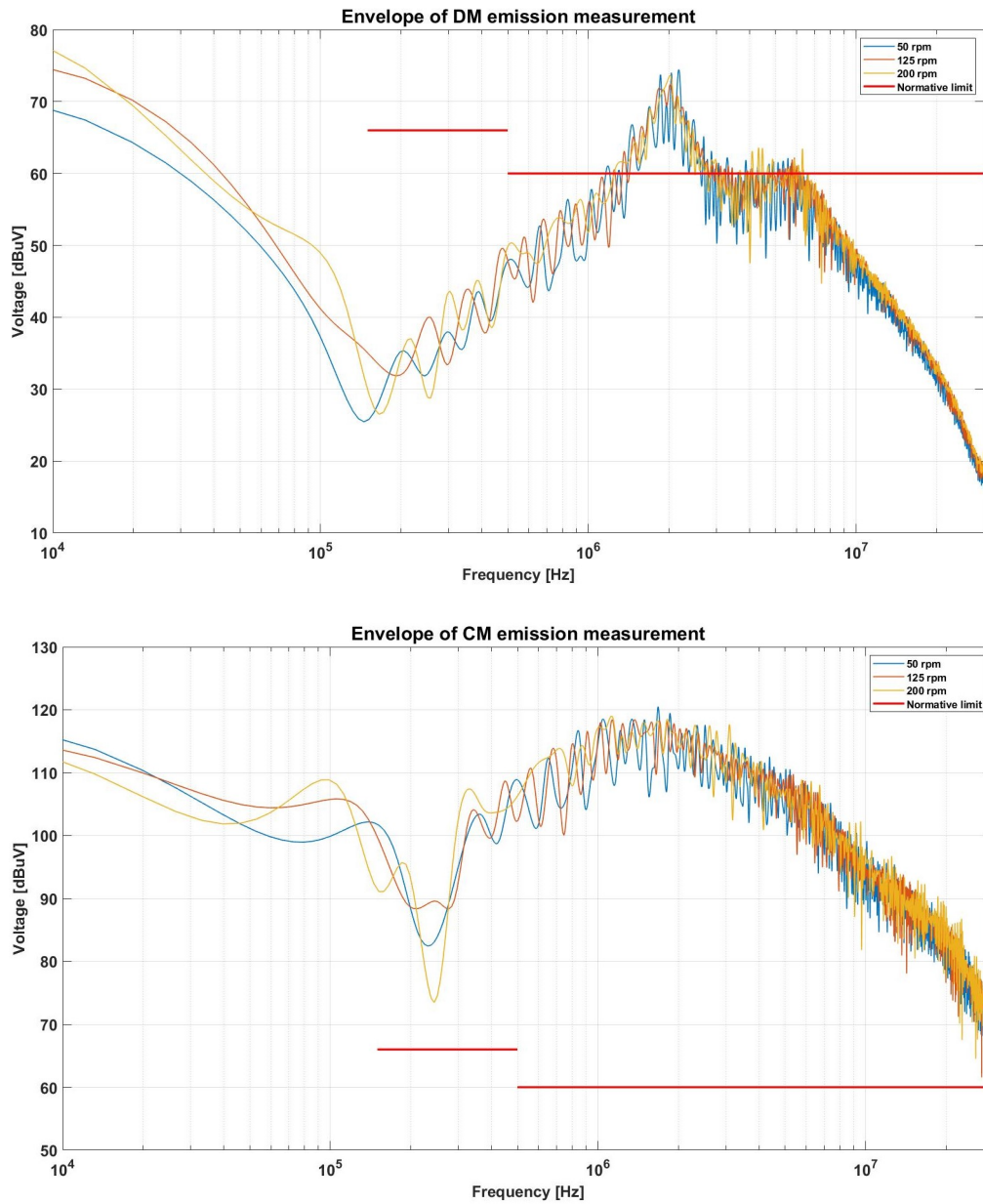


Figure 5.21: Effect of the motor speed on positive envelope of the DM and CM emissions.

of both DM and CM spectra have been compared in Figure 5.22. As before, the shape of the spectrum is similar in the compared cases. However, both the DM and CM envelopes are slightly higher using a $f_{sw} = 15$ kHz carrier rather than $f_{sw} = 10$ kHz. This phenomenon occurs since the frequency behavior of the signal,

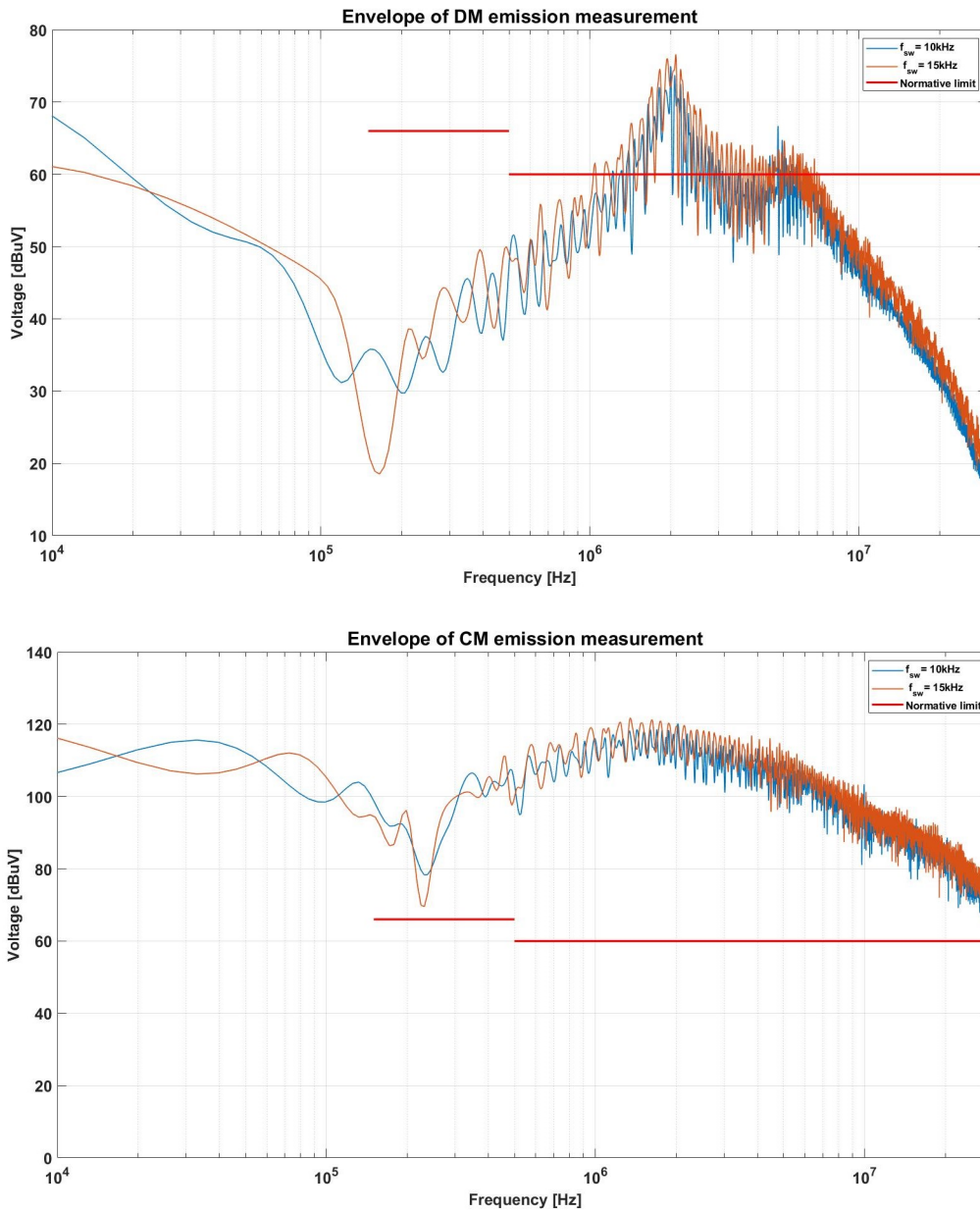


Figure 5.22: Effect of the switching frequency on positive envelope of the DM and CM emissions.

in general, is composed of harmonic components on the carrier frequency and at its multiples. By using $f_{sw} = 10 \text{ kHz}$, the minimum frequency of the normative limit ($f_{min} = 150 \text{ kHz}$) corresponds to the 15th harmonic of the analyzed signal.

If $f_{sw} = 15$ kHz is used, instead, f_{min} corresponds to the 10th harmonic. The harmonic amplitude generally decreases as the harmonic order grows and, for this reason, it is clear that using a higher carrier corresponds to a worst-case in terms of measured emissions. Since the harmonic order is very high it does not have a very large influence on the emission level and the difference is very small.

5.5.3 Shields grounding

One of the main sources of CM current is the connection between the cables shields and the reference conductor, modeled with the $L_{sn,conn}$ inductance. This connection is mandatory so that the shielding effect acts properly. Nevertheless, their effect on conducted emissions is exactly the opposite since a further path for the CM current is created. To confirm this concept, an analysis has been performed looking at the EM emissions behavior when the shields are connected on both sides, on only one side, or not connected at all. This last situation has been implemented by using the *Open circuit* component available on Simscape. When only one side is connected, the "inverter side" has been considered since it is the one closer to the emission source. The comparison of these three situation has been shown in Figure 5.23. As expected, the shield connection doesn't affect the DM spectrum, while the CM emission is strongly dependent on it. Connecting only one side doesn't provide many advantages, while not connecting the shield to reference reduces the CM emissions of around 20 dB until 5 MHz. Such a reduction of the CM spectrum should help remarkably the filter design, allowing to get less stringent specifications both in terms of attenuation level and frequency. However, keeping in mind that the shielding connection is necessary and wanting to consider the worst case for a reliable filter design, the model has been kept unaltered with both connections towards reference. Later on, a different possibility will be studied for the shielding connection.

5.5.4 Line sections

Previously, the length of each line section of cables model has been set to 0.5 m dividing the wavelength by 10. Sometimes, using a smaller length help to obtain more reliable and precise results. For this reason, Δ_z has been decreased to:

$$\Delta_z = \frac{\lambda}{20} = 0.25 \text{ m} \quad (5.15)$$

In this case the number of sections is the doubled than the ones reported on Table 5.4. The two situations have been compared and the result is shown in Figure 5.24. The result shows that both the DM and CM spectrum levels are very similar using $\Delta_z = 0.5$ m or $\Delta_z = 0.25$ m. For this reason, since the model results are reliable

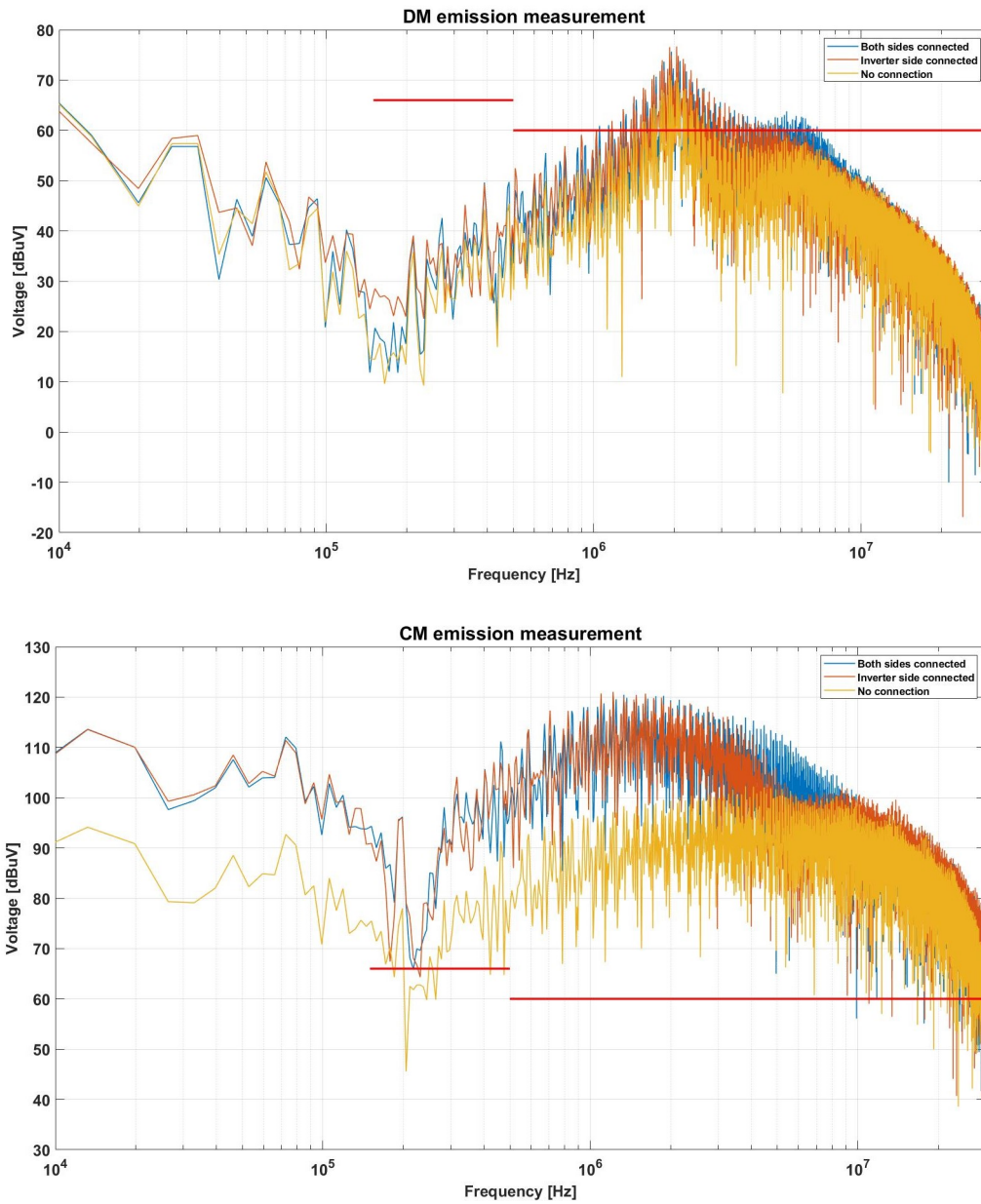


Figure 5.23: Effect of the connection between shield and reference on the DM and CM emissions.

using the number of line sections considered until now, the line section has been left unchanged at $\Delta_z = 0.5$ m, allowing to reduce the simulation time and the model complexity.

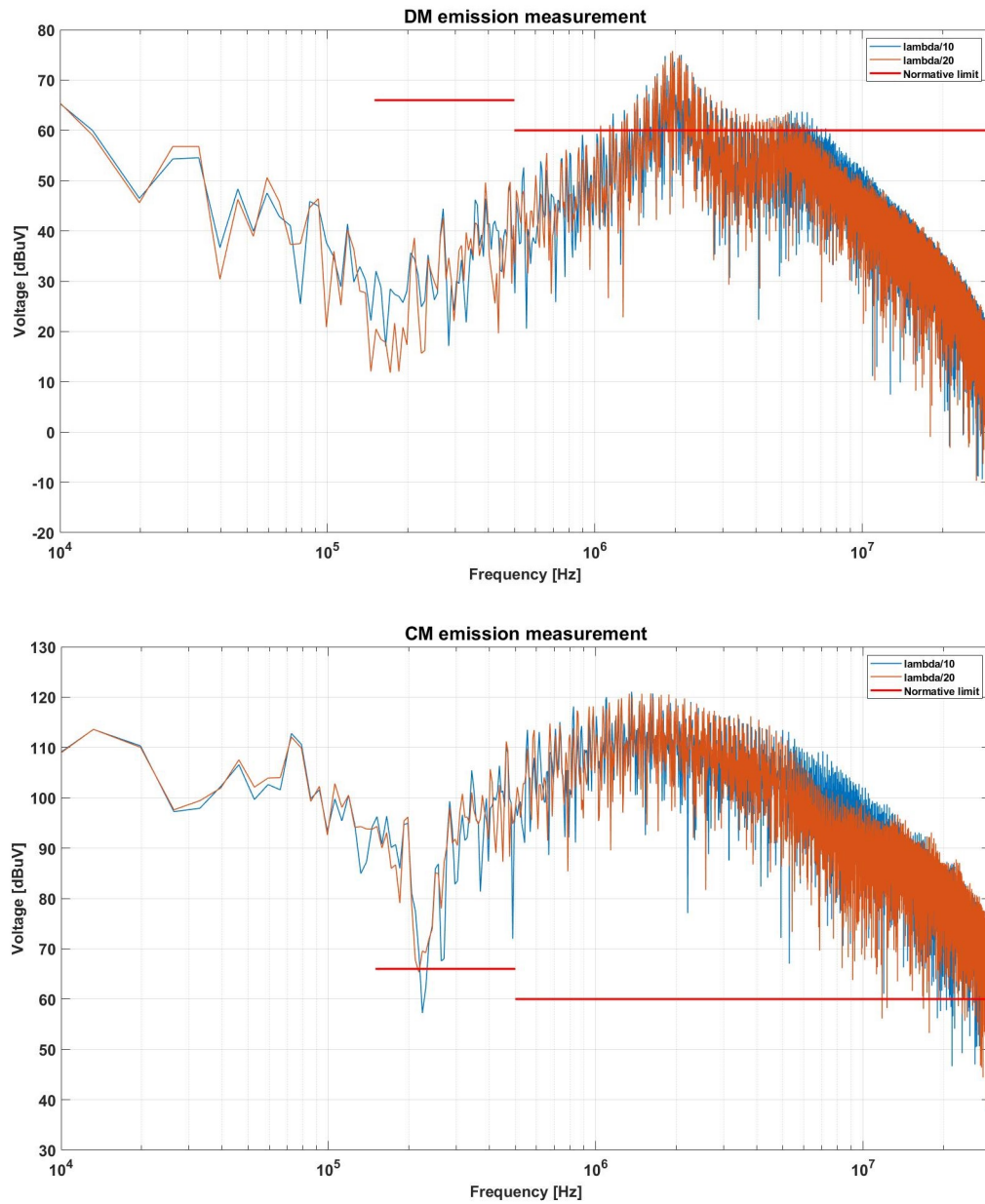


Figure 5.24: Effect of the line section length on the DM and CM emissions.

5.5.5 Sampling rate

Until now, the solver sampling rate of the model has been set to the Nyquist frequency, allowing to get a trade-off between the necessity to look until 30 MHz and to have acceptable simulation time and complexity. Now, wanting to obtain

even more reliable results, the sampling rate has been increased up to $10f_{max}$, seeing how the DM and CM spectra change. The comparison between the results get with these two different situations is shown in Figure 5.25. As expected, increasing the

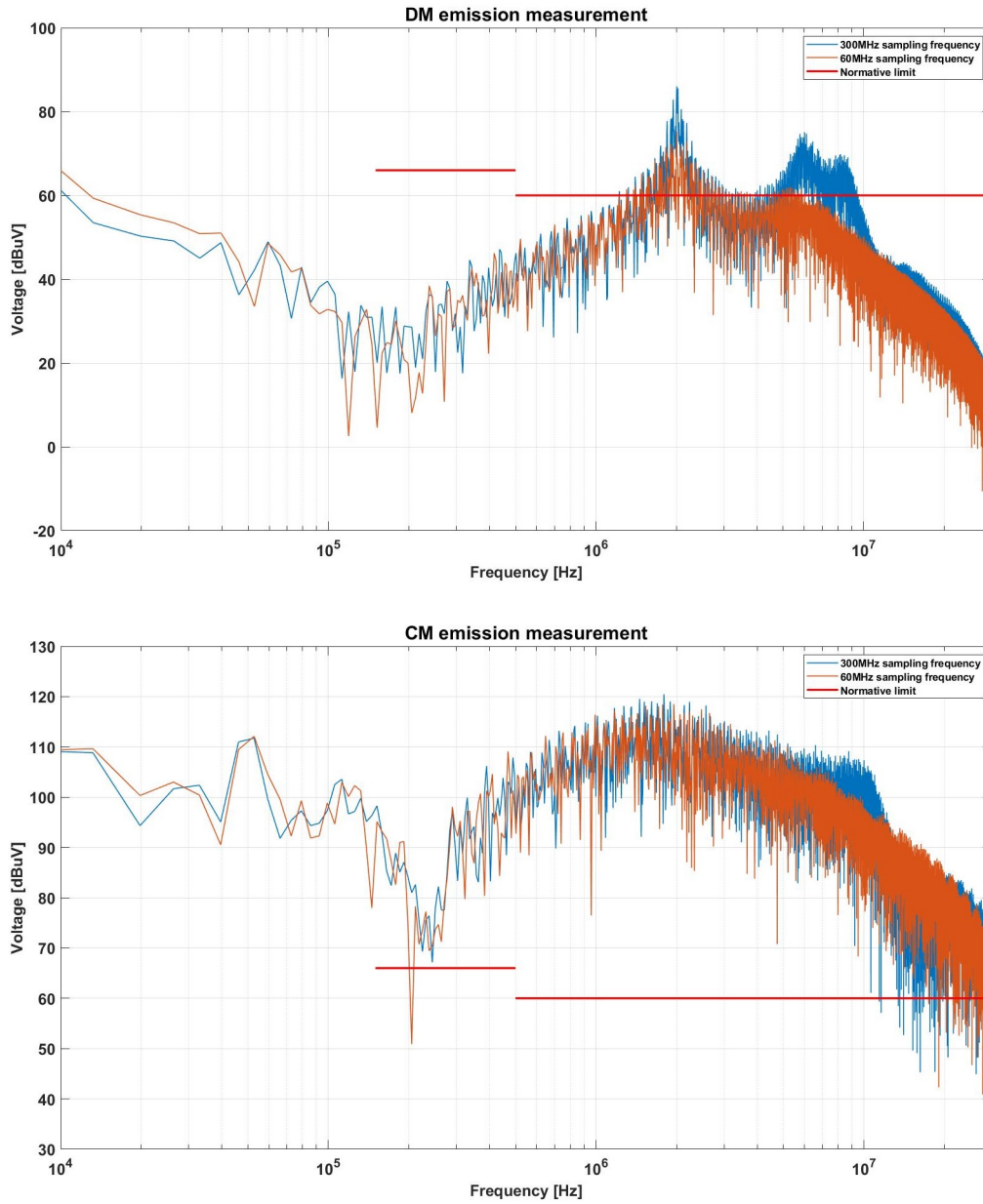


Figure 5.25: Effect of the solver sample rate on the DM and CM emissions.

sampling rate allows getting more precise results, especially on the measurement of the peak. This is visible on DM emission comparison, in which $f_s = 10f_{max}$ allows

to display the peaks at about 5.5 MHz and 8.5 MHz, which were only partially visible using the Nyquist frequency. This result is very important since it suggests that using a high sample rate will be fundamental on the final spectrum estimation since it influences the attenuation requirement for the EMI filter, which will be designed by looking at the results get with $f_s = 10f_{max}$.

Chapter 6

Simulation of the systems

After the implementation of the model of the tedder system with a single inverter, it has been completed by including all the four "branches", that are all identical to each other. For this reason, the model presented above has been replicated four times as shown in Figure 3.5 in Chapter 3, obtaining the so-called "quadruple configuration" instead of the "single configuration" seen until now.

Having implemented the full tedder system model, the DM and CM spectra have been evaluated and compared with the ones of the single configuration in Figure 6.1. As expected, being the amount of power involved on quadruple configuration four times the one included on the single one, the level of the spectra envelope is increased for both DM and CM emissions of around 12 dB, corresponding to a multiplication by four on linear scale. The result shows even a peak of 130 dBuV on CM emission spectrum, corresponding to a required attenuation of 70 dBuV for the EMI filter. Since the amount of required attenuation on quadruple configuration becomes quite critical, a smart strategy has been studied to reduce the emission levels without changing the circuit topology.

6.1 Carriers phase shift

The following analysis is based on the interleaving strategy employed on switching power converters. Parallel operation of PWM inverters is widely used in various applications to reduce system development costs and to provide easy power scalability. In this kind of application, the interleaving strategy allows eliminating certain harmonics and their sideband components in three-phase motor drives, reducing EMI attenuation requirements by around 6-8 dB and resulting in a significant reduction of both DM and CM filter size and weight [26]. For example, let's consider the situation shown in Figure 6.2, in which are represented three parallel inverters driving a common induction motor. In literature, several kinds of interleaving are

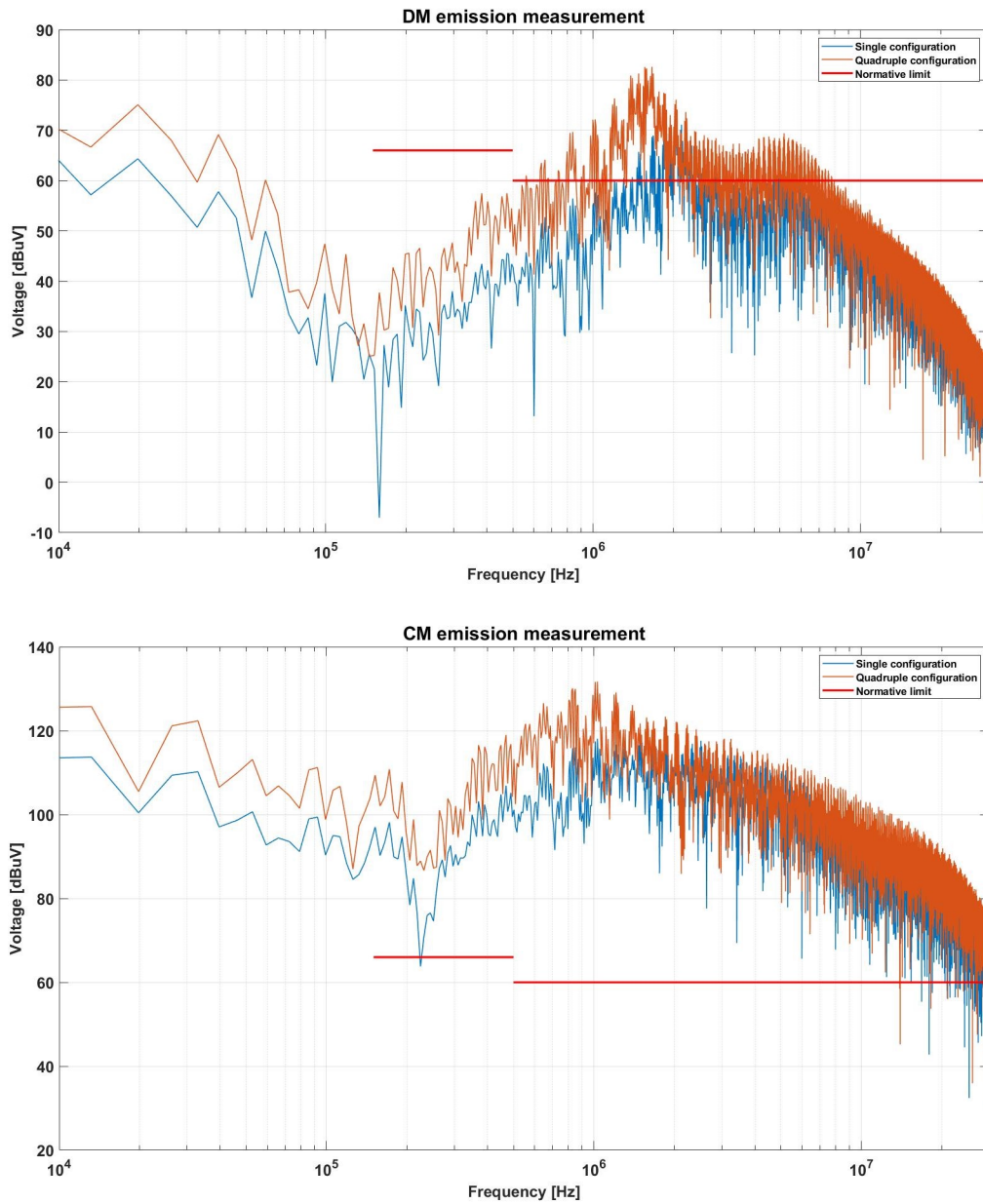


Figure 6.1: Comparison of the DM and CM emissions between single and quadruple configurations.

shown. In general, the interleaving is applied by inserting a phase shift of the carrier of the PWM algorithm and the amount of shift depends on the kind of interleaving employed. Supposing to have N power converters in parallel, the most

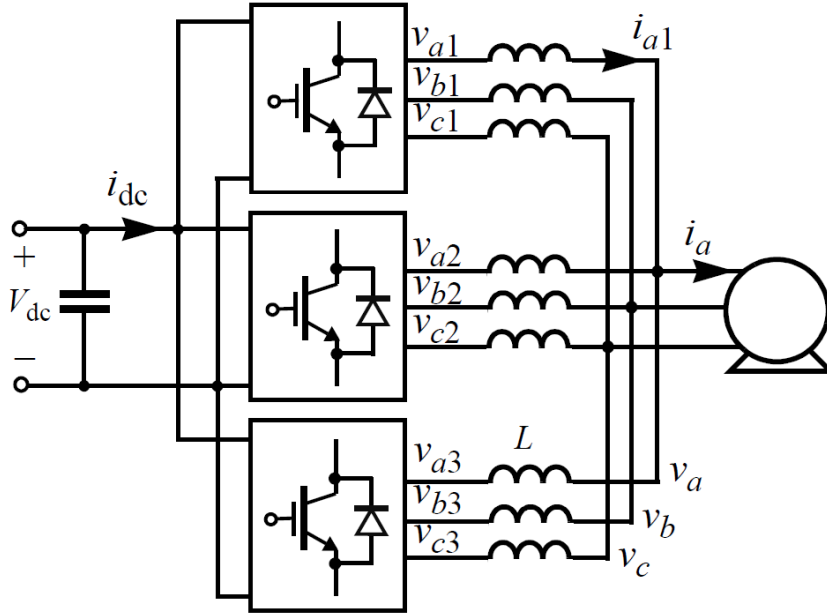


Figure 6.2: Three parallel inverters with common supply and driving a common induction motor [26].

common strategies are the symmetric and asymmetric interleaving:

- Traditional symmetric interleaving (Figure 6.3a) acts by introducing a phase shift of the carrier signals equal to $1/N$ of a whole carrier cycle:

$$\phi_{ck} = \frac{2\pi(k-1)}{N} + \phi_{c1} \text{ for } k = 1, 2, \dots, N \quad (6.1)$$

The main advantage of symmetric interleaving is the elimination of carrier harmonics and their sidebands that are not centered at N multiples of the carrier frequency.

- The asymmetric interleaving can be divided into regular or irregular. In regular asymmetric interleaving (Figure 6.3b) the carrier phase shift is constant between the adjacent converters but is different from $1/N$ of a carrier cycle:

$$\phi_{ck} = \frac{\Delta\phi_c(k-1)}{N} + \phi_{c1} \text{ for } k = 1, 2, \dots, N \quad (6.2)$$

In irregular asymmetric interleaving (Figure 6.3c), instead, the phase shifts between adjacent modules are not fixed, but they can vary freely. This last solution, due to its unpredictability, has been not used in this analysis. The

asymmetric interleaving allows introducing an additional degree of freedom, which can be optimally selected to obtain the elimination of certain harmonics characterized by system resonance.

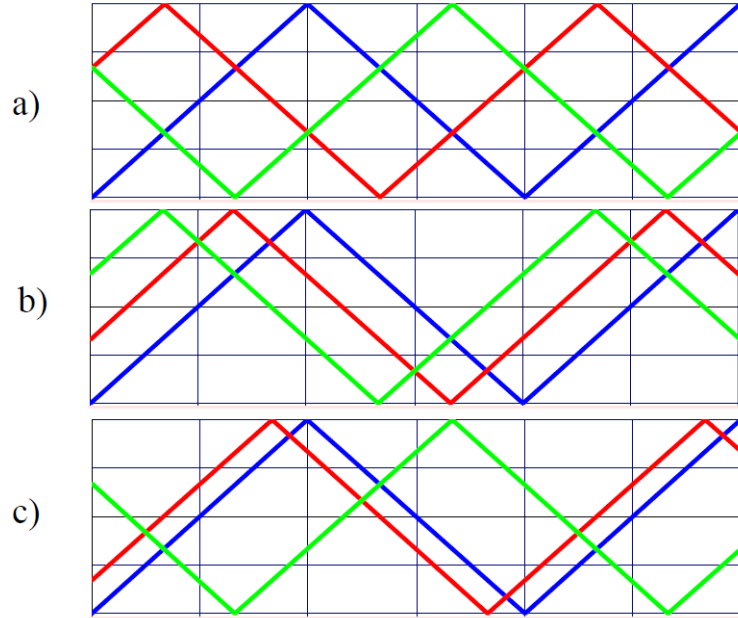


Figure 6.3: Generic carrier signals for a) symmetric interleaving, b) regular asymmetric interleaving and c) irregular asymmetric interleaving [26].

The system analyzed in this work is quite different from the one shown in Figure 6.2, since it doesn't include a parallel operation of the inverters, while they share the same DC supply but operate on four separated PMSM. For this reason, talking about interleaving is not formally corrected and this strategy has been named as "carriers phase shift". Three different phase shifts of the carriers have been used, as shown in Table 6.1. In symmetric case, the carriers have been set with a

	ϕ_{c1}	ϕ_{c2}	ϕ_{c3}	ϕ_{c4}
Symmetric	0°	90°	180°	270°
Symmetric "in pairs"	0°	180°	0°	180°
Asymmetric	0°	22.5°	30°	45°

Table 6.1: Phase shift of the carriers.

phase shift constant between the adjacent signals, as shown in Equation 6.1. The symmetric "in pairs" is realized by applying the symmetric strategy to the first

two carriers and then the other two, separately. For the asymmetric analysis, instead, a cycle of $\Delta\phi_c = 45^\circ$ has been used. All these three cases were individually compared with the situation in which the phase shift is not applied at all, judging whether the phase shift is helpful or not in terms of EMC, obtaining as reported in Figure 6.4. This analysis suggests that using the phase shift of the carriers provides

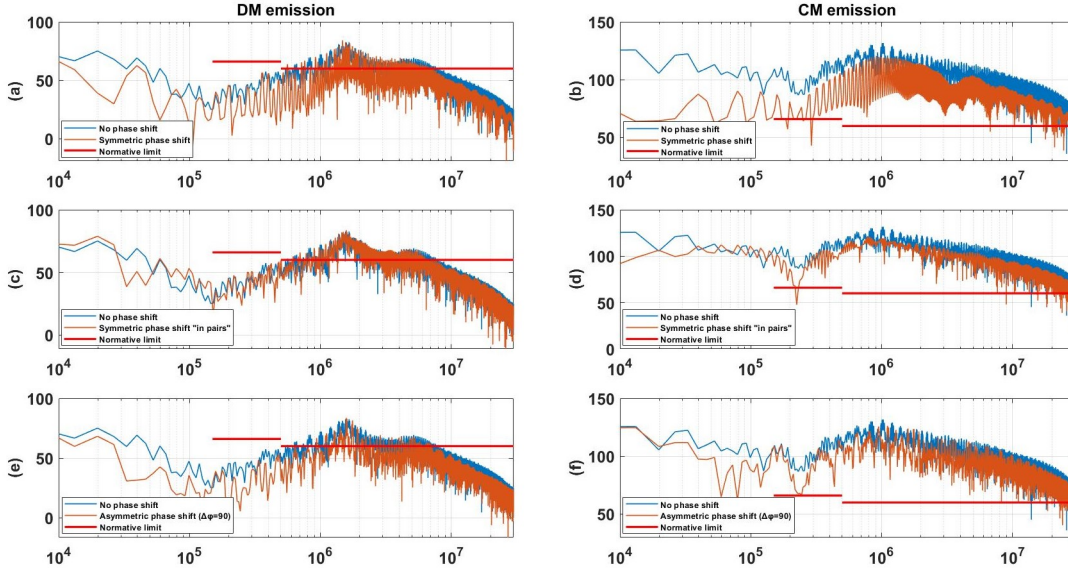


Figure 6.4: Emission comparison between no phase shift and a,b) Symmetric shift, c,d) Symmetric shift "in pairs" and e,f) Asymmetric shift.

always a reduction of the emission levels. For this reason, any shifting strategy is a good solution in terms of EMC, allowing to reduce the required attenuation and then to make a less complex filter. In particular, the symmetric shift "in pairs" is the only one that does not provide many improvements on the DM emission spectrum, unlike the other two strategies, and for this reason, it was discarded. To obtain a better comparison between the symmetric and the asymmetric phase shift, instead, their emission levels have been compared in Figure 6.5. The spectra of DM emission are practically identical while using asymmetric phase shift instead of an asymmetric one provides CM emission levels lower in the whole range of frequencies of interest. Looking at the spectrum in the symmetric case, also, it is visible that the shape is changed: as expected, the only harmonics present are centered at $N = 4$ multiples of the carrier frequency $f_{sw} = 10$ kHz employed on these simulations. To conclude this analysis, applying a phase shift on the carrier signals is always a good solution from the EMC point of view and the symmetric shifting technique is the more advantageous between the ones analyzed. For this reason, this kind of phase shift has been fixed for the model and for the following

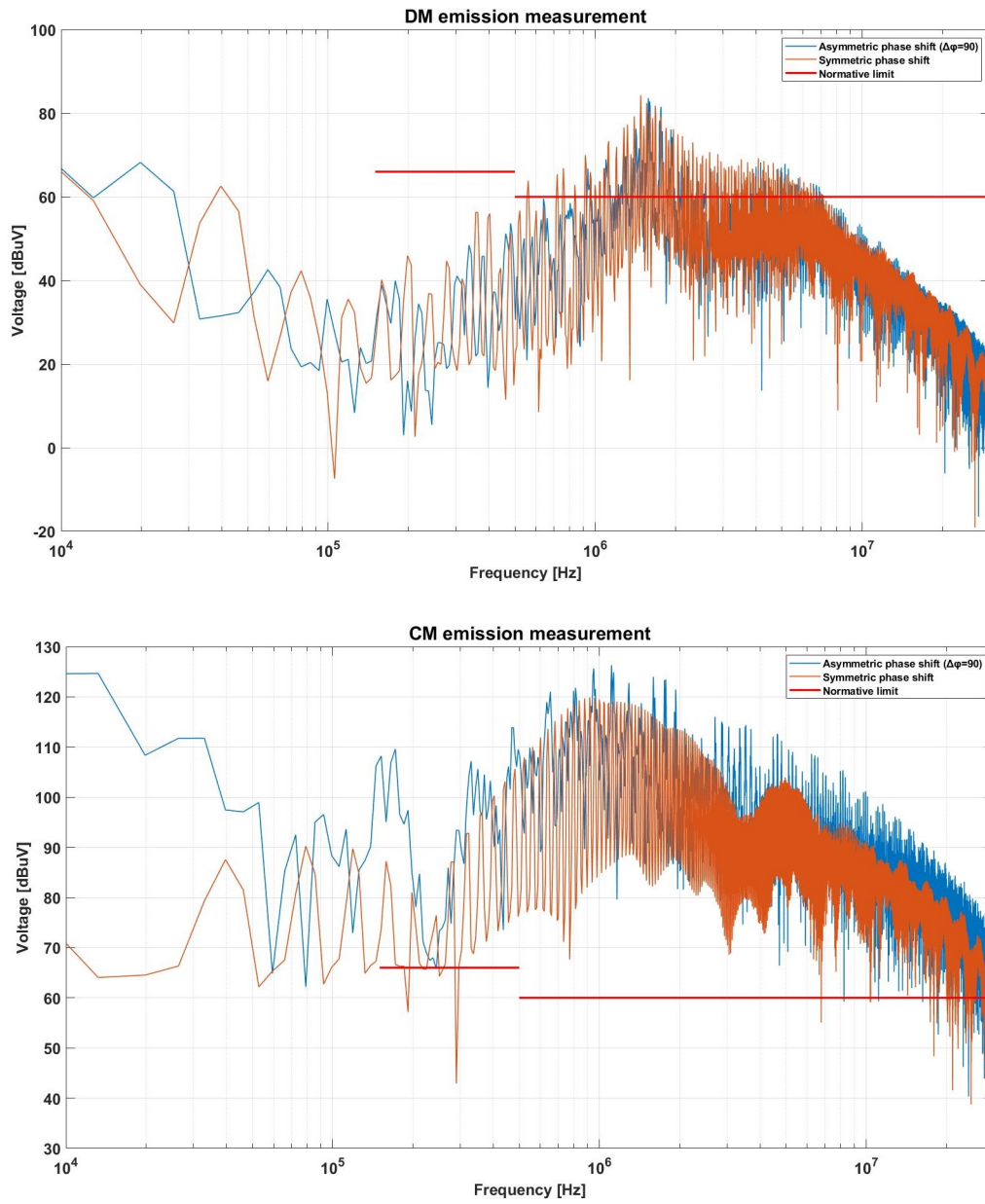


Figure 6.5: Comparison between symmetric and asymmetric phase shift on the DM and CM emissions.

simulations.

6.2 Distance between cables

An analysis has been also performed looking at the influence of the cable arrangement in the measured spectra. In particular, in this section, it is supposed to move the cable closer to each other. Until now, it has been supposed to have a distance of $D = 10$ cm between the cables. Now, it is desired to understand how the spectrum changes if the cables are approached at a distance of $D = 3$ cm. The effect of this change is shown in Figure 6.6. The result shows that, in general, the emission level is increased by approaching the cables of each other. However, this variation is small enough to understand that the filter design deriving from this model can be used also if the actual measurement setup is slightly different from the one described in this analysis. In any case, to consider the worst case, the distance of the cables has been reduced and fixed to $D = 3$ cm.

6.3 Final model setup

Finally, the last step to conclude the model concerns the introduction of the device enclosures and the insulating support. In particular, it is important to see how the presence of these elements can influence the LISN measurement and then the EMI filter design.

With enclosures, it is referred to the metallic cases used for both the inverter and the motor in their final form. These metallic cases act as a shield from and to the surrounding environment. For security reasons, all the metallic components must be grounded and on the final application, it is planned to connect the cases to the reference by placing them directly on it. In this way, the inductive connection between the cases and the reference is practically ideal, leading to a negligible grounding impedance. One of the advantages of the metallic cases, from the practical point of view, is that they provide a more accessible point to make the ground connection of the cable shields. In particular, the shield on the inverter side of DC and three-phase cables can be connected directly to the inverter case while the shield on the motor side of the three-phase cables can be connected to the PMSM case. This operation allows for a possible reduction of the inductive path of the CM current and, eventually, to a reduction of the overall CM emission level. On the other side, the insulating support is mandatory on the measurement setup imposed by the normative and must be put between the reference plane and the DC cables and the inverter. This insulating support must have a thickness of 10 cm and it is supposed to use a plate of wood. As a consequence, the model setup has been changed into the one shown in Figure 6.7. In particular, there are several differences compared to the previous configuration.

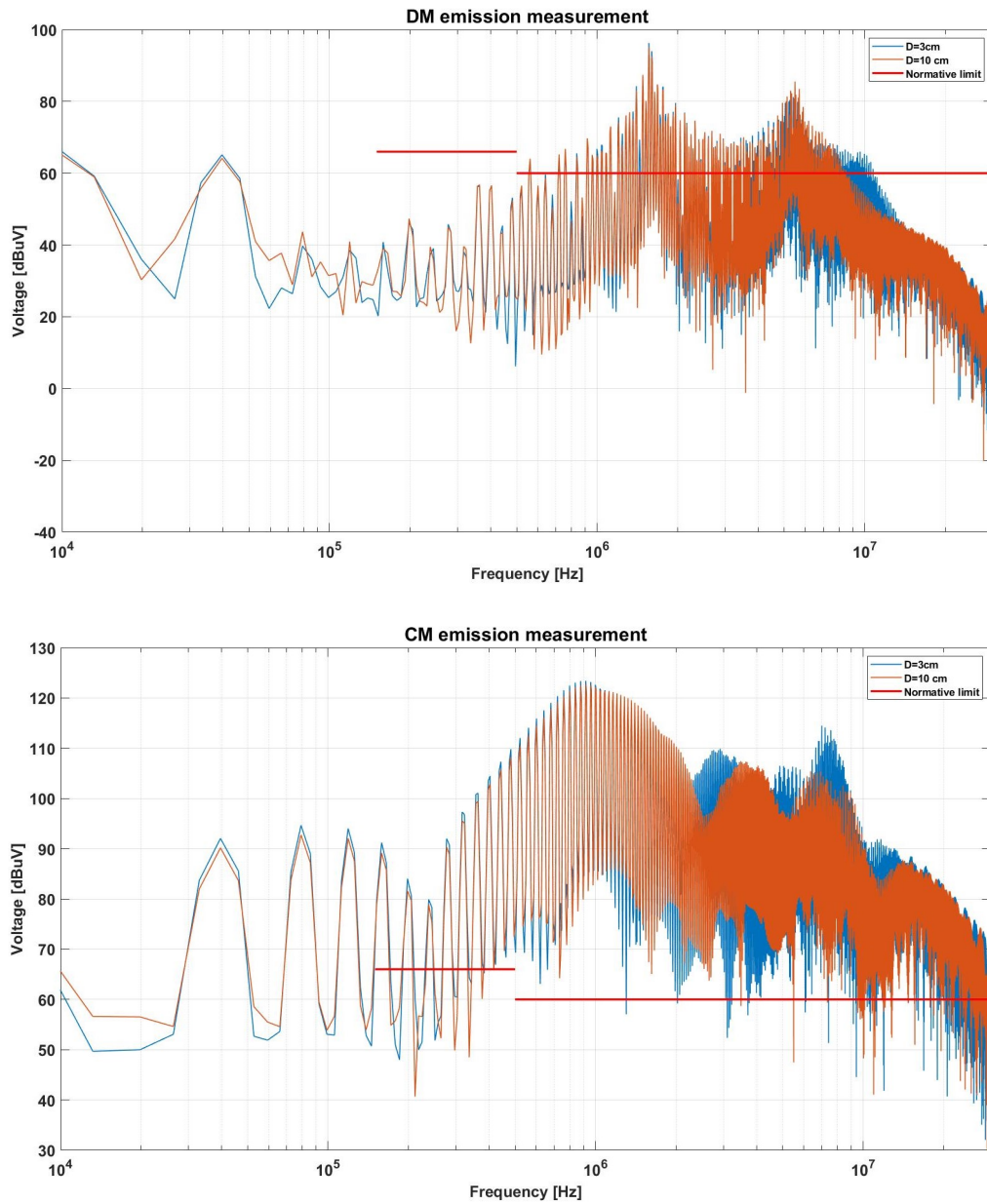


Figure 6.6: Effect of the distance between cables on the DM and CM emissions.

Inverter capacitive coupling with case

For first, it is necessary to consider the capacitive coupling of DC+, DC- and phase nodes with the inverter case, represented in red on Figure 6.7. In literature, these capacitive couplings can vary from some pF to a few hundred pF. To estimate

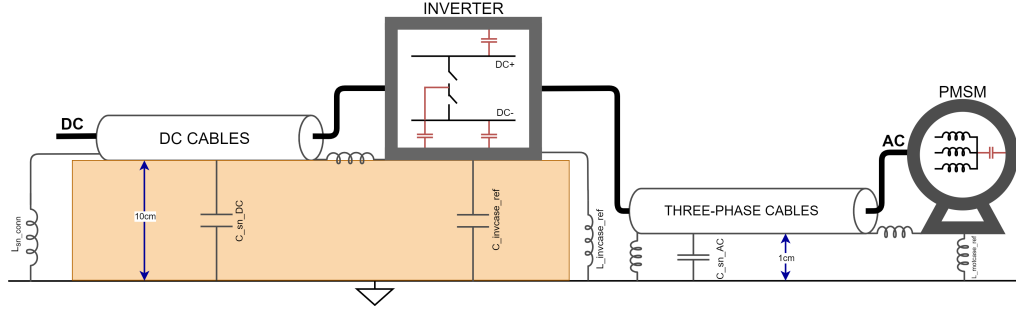


Figure 6.7: Measurement setup with the insertion of the insulator and enclosures.

the value of the parasitic capacitance, on first approximation, it was used the distance $d = 50 \mu\text{m}$ between the SiC MOSFET and the heat sink, which is in turn connected to the case and to the reference. The capacitance has been estimated by supposing a parallel-plate capacitor given by the area of the SiC MOSFET $A = 1 \text{ cm}^2$ and a plate of Kapton used as an insulator between the SiC and the heat sink. Remembering that the Kapton has a relative dielectric constant equal to $\epsilon_{r,k} = 3.4$, the capacitance is given by;

$$C_{coup,inv} = \epsilon_0 \epsilon_{r,k} \frac{d}{A} = 60 \text{ pF} \quad (6.3)$$

Anyway, a parametric analysis has been performed sweeping this value until 200 pF and judging that the changes in emission spectra are very small.

Inductive connection between inverter case and reference

Despite the inverter being placed on the wooden plate, its case must be connected to the reference. This connection has been modeled with an inductance of 1 nH/mm and a distance of 10 cm as imposed by the normative, getting a total inductance of:

$$L_{caseinv,ref} = 100 \text{ nH} \quad (6.4)$$

Capacitive coupling through the insulator

Due to the presence of the insulator, the capacitive couplings between the DC side cables and the reference are changed by multiplying them with the relative dielectric constant of the wood $\epsilon_{r,w} = 2.5$. On the other side, due to coupling between the inverter case and the insulator a new parasitic capacitance $C_{invcase,ref}$ is introduced on the model. Its value has been estimated considering a distance $d = 10 \text{ cm}$, the area of the inverter case experimentally measured and equal to

$A = 0.122 \cdot 0.278 \text{ m}^2$ and under the hypothesis of parallel-plate capacitor:

$$C_{caseinv,ref} = \epsilon_0 \epsilon_{r,w} \frac{d}{A} = 7.5 \text{ pF} \quad (6.5)$$

Shield connection

As said before, the presence of the metallic cases allows an easier connection between the cables shields and the reference. In Figure 6.7 the inverter/motor side of the DC/three-phase side cables have been directly connected to the inverter/motor cases, which are practically more accessible. Also, the distance of these connections has been reduced from 10 cm to a more realistic 5 cm, leading to:

$$L_{sn,conn} = 50 \text{ nH} \quad (6.6)$$

Three-phase cables and motor height

Until now it was supposed to place the three-phase cables and the PMSM at the same height as the DC side cables. Now, it is important to underline that they don't belong to the DUT and so they are not forced to stay on the insulator support. For this reason, a typical solution is to place them directly on the reference plane to reduce the parasitic effect towards the ground. In order to make a coherent computation, the height on AC side has been reduced from 10 cm to 1 cm. As a consequence, all the parasitic contributions towards reference on the three-phase side have been re-calculated accordingly.

Stator capacitive coupling

Another capacitive coupling to be included is the one between the star center of PMSM and its case. Unfortunately, the motors were not physically available during this thesis work and, for this reason, it was impossible to measure this capacitance or even make a geometric estimation. For this reason, its value has been estimated by looking at the information available in the literature. For example, in a 4 kW PMSM this capacitance has been measured as 300 pF [27], on a 400 W motor it is around 6 pF [28], while on a Medium Voltage DC (MVDC) power distribution systems it is even 6 nF [29]. Also, it was found that for PMSM on the power range considered on this work the capacitance between the star neutral point and the case is typically between 100 pF and 500 pF [30]. At first approximation, it has been used a capacitive coupling of 500 pF. To make a detailed model of a PMSM, other capacitive couplings should be included, as the interwinding and the phase-to-phase couplings. However, these couplings are quite lower than the one just included and, for this reason, they can be neglected in this analysis.

Looking at the previous and the current model configurations, there are two kinds of differences. The first is related to the coupling values, which are changed due to the different heights or to the presence of the insulator layer. The second, instead, is given by the presence of further coupling elements. The introduction of $L_{invcase,ref}$ and $C_{invcase,ref}$ forms a resonant circuit for the CM current with a resonant frequency given by:

$$f_{res} = \frac{1}{2\pi\sqrt{(L_{invcase,ref} \cdot C_{invcase,ref})}} = 183.7 \text{ MHz} \quad (6.7)$$

Due to this resonant behavior, it is expected to have a reduction of the CM emission at high frequencies. At this point, the new model setup has been simulated and then compared with the previous one, getting the DM and CM spectra shown in Figure 6.8. Figure 6.9, instead, shows the overall LISN measurement get with this final model setup. The variations are very small on the DM spectrum because almost all of the changes concerned the connections towards the reference. On the other side, the CM spectrum is unchanged at low frequencies, while the main difference is given at higher frequencies, where the emissions are reduced as expected. However, these changes don't heavily affect the EMI filter design as the peak emissions have remained nearly the same on both amplitude and frequency.

In order to make a more deep analysis on the effect of these new model parameters on the measured emission, some parametric analyses have been performed. The stator-case capacitance has been changed from 500 pF to 100 pF, which are the typical limit values as seen before [30]. It has been found that the effect on measured spectra is visible only at frequencies lower than 150 kHz and moreover it is quite negligible, while on the bandwidth of interest the behavior is almost identical.

Subsequently, the shield to inverter case connection has been reduced from 5 cm to 5 mm by decreasing the modeling inductance from 50 nH to 5 nH. Figure 6.10 shows that, as expected, the CM spectrum is slightly lower as going up in frequency.

Another topic analysis has regarded the shield connection. In the previous chapter, it was seen that not connecting the shield to the reference allows getting a 20 dB reduction of the CM emission level. Now, an alternative solution that can be employed is to connect the shields to the DC- conductor instead of to the inverter case, which being directly connected toward the reference is a big source of CM emission. In this way, the shields continue to act properly but, at the same time, the path of the CM current is changed. By implementing this alternative solution, the result on Figure 6.11 is obtained. As expected, the shape of the CM spectrum is remarkably changed and the most important result is that the first peak is reduced by around 20 dBuV and the second peak, at around 2 MHz, becomes the higher. This result suggests that connecting the shield to DC- allows a more relaxed EMI filter design and, in general, is a good choice to reduce the amount of emission

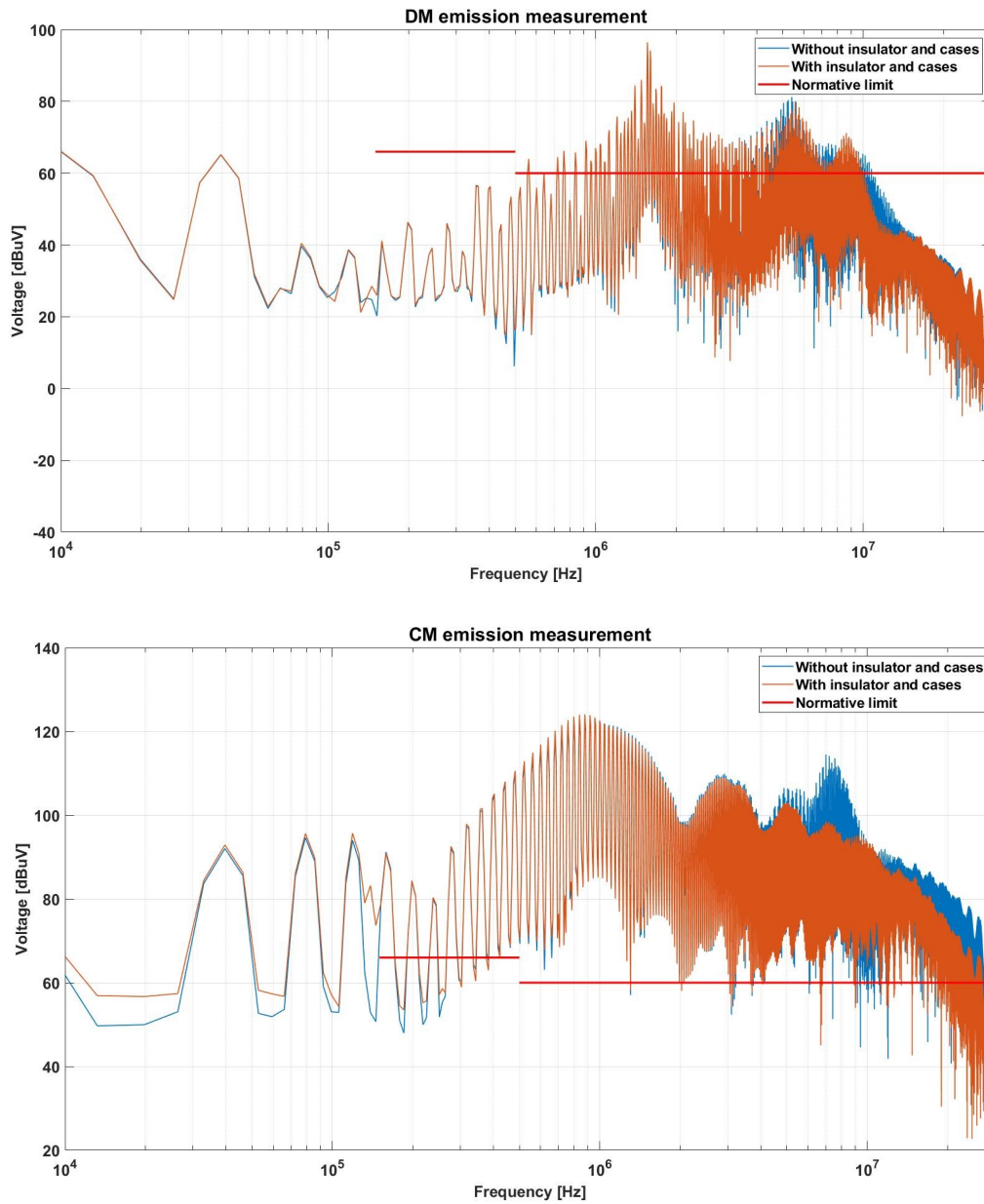


Figure 6.8: Effect of the insulating support and device enclosures on the DM and CM emissions.

acting on the measurement setup. Nevertheless, this analysis explores a solution that allow alternative paths to the CM current that do not involve the LISN. In most application these connections are unattainable in practice, because standard

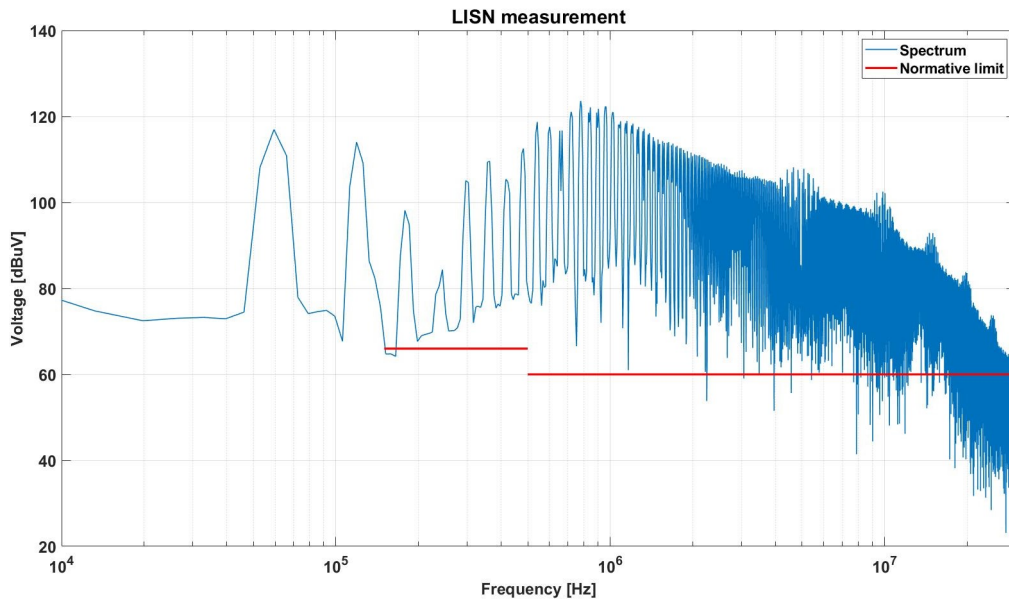


Figure 6.9: LISN measurement of the tedder system.

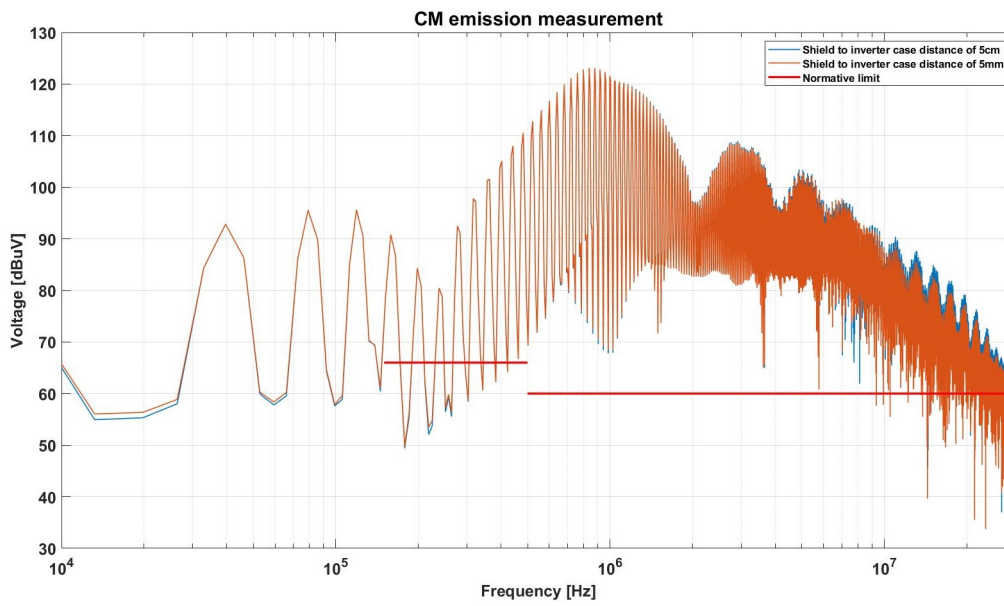


Figure 6.10: Effect of the distance between cable shields and inverter case on the CM spectrum.

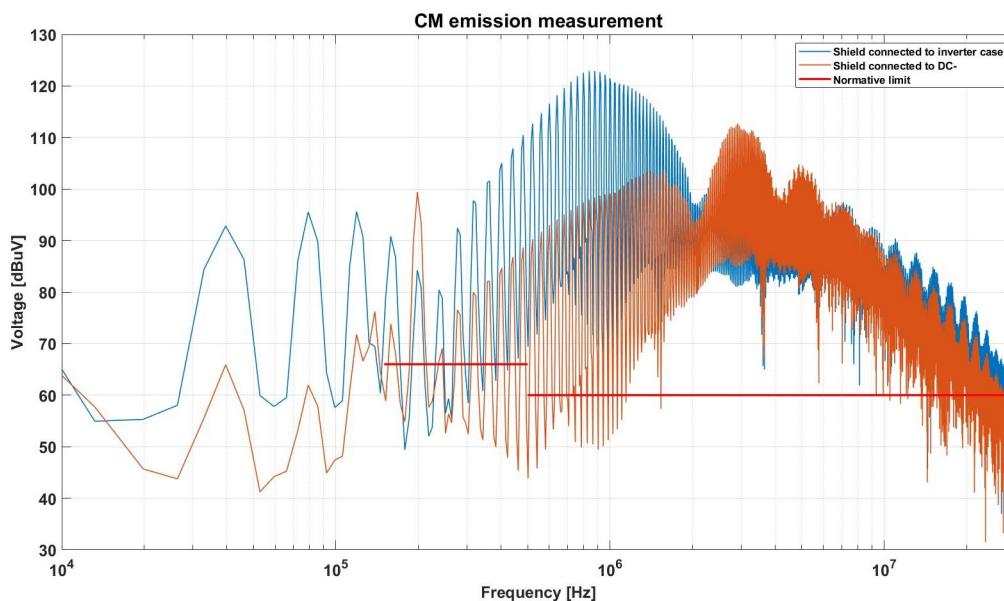


Figure 6.11: Effect of the shield connection to DC- instead of inverter case on the DM and CM emissions.

case connectors force to bond the shields to the metallic case. Furthermore, it is important to comply the safety regulations regarding the shield connections [31].

6.4 DM emission on time domain

A final analysis regards the spikes present on the DM spectrum since they are related to the nominal behavior of the system. The final DM spectrum is the one shown in Figure 6.12, where its peaks have been highlighted. To analyze these peaks in the time domain, the behaviors of the "U phase" voltage and the input switching current have been evaluated. Figure 6.13 shows a zoomed view of their waveforms, highlighting the sources of peaks on emission measurement. The characteristic frequencies have been identified by looking around the commutation of the "U" voltage. When there is no commutation of any MOSFET, both current and phase voltage have a sinusoidal behavior with 1.5 MHz frequency around their mean value. This behavior is clearly visible on input current shown in Figure 6.13, but not on phase voltages since these oscillations have an amplitude on the order of 1 V or even less. Since the commutation has not yet occurred, these oscillations are due to the non-ideality introduced on positive and negative conductors, such as the PCB traces and the cables parasitics. After the commutation, instead, the oscillations at 5.5 MHz occurs and are clearly visible on both input current and

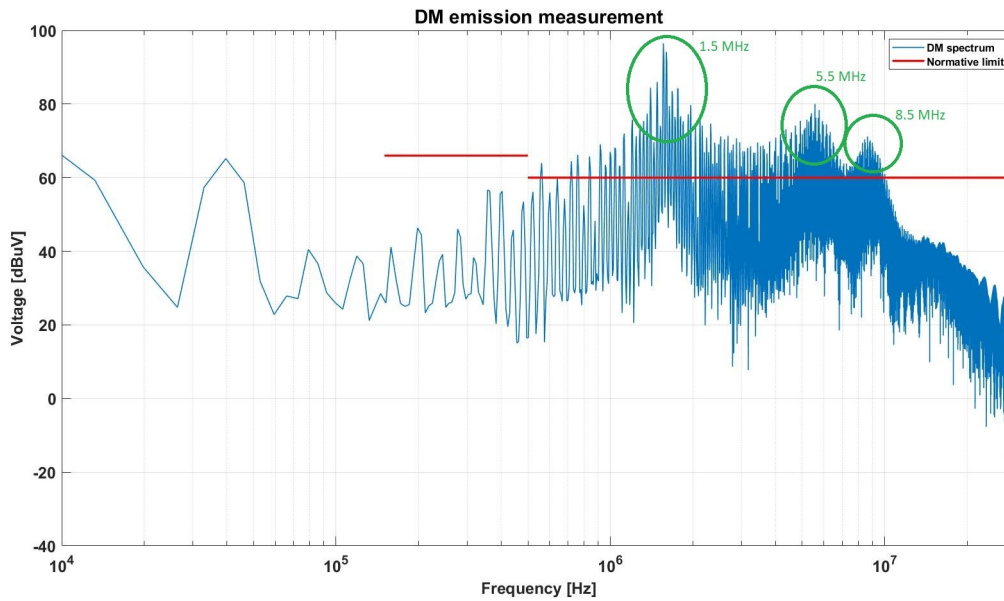


Figure 6.12: DM emission and its peaks.

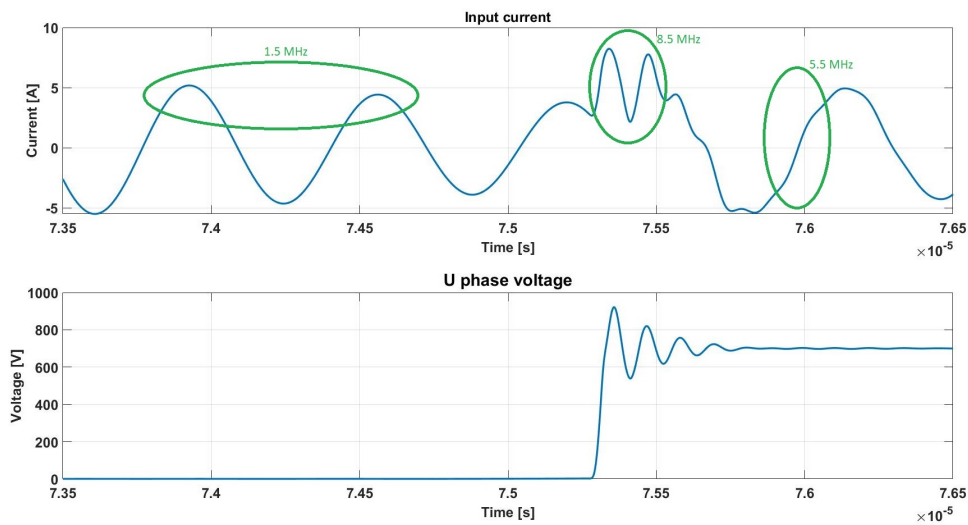


Figure 6.13: Behavior of "U" phase voltage and input current.

phase voltage. As seen before, this behavior is due to the resonance between the parasitics inductances and capacitances of the real MOSFET and of the cables introduced on the model. Finally, before starting the sinusoidal behavior with 1.5 MHz frequency, the waveforms exhibit a short further oscillation around their

nominal shape with 5.5 MHz frequency.

6.5 Model of the ditcher system

Until now, the model of the tedder system has been realized looking at its nominal and parasitic characteristics, at its measurement setup and its EMC behavior in different cases. On this section, the model has been replicated for the ditcher system starting from the measurement setup described on Figure 6.7 and changing the parameters appropriately.

For first, the motor data has been changed on the script reported in Appendix C by considering the parameters already shown in Table 3.4. Also the control data has been changed by setting the correct nominal speed and current. The DC cables are exactly the same of the tedder system, while the three-phase ones are changed due to the difference seen before on Tables 5.2 and 5.4. This has been done by keeping unchanged the circuitual model but changing the geometrical data.

Since in this case the switching devices are the SiC power modules shown in Figure 3.8, they have been opportunely changed on the inverter model as shown in Figure 6.14. There are several difference on the ditcher inverter compared to

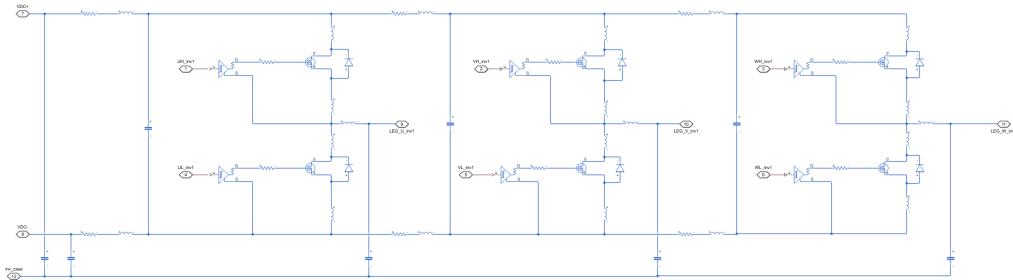


Figure 6.14: Model of the ditcher inverter.

the tedder one. The PCB traces are quite shorter and the equivalent resistances and the inductances have been reduced to $200\ \Omega$ and $3\ \text{nH}$. Also the geometry is difference, since the switching devices and the cooling plate, unlike the tedder system, are in parallel with the PCB. In this case, there is an increasing of the coupling capacitances with the inverter case from $60\ \text{pF}$ to $200\ \text{pF}$. The power module inductances are estimated by looking at their datasheet, which provide a stray inductance equal to $L_{sCE} = 8\ \text{nH}$ [15]. This value depends on the topology

and it is the inductance of a single switch for two switches power, as shown in Figure 6.15 [32]. The stray inductance has been equally splitted as 4 nH for each drain and source. In addition to this, this inductance has been summed with

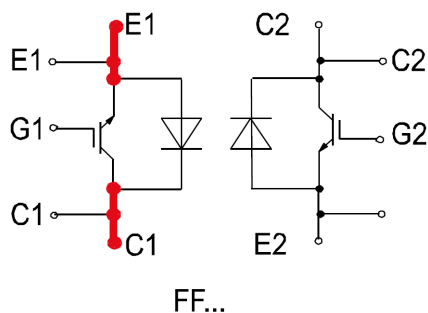


Figure 6.15: Stray inductance of the SiC power module.

the equivalent one of the device pins, estimated with a 1 nH/mm approximation, obtaining 3,2 nH. This inductances have been placed on drain of topper switch, on source of the bottom one, and on the phase output. Finally, the 6.14 shows that the diode has been not implemented anymore on the MOSFET model, because the information provided by the datasheet are related to the parameters defined only on the *Diode* block.

Finally, the complete model has been simulated getting the results shown in Figure 6.16 and 6.17, respectively for the measurement of DM and CM emissions and for the LISN overall measurement. As expected, the LISN spectrum is almost totally equal to the CM one since it is much greater than the DM contribution. Also, the shape of the two spectra is similar to the tedder system in "single configuration", but with higher values because of the higher power involved.

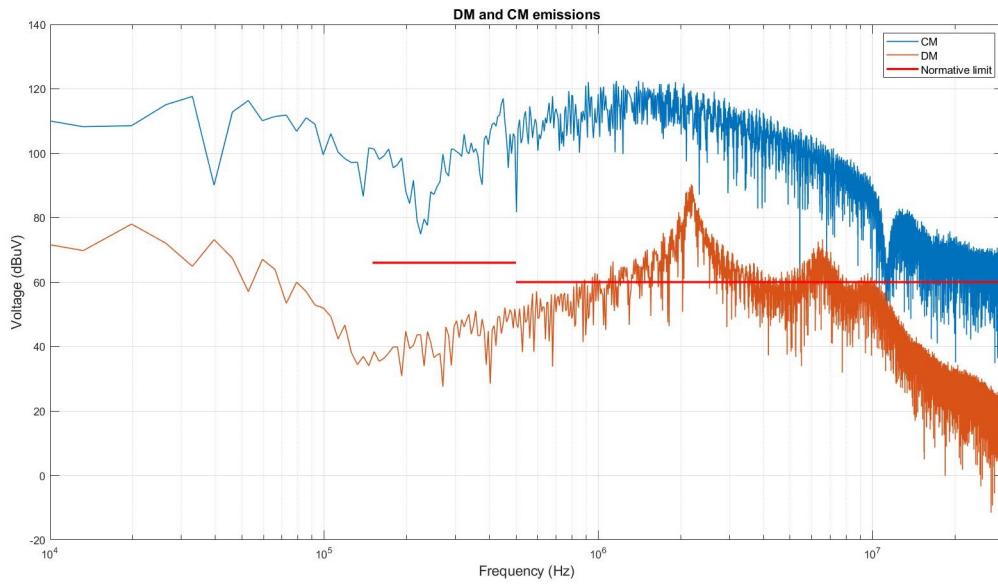


Figure 6.16: DM and CM emissions measured on ditcher system.

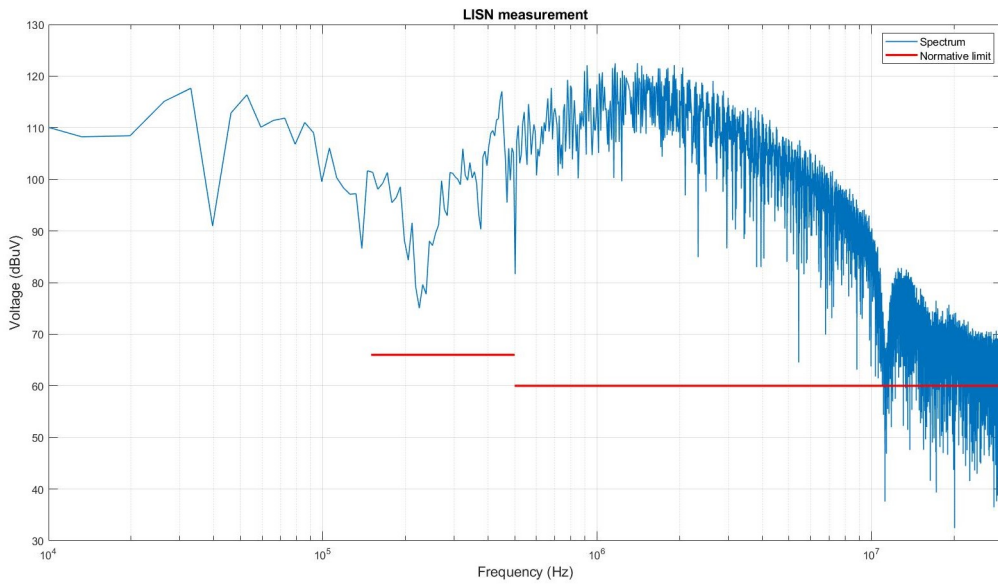


Figure 6.17: LISN measurement on ditcher system.

Chapter 7

Design of EMI filters

Once the modeling of the inverters has been performed, as previously detailed, in this Chapter the specifications of the EMI filters will be first defined and, then, they will be designed accordingly. As done in the previous sections, the analysis is focused on the tedder system and the results will be applied also on the ditcher one.

The LISN specified by the standard can only measure the total conducted emissions, but the filter must provide attenuation for both the CM and the DM noise currents. Figure 7.1 shows the DM and CM emission spectra increased by 6 dB as a safety margin to take into account any neglected emission contribution. The Insertion Loss (IL) of the filter is defined as the ratio (or the difference in dB) between the spectrum seen at the measurement port without the filter inserted and the one with the filter inserted. The required ILs, reported on Equation 7.1, are computed both for amplitude and frequency looking at the DM and CM peaks.

$$\begin{cases} IL_{DM} = 42 \text{ dBuV @ } 1.5 \text{ MHz} \\ IL_{CM} = 70 \text{ dBuV @ } 870 \text{ kHz} \end{cases} \quad (7.1)$$

The requirements for the CM attenuation are more stringent for both magnitude and frequency and, for this reason, the design will start from the CM filter.

7.1 Topology

The design starts with the definition of a general topology for the EMI filter without including, at the moment, any parasitic contribution. A filter can be seen as a mismatching device. In power transmission theory, the criteria for maximum power transfer is that the source and the load resistances must be equal or complex conjugates. On the contrary, the EMI transfer is minimized with maximally mismatched source and load impedances. The filter attenuation is a function of

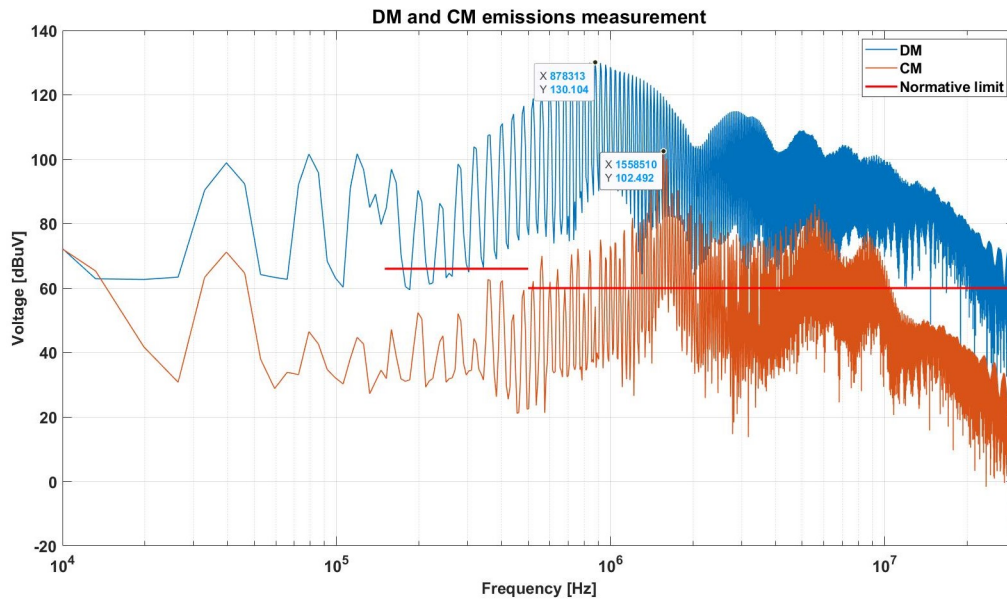


Figure 7.1: Insertion loss required for DM and CM emissions.

impedance mismatch between the SMPS and LISN, influencing the topology chosen for the filter [33]. In addition to this, if only purely reactive elements are used in the filter, the EMI energy is reflected back to the emission source, while if lossy elements are used the EMI energy may be dissipated as heat [33]. Since a low-pass attenuation is needed, a power line filter is based on an LC topology. In particular, as shown in Figure 7.2, the simplest topology of a filter is composed of a Common-Mode Choke (CMC) and two Y-capacitors for the CM emission, and by two differential-mode inductances an X-capacitor for the DM component.

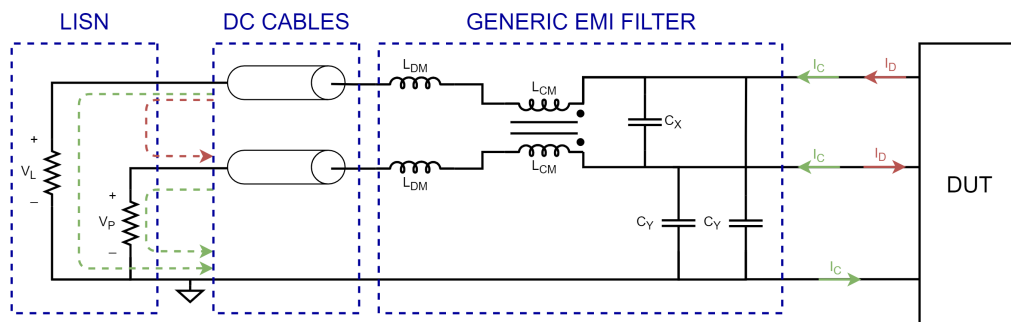


Figure 7.2: Generic typical EMI filter topology.

7.1.1 Review of basic magnetics

To understand how a CMC is realized, first consider the structure of a simple inductor. It is composed by a winding of n turns placed on a core having permeability μ , as shown in Figure 7.3. Faraday's law states that the flux $\Phi(t)$ inside the core

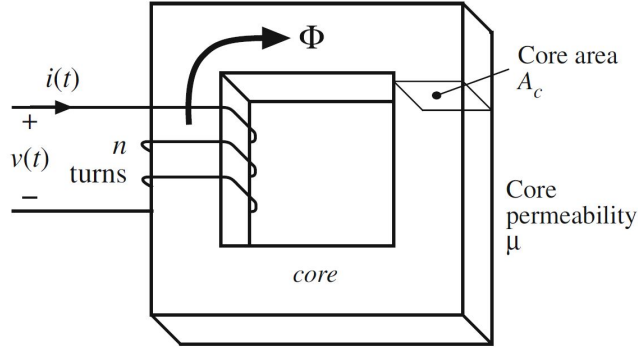


Figure 7.3: Inductor geometry [34].

induces a voltage $v_{turn}(t)$ in each turn of the winding, given by:

$$v_{turn}(t) = \frac{d\Phi(t)}{dt} \quad (7.2)$$

Since the same flux $\Phi(t)$ passes through each turn of the winding, the total winding voltage is:

$$v(t) = n \frac{d\Phi(t)}{dt} \quad (7.3)$$

By relating the flux $\Phi(t)$ with the coil current $i(t)$ through the definition of magnetic field strength $H(t)$ [34], the total winding voltage can be also written as:

$$v(t) = \frac{\mu n^2 A_c}{\ell_m} \frac{di(t)}{dt} \quad (7.4)$$

where A_c and ℓ_m are, respectively, the core area and the magnetic path length around the interior of the core. As a consequence, the inductance value is given by:

$$L = \frac{\mu n^2 A_c}{\ell_m} \quad (7.5)$$

The relationship between the average flux density B and the magnetic field strength H is determined by the core material characteristics:

$$B = \mu H \quad (7.6)$$

The real characteristic is nonlinear and exhibits both hysteresis and saturation phenomena. In particular, the core material saturates when the magnitude of the flux density B exceeds the saturation flux density B_{sat} . The device behaves as an inductor for $|I| < I_{sat}$. If not, the flux density $B(t) = B_{sat}$ is constant and the winding voltage is zero, resulting in short circuit behavior. Square-loop materials exhibit an abrupt saturation characteristic and have a very large relative permeability, while soft materials exhibit a less abrupt saturation characteristic. In general, the core saturation is heavily dependent on the core material and shape. Sometimes, an air gap is added to the core allowing it to operate at higher values of winding current $i(t)$ without saturation [34].

7.1.2 Common-mode choke

A common mode inductor is fabricated by winding two wires around a ferromagnetic core as shown in Figure 7.4(a). The voltage across each winding is given by Equation 7.3. If the windings are identical between them and the total flux completely links both windings, then the winding inductances are equal to $L_1 = L_2 = L$. The impedance of one winding is given by:

$$\hat{Z}_1 = \frac{\hat{V}_1}{\hat{I}_1} = \frac{pL\hat{I}_1 + pM\hat{I}_2}{\hat{I}_1} \quad (7.7)$$

The series impedance varies due to the current component considered. Looking at the CM currents $\hat{I}_1 = \hat{I}_C$ and $\hat{I}_2 = \hat{I}_C$, providing:

$$\hat{Z}_{CM} = p(L + M) \quad (7.8)$$

The series impedance due to DM currents, where $\hat{I}_1 = \hat{I}_D$ and $\hat{I}_2 = -\hat{I}_D$, is:

$$\hat{Z}_{DM} = p(L - M) \quad (7.9)$$

If the windings are perfectly symmetric and all the flux remains in the core, then $L = M$ and $Z_{DM} = 0$. Ideally, a CMC has no effect on DM currents, while it places an inductance equal to $2L$ in series with the two conductors to CM currents, as shown in Figure 7.4(b) and 7.4(c).

In real applications, the flux produced by one winding does not couple completely to the other winding, due to the magnetizing inductance and current on the primary winding [34]. Hence, when DM currents flow in the windings there is a leakage flux that is not canceled. This leakage causes the winding to have a small DM inductance, the so-called leakage inductance, as shown in Figure 7.5. The leakage inductance of the CMC determines the differential-mode inductance available "for free" in the filter. As always, this effect provides both advantages and disadvantages. Each winding of the choke has a small DM inductance which forms an L-C filter

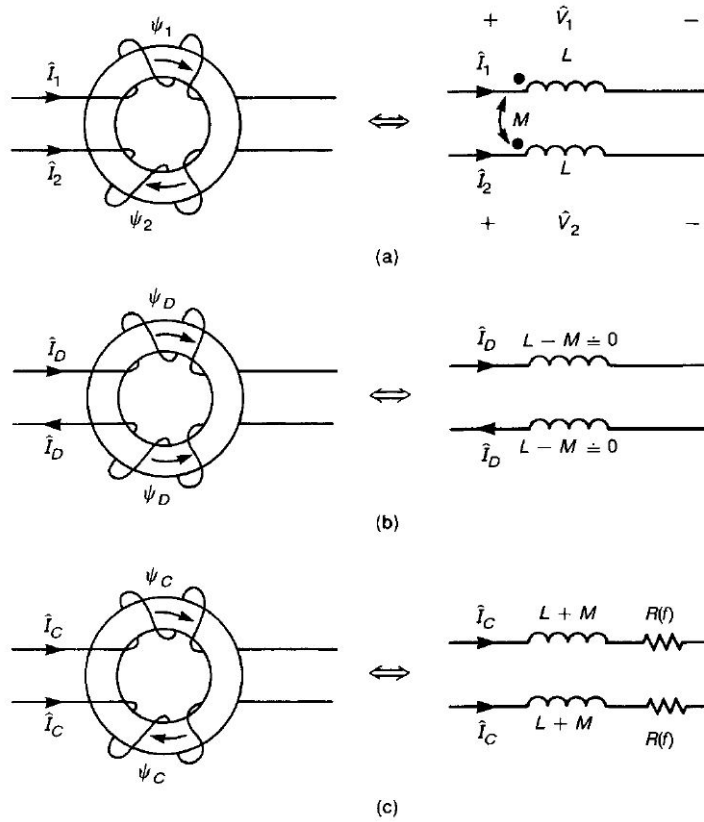


Figure 7.4: Modeling the effect of a CMC on (a) the currents of a two-wire line, (b) the DM components, and (c) the CM components[3].

along with the X-capacitor (see capacitors C_x in Figure 7.2), providing DM filtering. On the other side, too much leakage inductance can cause the saturation of the core at a low value of AC power current [30]. For this reason, the CM filter is usually designed first and then the DM filter is designed by starting from the leakage inductance of the CMC and choosing a value for the X capacitor to provide the required attenuation. If additional DM attenuation is required, two additional discrete inductors can be added to the DM filter. These leakage inductances cause the terminal voltage ratio $v_2(t)/v_1(t)$ to differ from the ideal turns ratio n_2/n_1 . The coupling coefficient k is a measure of the degree of magnetic coupling between the primary and secondary windings. It lies in the range $0 \leq k \leq 1$ and it is defined as:

$$k = \frac{M}{\sqrt{L_1 L_2}} \quad (7.10)$$

In a CMC with perfect coupling, the leakage inductances are zero and the coupling coefficient is then equal to 1.

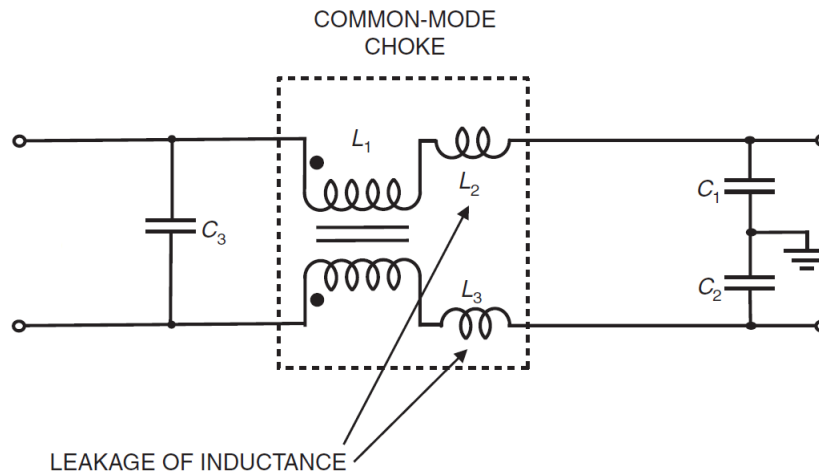


Figure 7.5: Power-line filter showing the leakage inductance of the common-mode choke [30].

Typically, a common-mode choke is realized on a toroidal core. One of the advantages of the toroidal shape is that, due to its symmetry, the amount of leakage flux is lower than other core configurations [35]. The most common material used for low-cost applications is high permeability manganese zinc ferrite. In high-end applications, instead, Co-based amorphous, Fe-based amorphous, and Fe-based nanocrystalline materials are used. In general, the nanocrystalline core has the following advantages [36]:

- The typical impedance is over twice that of the ferrite core, with the same core size, wire size, and number of turns;
- Very high permeability, allowing to reduce the component size;
- Saturation flux of 1.25 T, over twice the one of ferrites which is less than 0.5 T;
- Curie temperature (the temperature above which the material loses its permanent magnetic properties) of 200°, as compared to 330° for ferrites, allowing to be used in much higher temperature applications.

However, the major disadvantages of using nanocrystalline cores are the high cost and the long lead time in many cases.

7.1.3 X and Y capacitors

Class-X and class-Y capacitors are safety certified and designed to be used in power-line filtering for many electronic device applications. Because of the direct

connection to the supply voltage, these capacitors may be subjected to overvoltages and spikes, causing failures. When a class-X capacitor fails because of an overvoltage, it is likely to fail short and this would cause an overcurrent protective device to open. If a class-Y capacitor fails, instead, this could lead to a fatal electric shock due to the ground connection. For this reason, class-Y safety capacitors are designed to fail open [37].

Safety capacitors are classified into subclasses according to their peak or rated voltage and the peak impulse voltage that they can safely withstand. However, this classification is strictly related to the applications on AC power lines. For the DC supplies, like the one used for this thesis work, the limitations are different. In particular, the ISO6469-3 normative imposes different safety standards in the case of capacitors used in AC or DC power lines [38].

- For AC body currents caused by such capacitive couplings when touching AC class B voltage ($30 \text{ VAC} \leq V \leq 1000 \text{ VAC}$), the AC body current shall not exceed 5 mA when measured following IEC 60950-1.
- For DC body currents caused by the discharge of such capacitive couplings when touching DC class B voltage ($60 \text{ VDC} \leq V \leq 1500 \text{ VDC}$), the energy of the total capacitance between any energized voltage class B and the electric chassis shall be $E_{imm} \leq 0,2 \text{ J}$ at its maximum working voltage. The total capacitance should be calculated based on the designed values of related parts and components.

Following the second statement, the maximum value can be calculated supposing a large overvoltage equal to $\Delta V = 1 \text{ kV}$. In this case:

$$E_{imm} = \frac{1}{2} C (\Delta V^2) \leq 0.2 \text{ J} \implies C \leq 400 \text{ nF} \quad (7.11)$$

Regarding the X-capacitor, instead, there is no design constrain on DC line applications and it can be chosen looking at its safety features and voltage rating.

7.2 Stability

It is possible to realize a first design of the EMI filter from the IL specifications. Since the DM inductance depends on the leakage inductance of the CMC, the CM filter is firstly designed. Some hypotheses could be formulated on the behavior of the components and their value is not normalized at all. Since $IL_{CM} = 70 \text{ dB}$ at 870 kHz is needed, considering that the filter shown in Figure 7.2 is a 2nd order filter, its attenuation increases with a -40 dB/dec after the corner frequency, which has to be chosen at least at $f_{CM} = 10 \text{ kHz}$. Supposing to use $C_y = 100 \text{ nF}$, the CM

inductor is given by:

$$L_{CM} = \left(\frac{1}{2\pi f_{CM}} \right)^2 \cdot \frac{1}{2C_y} = 1.3\text{mH} \quad (7.12)$$

Supposing that the common-mode choke is characterized by a coupling coefficient of $k = 0.95$:

$$L_{DM} = L_{leak} = 0.05 \cdot L_{CM} = 65 \mu\text{H} \quad (7.13)$$

Since the DM filter needs $IL_{DM} = 42 \text{ dB}$ at 1.5 MHz, a corner frequency of $f_{DM} = 10 \text{ kHz}$ has been considered, providing:

$$C_x = \frac{1}{2\pi f_{DM} 2L_{DM}} = 2\mu\text{F} \quad (7.14)$$

These values are needed to make a first simulation of the filter. The input filter is described by its voltage transfer function $H(f)$ and its finite output impedance $Z_{out,filter}(f)$. On the other side, the filter sees the input impedance of the SMPS $Z_{in,SMPS}$. However, the fact that the filter shows a non-zero output impedance and the converter a non-infinite input impedance can degrade the performance of the device or even lead to instability. For guaranteed system stability, the output impedance of the input filter must be much smaller than the input impedance of the closed-loop converter [39]:

$$Z_{out,filter} \ll Z_{in,SMPS} \quad (7.15)$$

This condition is due to the control loop action, which keeps the inverter output waveform constant even if variations of the input voltage occurs. This behavior can be described as a negative resistance at the converter input side, which forms a parallel resonance tank with the LC input filter and it is a potential source of oscillation.

In this thesis work, the control loop acts until 400 Hz, which means that the stability problem should be confined to low frequencies. Nevertheless, on a typical filter design, stability is ensured for a wide band using the damping technique. By adding a resistive loss element to the filter circuit, the LC resonance can be damped and the $Z_{out,filter}$ peak is reduced at resonance, making easier separation with $Z_{in,SMPS}$ curve. Two ways to damp an LC input filter are shown in Figures 7.6 and 7.7. In this work, parallel damping has been used. In this case, it is demonstrated that the peaking is minimized by using [40]:

$$\begin{cases} R_D = \sqrt{\frac{L_{DM}}{C_{DM}}} \\ C_D = 4 \cdot C_{DM} \end{cases} \quad (7.16)$$

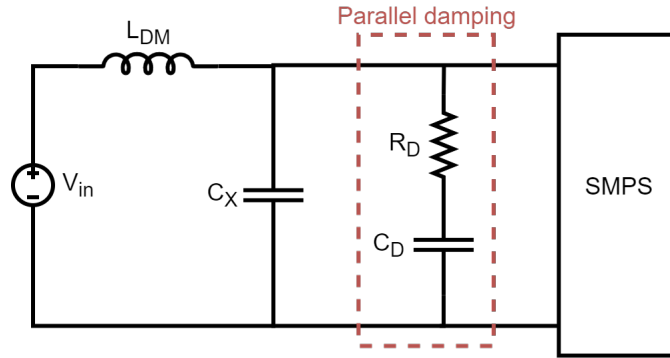


Figure 7.6: Parallel damped filter

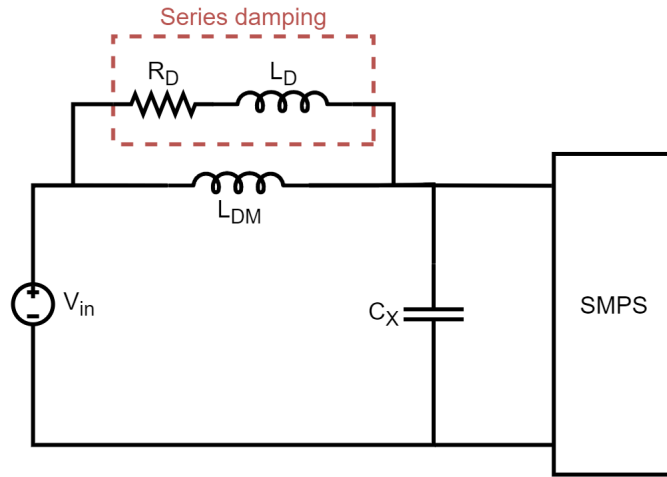


Figure 7.7: Series damped filter

The effectiveness of this technique can be seen by performing a Spice simulation of the filter with and without the damping, as shown in Figure 7.8, where the simulation setup allows to compute the filter output impedance. The output impedances, in the two cases, have been compared to the input impedance of the inverter. This last one has been estimated by using the data definition code in Appendix C:

$$|Z_{in,SMPS}| = \frac{V_{DC}^2}{4P_{DC}} = 12.7 \Omega \quad (7.17)$$

Since the real $Z_{in,SMPS}$ is not flat, the computed value has been reduced by 10 times to make a very safe comparison. As expected, the results in Figure 7.9 show the reduction of the peak on the resonance frequency by using parallel damping.

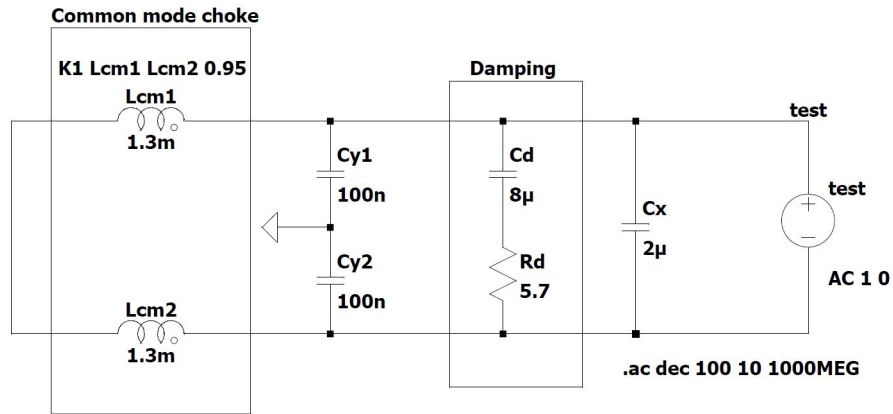


Figure 7.8: Simulation setup for the measurement of the filter output impedance.

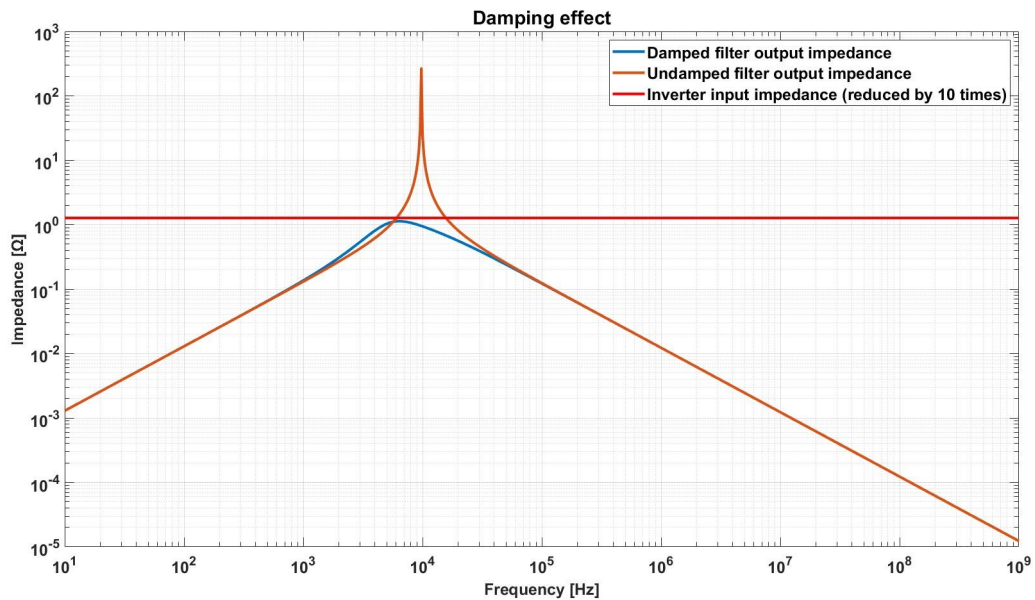


Figure 7.9: Effect of the parallel damping on the output impedance of an ideal filter.

7.3 Components selection

Once the filter components have been described, they have been selected looking at the solutions proposed by the main semiconductor and magnetics manufacturers for EMI suppression applications. In particular, the following specifications have been considered:

- The components cost and/or availability on the market.
- The component sizes. As a volume for the filter there was a maximum height of 75 mm and width of 150 mm because of mechanical constraints. It was not specified a maximum filter length, allowing to design of a multi-stage filter if necessary.
- Voltage rating and effectiveness for X and Y capacitors.
- Current rating and effectiveness for CMC. The choke must be chosen with a current rating of around:

$$I_{DC} = \frac{P_{DC}}{V_{DC}} = 57 \text{ A} \quad (7.18)$$

Common-mode choke

A topic point on this analysis regards the choice of a common-mode choke with characteristics adapted to the required application. In particular, the main issue was to find a trade-off between the current rating and the CM inductance of the device. The choke available with a current rating of around 57 A are not too much and, in most cases, they haven't the necessary characteristic. A recap of the solutions found is reported on Table 7.1. The Self-Resonant Frequency (SRF)

Part Number	Manufacturer	Core	L_{CM}	SRF	I_{rat} [A]	Availability
CM-161U-60A	CWS	Ferrite	160uH	825kHz	60	15 \$ on CWS site
C-36A29-06	CWS	Ferrite	70uH	Not reported	90	10 \$ on CWS site
C-36A29-07	CWS	Ferrite	110uH	Not reported	60	10 \$ on CWS site
LN-H-121U-83A	CWS	Nanocrystalline	121uH	1MHz	83	9 \$ on CWS site
RD8127-64-0M8	Schaffner	Not reported	800uH	> 3MHz	64	43 € on RS
B82726S3543N040	EPCOS / TDK	Ferrite	190uH	[500kHz, 1MHz]	54	10 € on Mouser
SCF47B-600-2R2C0005JH	Kemet	Nanocrystalline	50uH	> 10MHz	60	13 € on Mouser
RB6122-50-0M3	Schaffner	Not reported	250uH	500kHz	50	13 € on Mouser

Table 7.1: Solutions proposed for the selection of the common-mode choke.

is the frequency at which the parasitic capacitance of the CMC resonates with its inductance, resulting in an extremely high impedance. As a consequence, the device attenuation is maximum at SRF but it does not work properly beyond it. The SRFs shown in the table were taken from the device's datasheet, when possible, or estimated by looking at the impedance vs frequency graphs.

An interest solution is proposed by the Schaffner and regards the possibility to apply a forced cooling on the choke in order to increase its current rating [41]. Although this solution is applicable and allows to increase the inductance value and the IL of the filter, it has not been further exploited due to the difficult mechanical integration. In this work, instead, it was chosen to design the filter



Figure 7.10: 3D view of the CM-161U-60A common-mode choke.

using a CM-161U-60A of the CWS, which is one of the best solutions for this application. The CM-161U-60A 3D view is shown in Figure 7.10. It has a height of around 40 mm and width of around 46 mm, suited with the filter available space. Nevertheless, the value of the CM inductance is much less than the one predicted in the previous section, which will lead to an increase in the filter order to get the required IL. If it is desired to use another choke available on the market, this is possible by carrying out the procedure that will be shown from now on.

X and Y capacitors

As seen before, safety capacitors are needed for both X and Y classes. Semiconductor manufacturers propose several solutions based on their ratings and applications. For the X-capacitors, the best solution has been identified on the "B32912*5...B32918*5" series of the TDK. There are film capacitors of the X1 subclass, optimized for the "across the line" application [42] and the available values vary from 6.8 nF to 5.6 μ F. Belonging to the X1 subclass, they are rated for a voltage of 1 kV. Since the ideal LC filter was designed with $C_x = 2 \mu$ F, this series seem to be suitable with the specifications.

The Y capacitors can be selected from Y1 or Y2 subclasses, since both provide capacitors with a voltage rating sufficiently high. In particular, the best Y1 capacitors series available are:

- Vishay VY1 series: some of them are already present in stock, but the values go up to 4.7 nF.
- Vishay SMDVY1 series: the capacitor values are equal to the ones of the previous series but the technology is SMD.

- Vishay 400L series: it allows to use Y1 capacitors with values up to 20 nF. Nevertheless, this maximum value is unobtainable on online dealers, while the higher value easily available is 10 nF.
- Kemet KJN series: as for the VY1 series, the maximum value is 4.7 nF.
- Murata DK1 series: the capacitor values even go up to 1.5 nF.

Since the Y1 capacitors available are not suitable with the filter specifications, the Y2 subclass has been analyzed. Being rated for lower AC voltages, their values are generally higher than the ones of the Y1 subclass. In particular:

- Vishay MKP338 6 Y2 series: the capacitance values go up to 470 nF, but the Spice models are not available online.
- Kemet R41T series: provides capacitors up to 68 nF.
- TDK "B32021...B32026" series: provides capacitance optimized for EMI suppression until 1 μ F and the Spice models are available.

This last series has been chosen for reasons of cost, availability and modeling. In addition, the footprint of these TDK capacitors is available and it should be used for the PCB design.

7.4 Equivalent model of filter components

Parasitics of the passive components, such as ESL of the capacitors and the inter-winding capacitance of the coupled inductors, have a negative influence on the EMI filter performances [43]. In order to design an optimized filter, a detailed model including parasitic elements of the passive components need to be realized. On this section, the filter components have been studied in order to determine their frequency behavior and realize a reliable filter model. The equivalent circuit of a generic common-mode choke is shown in Figure 7.11. The L_{CM} and L_{leak} values are defined on the CM-161U-60A datasheet as 161 μ H and 2 μ H. The maximum value of the line impedance R_{dc} is 0.5 m Ω . The inter-winding capacitance C_{win} resonates with the common-mode inductance at $SRF = 825$ kHz. For this reason, it can be estimated as:

$$C_{win,theory} = \frac{1}{2 \cdot (2\pi \cdot SRF)^2 \cdot L^2} = 108.3\text{pF} \quad (7.19)$$

The measured inter-winding capacitance reported on the datasheet is quite different:

$$C_{win,meas} = 145\text{pF} \quad (7.20)$$

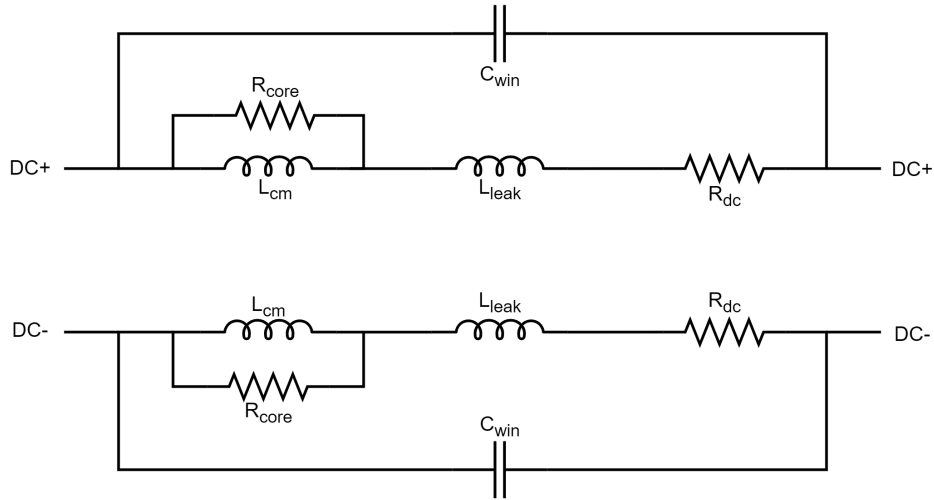


Figure 7.11: Equivalent circuit of a common mode choke.

Nevertheless, the difference is small and the datasheet value has been used. The core resistance R_{core} , which is ideally infinite, can be estimated by the impedance value at SRF reported on the datasheet, equal to:

$$|Z(@SRF)| = 400 \Omega \quad (7.21)$$

The impedance has been measured sweeping the R_{core} value and using the setup shown in Figure 7.12. It has been found that the impedance at SRF is around 400Ω by using $R_{core} = 800 \text{ k}\Omega$, as shown in Figure 7.13.

Once the CMC model has been completed, it has been included on the filter model. The SPICE models of the capacitors are available and they have been also included in the model. Since the common-mode inductance is quite small, the filter topology has been changed in order to obtain a better attenuation. The X and Y capacitors have been placed on both left and right side of the CMC, realizing a CLC filter. This choice, as well as for the attenuation, takes into account the presence of the DC cables which have an unpredictable impedance. As a consequence, the values of each X and Y capacitor have been halved respectively to $1 \mu\text{F}$ and 47 nF . The selected capacitors from the DTK series are:

- B32022A3473M: 47 nF Y2 capacitor;
- B32914A5105M: $1 \mu\text{F}$ X1 capacitor;
- B32916A5475M: $4.7 \mu\text{F}$ X1 capacitor for the damping;

The damping resistor has been experimentally fixed to 2.7Ω for minimizing the filter output impedance. Since the rating voltage of 700 V is quite high for commercial

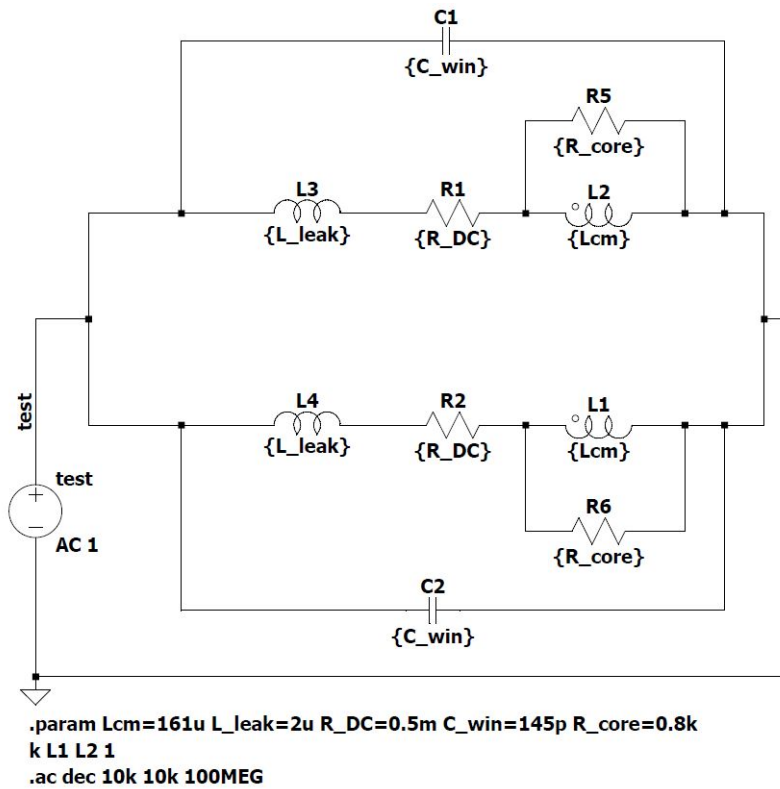


Figure 7.12: Setup for the measurement of the CMC impedance.

resistors, it has been chosen two "CRCW20101R50FNEF" of the Vishay in series. Each of them has a $1.5\ \Omega$ resistance and a 400 V rating. Figure 7.14 shows the filter model implemented on Spice.

To insert the real filter components on Simulink, it is necessary to model the capacitors by looking at their frequency behavior, which provides information about the ESR and ESL of the capacitor. The results of this analysis are shown in Table 7.2.

Part Number	Value	ESR	ESL
B32022A3473M	47 nF	90 m Ω	6.65 nH
B32914A5105M	1 μ F	45 m Ω	4.8 nH
B32916A5475M	4.7 μ F	10 m Ω	1.1 nH

Table 7.2: ESR and ESL of the X and Y capacitors.

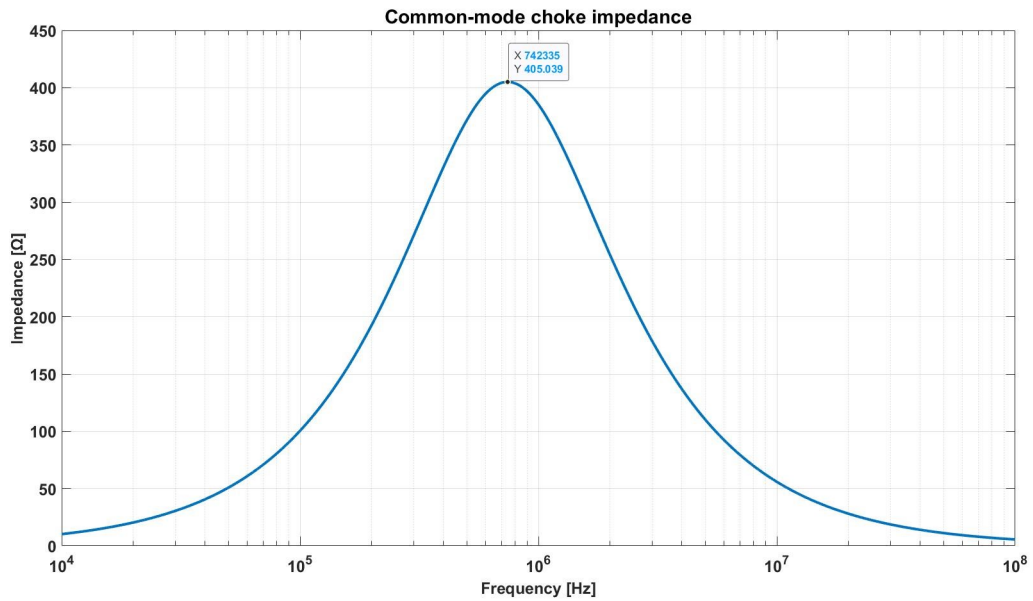


Figure 7.13: CM-161U-60A impedance measured with $R_{core} = 800 \text{ k}\Omega$

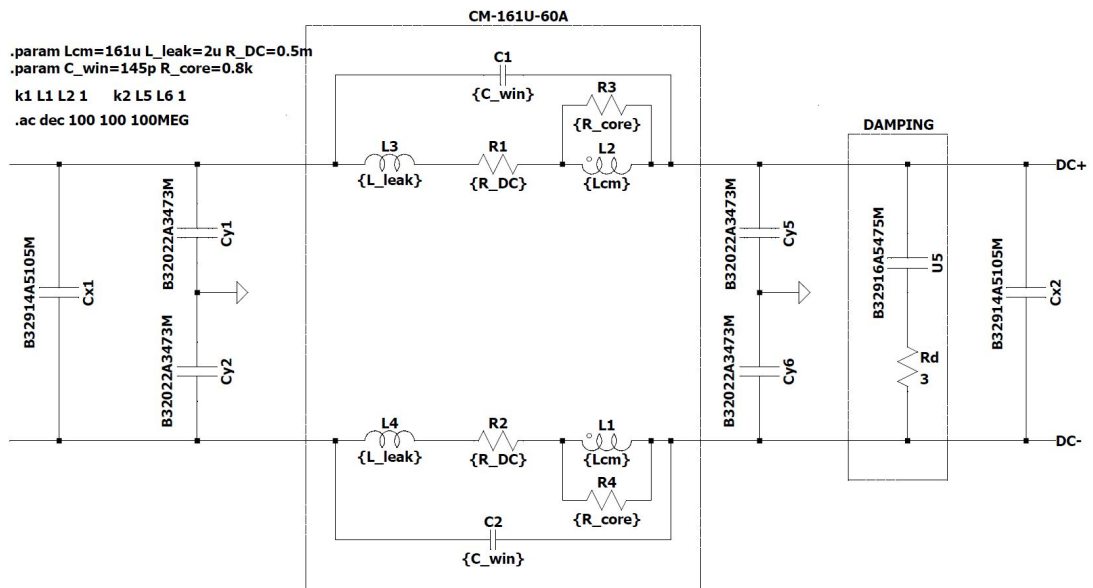


Figure 7.14: One stage EMI filter with input capacitors.

7.5 Model validation

The filter model has been inserted in the tedder system to evaluate its behavior. This validation procedure is necessary to see if the filter acts properly on the

reduction of the LISN measured spectrum and, if not, the filter must be re-designed in order to meet the regulation limits. The filter model has been realized by using the *Capacitor* blocks for the X, Y and damping capacitors. The CMC, instead, has been implemented by using the *Mutual inductor* block available on Simscape. It allows to define almost all the CMC parameters as shown in Figure 7.15. The only one which is missing is the inter-winding capacitance, which has been added externally. The filter has been added on the model between the 1 m DC cables and

The image shows a 'Settings' dialog box for a CMC model. It has two tabs: 'Main' and 'Resistance'. The 'Main' tab is active and contains the following parameters:

- Inductance L1: Lcm (text input), H (dropdown)
- Inductance L2: Lcm (text input), H (dropdown)
- Coefficient of coupling: coup_k (text input)
- Tolerance (%): 20 (text input)
- L1 tolerance application: None - use nominal value (dropdown)
- L2 tolerance application: Random tolerance (dropdown)
- L2 tolerance distribution: Uniform (dropdown)

The 'Resistance' tab is also visible and contains the following parameters:

- Series resistance, [R_primary R_secondary]: [Rdc_choke, Rdc_choke] (text input), Ohm (dropdown)
- Parallel conductance, [G_primary G_secondary]: [1/Rcore_choke, 1/Rcore_choke] (text input), 1/Ohm (dropdown)

Figure 7.15: Setting parameters for the CMC model.

the inverter input side. The spectrum at the LISN measurement port after the filter is inserted is shown in Figure 7.16. The filtered spectrum is higher than the normative limit until 1 MHz and at around 5 MHz. As a consequence, the values of filter components have been increased to see if the spectrum would get low enough, but with poor results. As a consequence, it was decided to increase the order of the filter by adding another LC stage for the CM filter. This is possible since the mechanical limitation is related to the height and width, not to the length. The filter has been modified obtaining the model shown in Figure 7.17. The filter on the model has been then modified inserting another CM stage. As Figure 7.18 shows, the further CM stage acts properly reducing the emission level below the normative limit. In particular, the filtering remains unchanged for frequencies higher than around 5 MHz, due to the CM resonance already present in all the previous simulations. Evidently, the CM impedance at those frequencies greatly limits the behavior of the filter. To ensure the effectiveness of the filter, the CM emission sources (such as the inductive connection with the reference) should be minimized, while until now they have been included to put the system in a worst case condition.

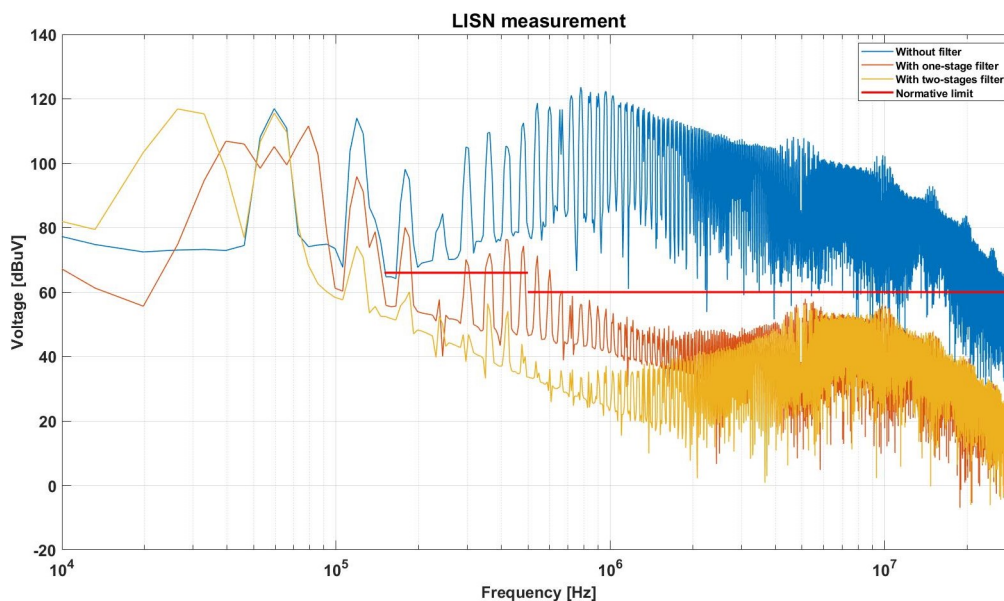


Figure 7.18: Comparison between the LISN measurement without filter and with a two stage filter.

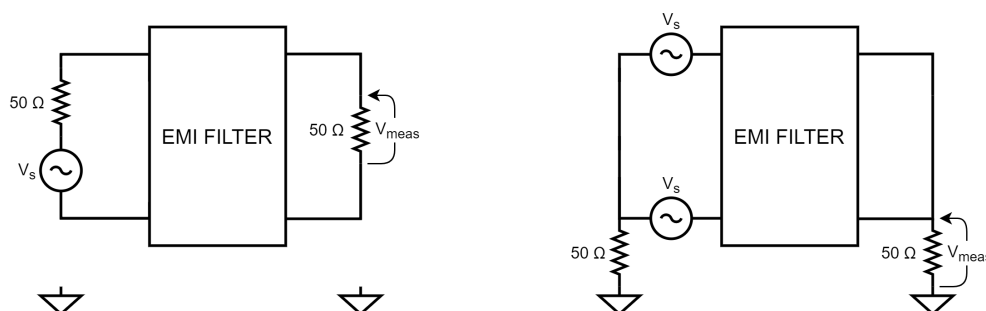


Figure 7.19: Setup for the EMI filter characterization in DM (left) and CM (right).

the capacitor on input side and even more inserting another stage. The results show that both DM and CM attenuation are much higher than the one required by the specifications. However, it is important to underline that the IL shown in this analysis is the result of a generic filter characterization and it is not equal to the one obtained inserting the filter on the final model. In fact, the attenuation is strictly related to the impedance seen on both input and output side of the filter, which can cause an higher or lower attenuation than the one measured on a $50\ \Omega/50\ \Omega$ system. This consideration is especially true for the CM attenuation,

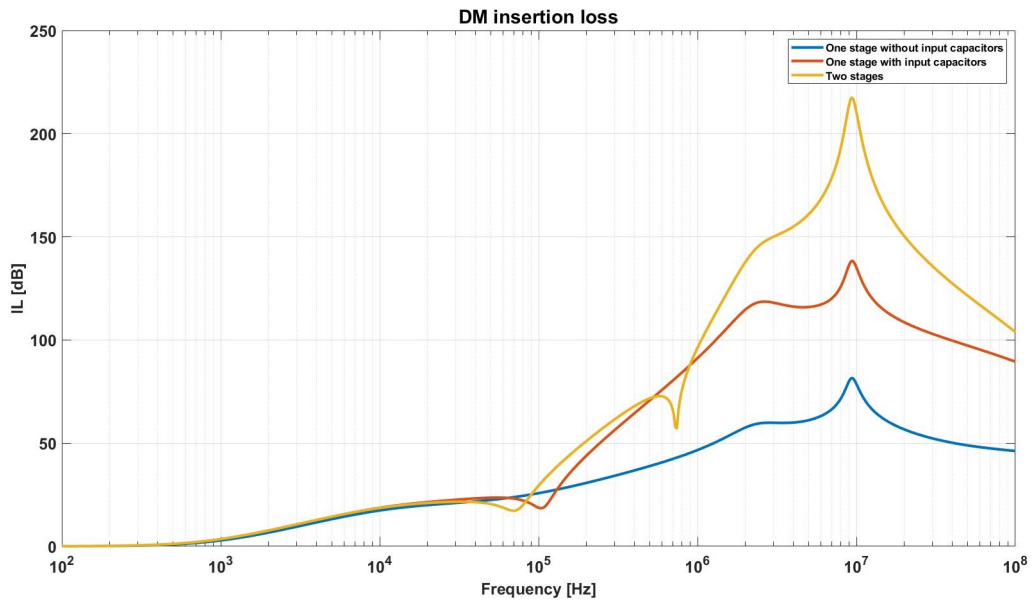


Figure 7.20: Comparison of the DM insertion losses measured on a generic 50 Ω/50 Ω system.

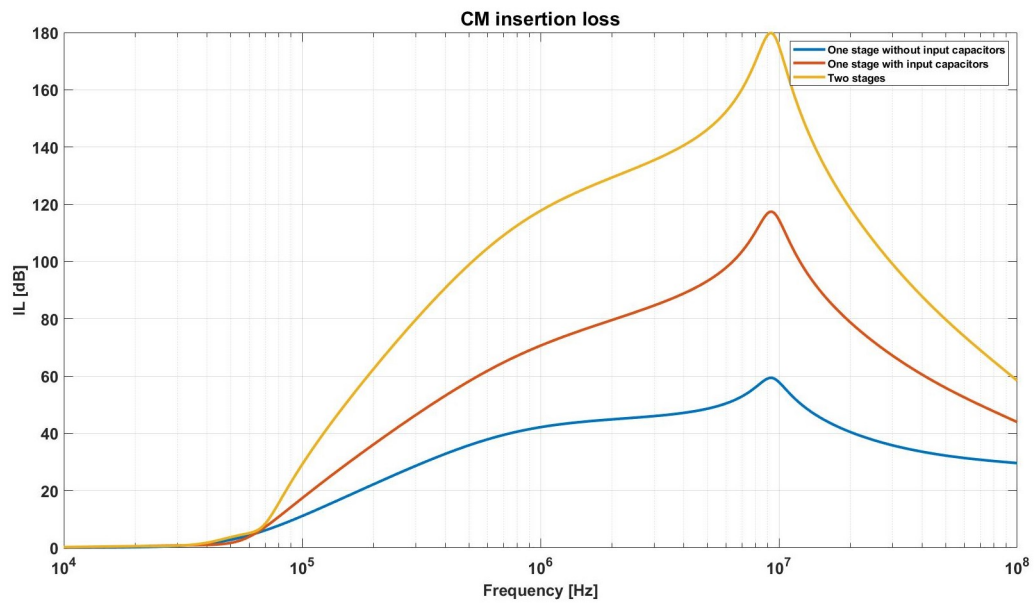


Figure 7.21: Comparison of the CM insertion losses measured on a generic 50 Ω/50 Ω system.

which depends not only from the nominal impedance of the system but also from the system measurement setup and therefore it is highly variable.

The filter stability was evaluated by looking at its output impedance with the measurement setup already shown in Figure 7.8. It has been found that to minimize the output impedance, due to the insertion of a second stage, it is necessary to increase the damping resistance to around $12\ \Omega$.

Finally, the two-stage filter has been validated also on the ditcher system. Since the emission spectra and the measurement setup were very similar to the ones of the tedder system, the filter design is valid also in this case as shown in Figure 7.22.

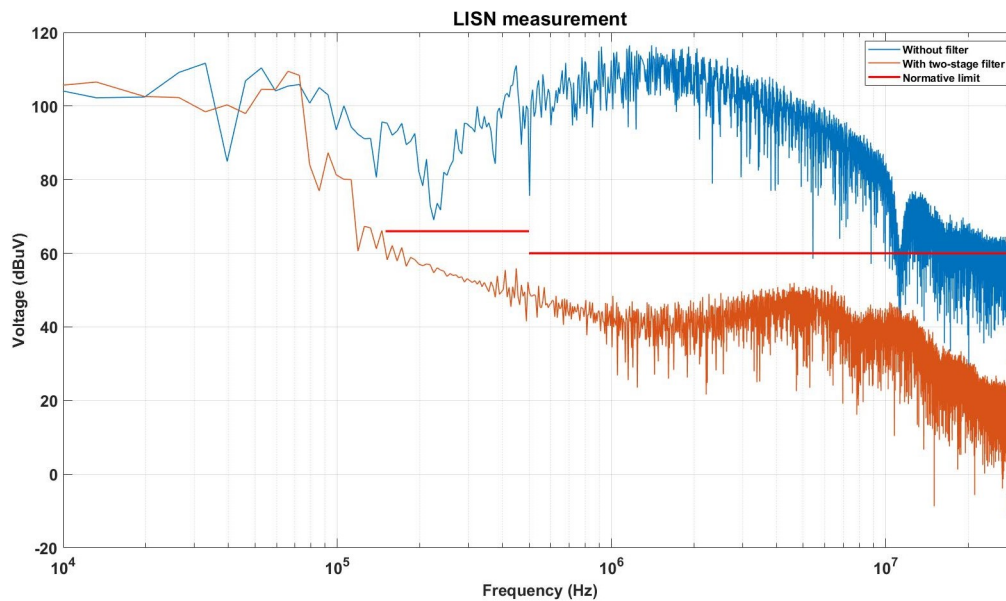


Figure 7.22: LISN measurements without and with two-stage filter on ditcher system.

7.6 Some considerations on how mounting the EMI filter

The performance of the filter is as much a function of how and where it is mounted as of its electrical design. In this sections, the most common mounting issues are illustrated, since they can significantly decrease the filter effectiveness [30]. First, a metal case must be used to properly enclose the filter, avoiding any radiated coupling with the external environment. Second, the filter should be mounted

close to the emission source to acts properly, otherwise the filter cannot remove any noise picked up by the power lines after it. Third, capacitive coupling occurs between the power lines before and after the filter. A good rule is to not route the filter input cables close to output ones, otherwise this will maximize the parasitic capacitance coupling. Finally, the grounding of the filter should be placed on the metal enclosure. This connection can be a large inductance and can decrease the effectiveness of the Y-capacitors. The filter manufacturers, typically, mount the internal Y-capacitors in order to minimize this inductance connection. Figure 7.23 show the two situations in which the filter is improperly or properly mounted. A properly mounted power-line filter overcomes the three problems.

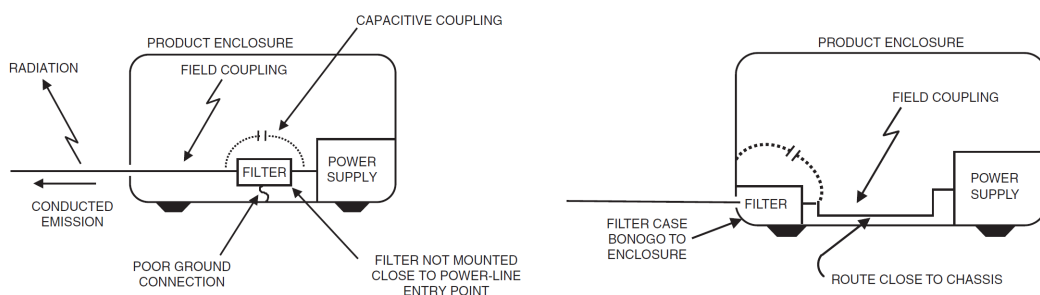


Figure 7.23: EMI filter mounting and grounding improperly (left) and properly (right) [30].

As a further demonstration, it was placed an inductance to simulate the grounding connection of the Y capacitor. The inductance value has been set to 10 nH to see its effect on the LISN measurement emission. The result of the comparison is shown in Figure 7.24. As expected, the improper grounding if the Y capacitors change the LISN measurement, especially at high frequencies where the resonance almost reaches the limit of the regulation. This result suggest that a proper grounding is mandatory to ensure the effectiveness of the filter. In particular, an inductive connection higher than 10 nH should be avoided.

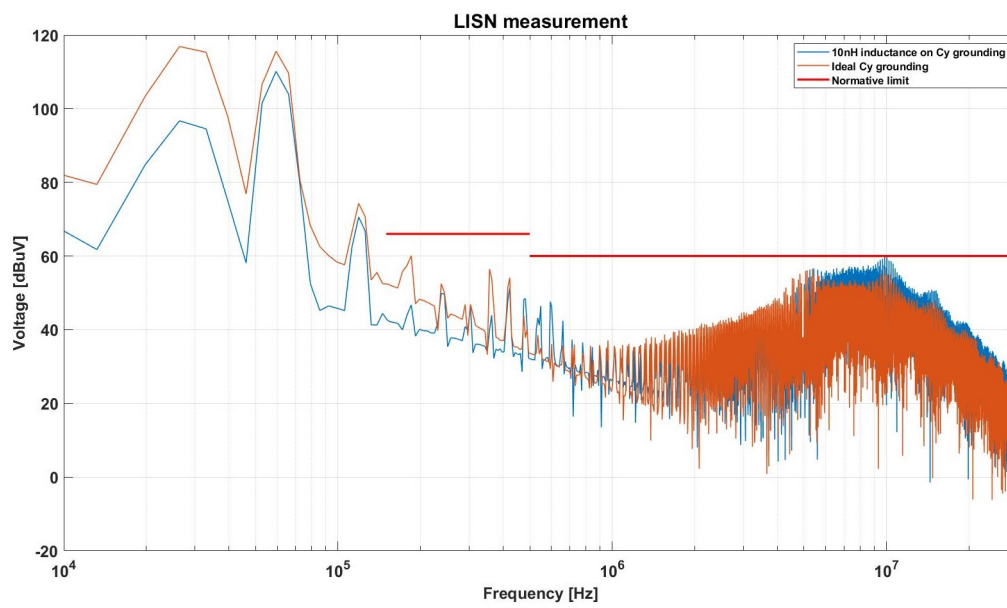


Figure 7.24: Effect of the improper grounding of the Y capacitors.

Chapter 8

Conclusions and outlooks

The present work has provided the design of the EMI filters for the so-called tedder and ditcher systems. The design has been preceded by the realization of the Simulink models of the two systems, focusing on the main sources of conducted emission. This analysis, in addition to the components and the topology of the filter, has provided some design considerations regarding the influence of various inverter parameters in terms of EMC.

The model has been realized on the Simulink environment using the *Simscape Electrical* tool, which is suited for modeling electronic, mechatronic, and power supply systems. The modeling has been divided into various steps, refining the model more and more and including new emission sources up to the final measurement setup. The system analysis has been focused on the tedder system, while the ditcher one has been realized reusing the results achieved.

A basic model has been implemented including the stator, the SVPWM algorithm, the inverter with ideal switches, and implementing the LISN for the emission measurement. This section allowed also to define the steady-state equations, fixing the system operating point and looking at its time-domain behavior. The SA and solver configurations have been set following the normative and looking at their impact on the system behavior and the LISN measurement.

Later on, an advanced model has been implemented optimizing the simulator efficiency and the precision of the results. It was seen that using a MOSFET model with real dv/dt waveforms is important to obtain reliable results, confirming the importance of the voltage and current derivative on the overall emission. The operating point parameters have been swept to put the system in the worst-case condition, though their effect was quite negligible. On the other side, the main emission sources have been identified on the resonance due to the non-idealities present in the model. These results came from the model of the PCB inductive path and, mostly, on the DC and three-phase side cables. They are the main source of conducted emission, especially due to the CM path created with the grounding

of the cable shields. Nevertheless, an analysis has been conducted for minimizing this inductive connection and then the CM currents.

The tedder model has been terminated by including all the four "legs" of the complete system. It was found that the symmetric shifting strategy, proposed during this work, is very useful to reduce the conducted emission spectrum. The measurement setup has been completed including the metal enclosures of the devices and the insulator support imposed by the normative. They introduce further capacitive and inductive couplings, influencing the spectrum on the LISN measurement port. The same model setup has been realized also for the ditcher system, obtaining results similar to the tedder system ones due to the affinity on construction and amount of power involved.

Finally, the model has provided the DM and CM insertion losses necessary for the EMI filter design. The design has been performed with commercial components, chosen based on their availability, size, effectiveness, and security specifications. The filter has been designed with a damping stage to ensure the system stability. The topology has been changed several times during the validation, until a spectrum that respects the limits of the legislation has been obtained.

Future developments

The final section of this thesis indicates some rules for the correct mounting of the filter and, if not, on the resulting consequences. One of the future developments of this work should consist of an analysis of the filter performance when the mounting or grounding varies within the measurement setup performed. In general, the work should be completed with experimental validation of the model and of the EMI filter, when it will be mounted. An important point regards also the condition in which the filter has been realized, which has been fixed to the worst case. As a consequence, the filter has required a two-stage topology, which is quite complex and expensive. Nevertheless, during this thesis work, some useful technique has been shown allowing to reduce the conducted emission by changing slightly the system topology, such as changing the grounding of the shields of the cables or applying an optimized modulation technique. Using the proposed techniques and carrying out an in-depth analysis on other techniques, is a good solution to get lower emission levels and, consequently, to reduce the order and complexity of the EMI filter required.

Appendix A

Tedder data definition

```
1 clc
2 clear all
3
4 %% Simulation data:
5
6 fmax=30e6; % [Hz]
7 fmin=150e3; % [Hz]
8
9 fsw=15e3; % [Hz]
10 dead_time=1e-6; % [s]
11
12 RBW=9e3; % [HZ]
13
14 %% Motor Data:
15
16 Phi_Mp = 0.97; % [Wb]
17 Rs = 1.05; % [Ohm]
18 Ls= 40e-3; % [H]
19 Lq = Ls; % [H]
20 Ld = Ls; % [H]
21 PP = 13; % []
22 Ke_rpm = Phi_Mp*sqrt(3)*PP/30*pi*1000; % [Vll/Krpm]
23 Kt_rms = Phi_Mp*1.5*PP*sqrt(2); % [Nm/A]
24
25 %% Control Data:
26
27 Vdc = 700; % [V]
28 Iq_ref = 13; % [A]
29 Id_ref = 0; % [A]
30 Speed = 200; % [rpm]
31
```

```

32 fm=PP*Speed/60; % [Hz]
33
34 modulation = sqrt(3); % 2 for sinusoidal modulation, sqrt(3) for svm
35
36 %% Eq solving (Steady state):
37
38 Vq = Rs*Iq_ref + Phi_Mp*Speed*PP*pi/30 + Ld*Id_ref*Speed*PP*pi/30;
39 Vd = Rs*Id_ref - Lq*Iq_ref*Speed*PP*pi/30;
40 ma = sqrt(Vq^2 +Vd^2)*modulation/Vdc; % Amplitude modulation
    index
41 AP = 1.5*(Vq*Iq_ref + Vd*Id_ref); % Active Power
42 RP = 1.5*(Vq*Id_ref - Vd*Iq_ref); % Reactive Power
43 TP = sqrt(AP*AP + RP*RP); % Total Power
44
45 if Id_ref == 0
46     cosphi = cos(atan2(Vd,Vq)); % cos phi
47 else
48     cosphi = AP/TP; % cos phi
49 end
50
51 Idc = 1.5*sqrt(Vq^2 +Vd^2)*sqrt(Iq_ref^2+Id_ref^2)/Vdc*cosphi;
52 Pdc = Idc*Vdc;
53 P_joule = 1.5*Rs*(Iq_ref*Iq_ref +Id_ref*Id_ref); % Joule losses
    on motor
54 Tm = 1.5*PP*(Phi_Mp+(Ld-Lq)*Id_ref) *Iq_ref; % Produce torque
55 Pm = Tm*Speed/30*pi; % Mechanical
    power
56
57 %% Cable modeling data:
58
59 rho_c = 1.68e-8; % [Ohm*m] Copper resistivity
60 sigma_c=5.98e7; % [S/m] Copper conductivity
61
62 k=1/(3.16e11); % [W/mK] Silicone rubber electrical conductivity
63
64 eps_0=8.85e-12; % [F/m] Vacuum permittivity
65 eps_r_s=4; % [] Silicone rubber relative dielectric
    permittivity
66 eps_r_w=2.5; % [] Wood relative dielectric permittivity
67
68 u_0=1.25663706e-6; % [H/m] Vacuum magnetic permeability
69 u_r=1; % [H/m] Relative permeability in typical coaxial
    cables
70
71 f=30e6; % [Hz]
72 c=3e8; % [m/s]
73 lambda=c/f; % [m]
74 piece_l=lambda/20; % [m]
75

```

```

76 D=0.03;           % [m]
77 h=0.1;           % [m]
78
79 %% DC wires geometry:
80
81 r_out_DC=(15.8e-3)/2;           % [m] => Outer radius (
   sheathing)
82 r_in_DC=(10.5e-3)/2;           % [m] => Inner radius (
   conductor)
83 t_shield_DC=(0.21e-3)/2;       % [m] => Shield thickness
84 r_shield_DC=r_out_DC-0.6e-3-t_shield_DC; % [m] => Shield radius
85
86 total_l_DC=1;   % [m]
87
88 %% DC wires modeling:
89
90 n_of_lines_DC=total_l_DC/piece_l;
91
92 R_wire_DC=0.368e-3;           %
   Conductor resistance [Ohm/m]
93 L_wire_DC=u_0*u_r/(2*pi)*log(r_out_DC/r_in_DC);           %
   Conductor inductance [H/m]
94 C_cs_DC=2*pi*eps_0*eps_r_s/(log(r_shield_DC/r_in_DC));           %
   Conductor-to-shield capacitance [F/m]
95 G_cs_DC=(2*pi*k)/log(r_shield_DC/r_in_DC);           %
   Conductor to shield conductance [S/m]
96
97 R_shield_DC=1/(sigma_c*2*pi*r_shield_DC*t_shield_DC);           %
   Shield self-resistance [Ohm/m]
98 L_shield_DC=u_0*u_r/(2*pi)*log(2*h/(r_shield_DC+t_shield_DC));           %
   Shield self-inductance [H/m]
99
100 L_ab=u_0*u_r/(4*pi)*log(1+4*h^2/(D^2));           % Shield-to-shield
   mutual-inductance [H/m]
101 C_ab=u_0*eps_0*L_ab/(L_shield_DC^2-L_ab^2);           % Shield-to-shield
   mutual-capacitance [F/m]
102
103 C_sn_DC=2*pi*eps_0*eps_r_w/(acosh(h/r_out_DC));           % Shield-
   to-gnd mutual-capacitance [F/m]
104
105 L_sn_conn_DC=(1e-6)*h;           % Inductance
   of shield-to-gnd connection [H] => HP 1nH/mm
106
107 %% Three-phase wires geometry:
108
109 r_out_AC=(5.8e-3)/2;           % [m] => Outer radius (
   sheathing)
110 r_in_AC=(2.8e-3)/2;           % [m] => Inner radius (
   conductor)

```

```

111 t_shield_AC=(0.16e-3)/2; % [m] => Shield thickness
112 r_shield_AC=r_out_AC-0.5e-3-t_shield_AC; % [m] => Shield radius
113
114 total_l_AC=2; % [m]
115
116 %% Three-phase wires modeling:
117
118 n_of_lines_AC=total_l_AC/piece_l;
119
120 R_wire_AC=4.71e-3; %
    Conductor resistance [Ohm/m]
121 L_wire_AC=u_0*u_r/(2*pi)*log(r_out_AC/r_in_AC); %
    Conductor inductance [H/m]
122 C_cs_AC=2*pi*eps_0*eps_r_s/(log(r_shield_AC/r_in_AC)); %
    Conductor to shield capacitance [F/m]
123 G_cs_AC=(2*pi*k)/log(r_shield_AC/r_in_AC); %
    Conductor to shield conductance [S/m]
124
125 R_shield_AC=1/(sigma_c*2*pi*r_shield_AC*t_shield_AC);
    % Shield self-resistance [Ohm/m]
126 L_shield_AC=u_0*u_r/(2*pi)*log(2*h/10/(r_shield_AC+t_shield_AC));
    % Shield self-inductance [H/m]
127
128 L_uv=u_0*u_r/(4*pi)*log(1+4*(h/10)^2/(D^2)); % UV phases
    mutual inductance [H/m]
129 C_uv=u_0*eps_0*L_uv/(L_shield_AC^2-L_uv^2); % UV phases
    mutual capacitance [F/m]
130
131 L_vw=L_uv; % VW phases
    mutual inductance [H/m]
132 C_vw=C_uv; % VW phases
    mutual capacitance [F/m]
133
134 L_uw=2*L_uv; % UW phases
    mutual inductance [H/m]
135 C_uw=2*C_uv; % UW phases
    capacitance [F/m]
136
137 C_sn_AC=2*pi*eps_0/(acosh(h/10/r_out_AC)); % Shield-to-
    gnd mutual-capacitance [F/m]
138
139 L_sn_conn_AC=(1e-6)*h/2; % Inductance
    of shield-to-gnd connection [H] => HP 1nH/mm
140 L_motcase_ref=10e-9; % Inductance
    for motor case to ref connection (hp 1cm)
141 L_invcase_ref=100e-9; % Inductance
    for inv case to ref connection (10cm)
142 A_case=0.122*0.278;

```

```

143 C_invcase_ref=eps_0*eps_r_w*A_case/h;           % Cap
      coupling between inv case and ref (with wood)
144
145 %% FILTER DESIGN
146
147 % The SMPS input impedance is:
148 Rin=Vdc^2/(Pdc)/4;    % [Ohm]
149 Rin_min=Rin/10;      % [Ohm]
150
151 %% Ideal CM filter design:
152
153 f_cut_CM=10e3;
154 w_0_CM=2*pi*f_cut_CM;
155
156 Cy_id=100e-9;
157
158 Lcm_id=(1/w_0_CM)^2*1/(2*Cy_id);
159 coup_k_id=0.95; % Hp
160 L_leak_id=(1-coup_k_id)*Lcm_id;
161
162 %% ideal DM filter design:
163
164 f_cut_DM = 1e4; % [Hz]
165 w_0_DM = f_cut_DM*2*pi; % [rad/s]
166
167 % Cin=200e-6; % [F]
168 % ESR=1.4e-3; % [Ohm]
169 Ldm_id=L_leak_id;
170 Cx_id=1/(w_0_DM^2*2*Ldm_id);
171
172 % Filter output impedance:
173
174 Z0_DM=sqrt(Ldm_id/Cx_id);
175
176 % Damping:
177
178 Cd_id=4*(Cx_id); % [F]
179 Rd_id=sqrt(Ldm_id/Cx_id); %[Ohm]
180
181 %% Real filter parameters
182
183 Cx=1e-6;
184 Cx_ESR=45e-3;
185 Cx_ESL=4.8e-9;
186
187 % Parameters for Cy=47nF:
188 Cy=47e-9;
189 Cy_ESR=90e-3;
190 Cy_ESL=6.65e-9;

```

```
191 |
192 | % Parameters for Cy=68nF:
193 | % Cy=68e-9;
194 | % Cy_ESR=125e-3;
195 | % Cy_ESL=7.4e-9;
196 |
197 | C_damp=4.7e-6;
198 | C_damp_ESR=10e-3;
199 | C_damp_ESL=1.1e-8;
200 | R_damp=3.3;
201 |
202 | Lcm=160e-6;
203 | coup_k=0.98; %Lleak=2uH;
204 | Rdc_choke=0.5e-3;
205 | Rcore_choke=0.8e3;
206 | Cw_choke=108e-12;
```

Appendix B

Tedder system model

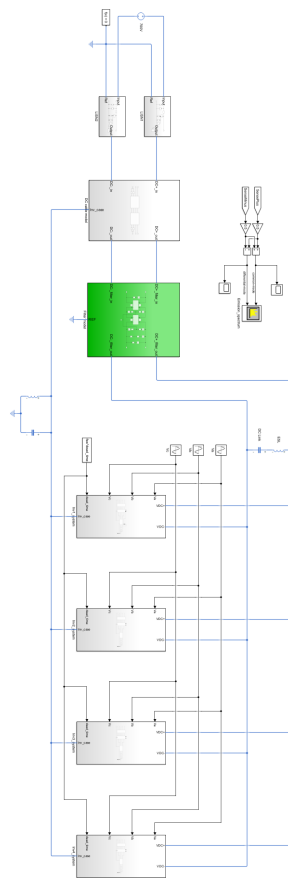


Figure B.1: Model of the tedder system.

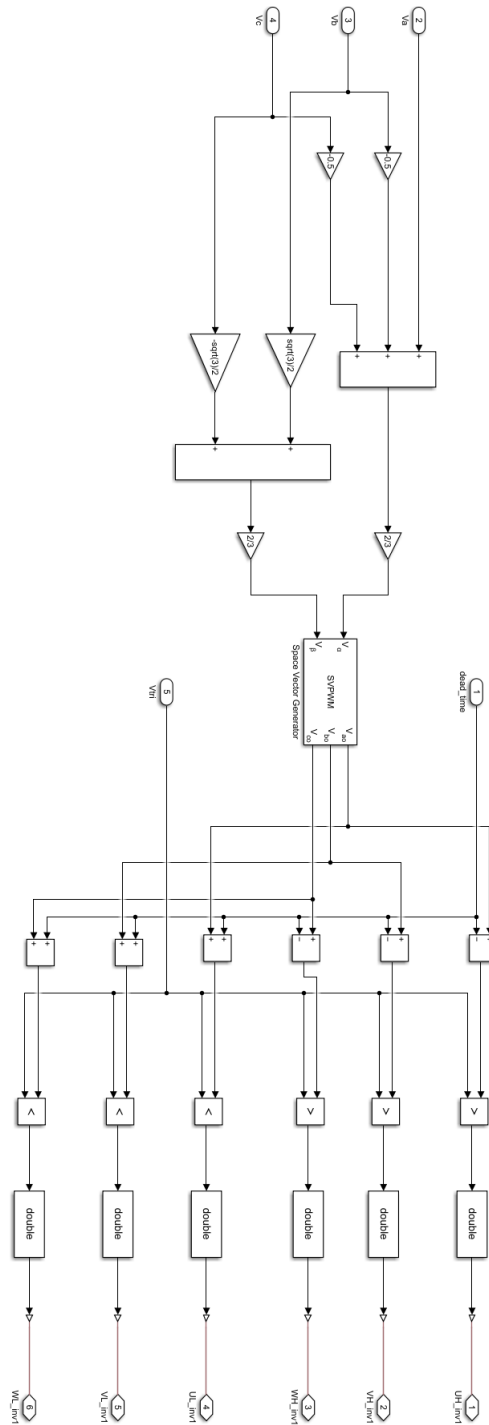


Figure B.2: SVPWM algorithm.

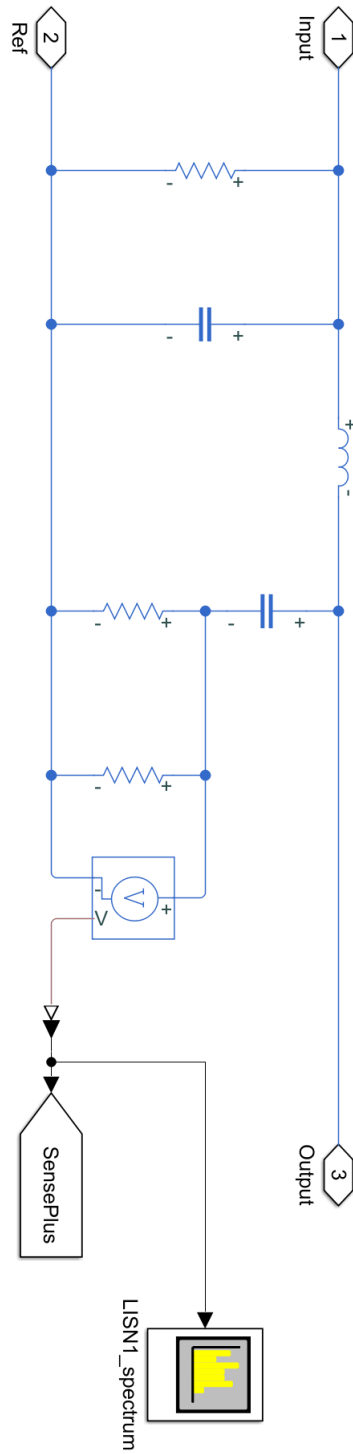


Figure B.3: LISN schematic.

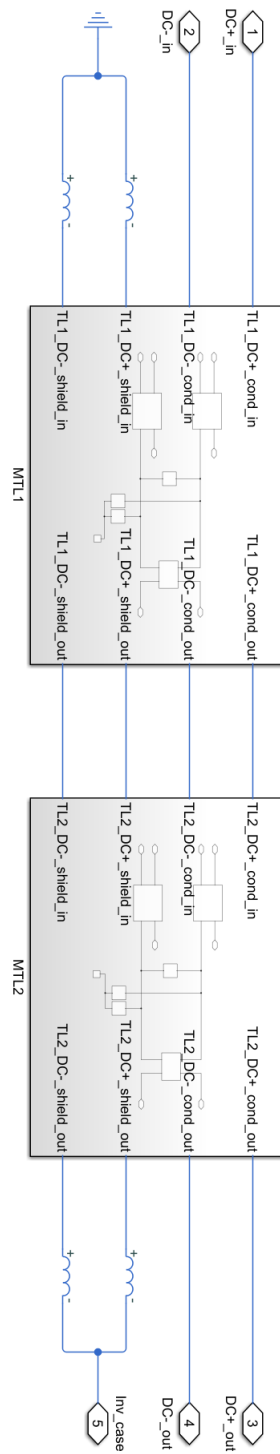


Figure B.4: DC cables model.

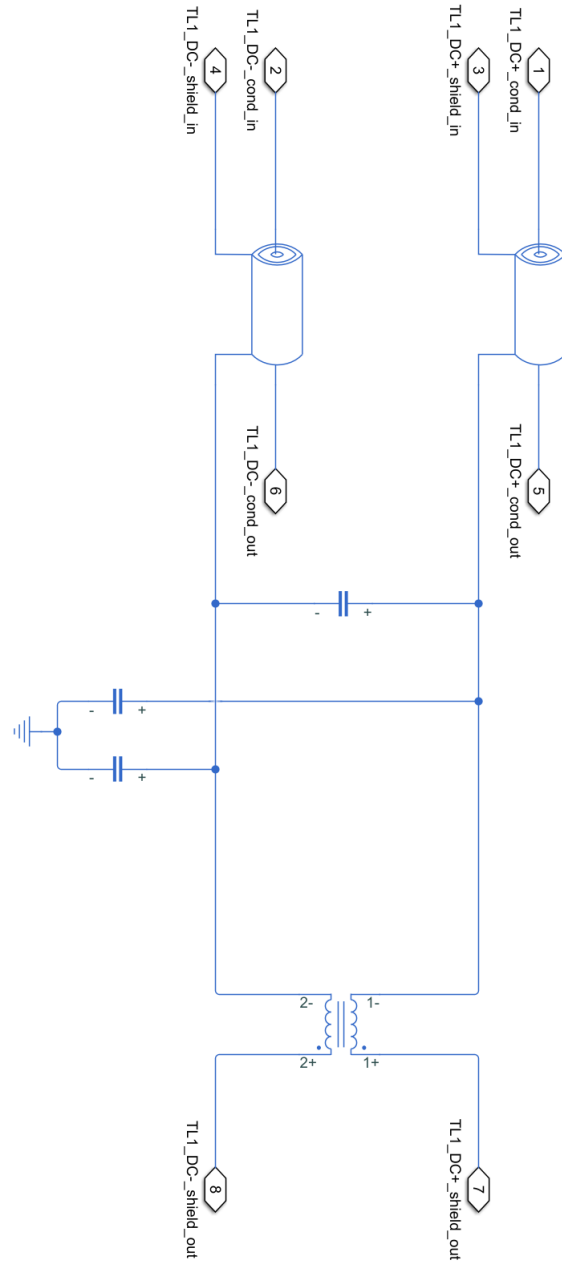


Figure B.5: DC cables line section.

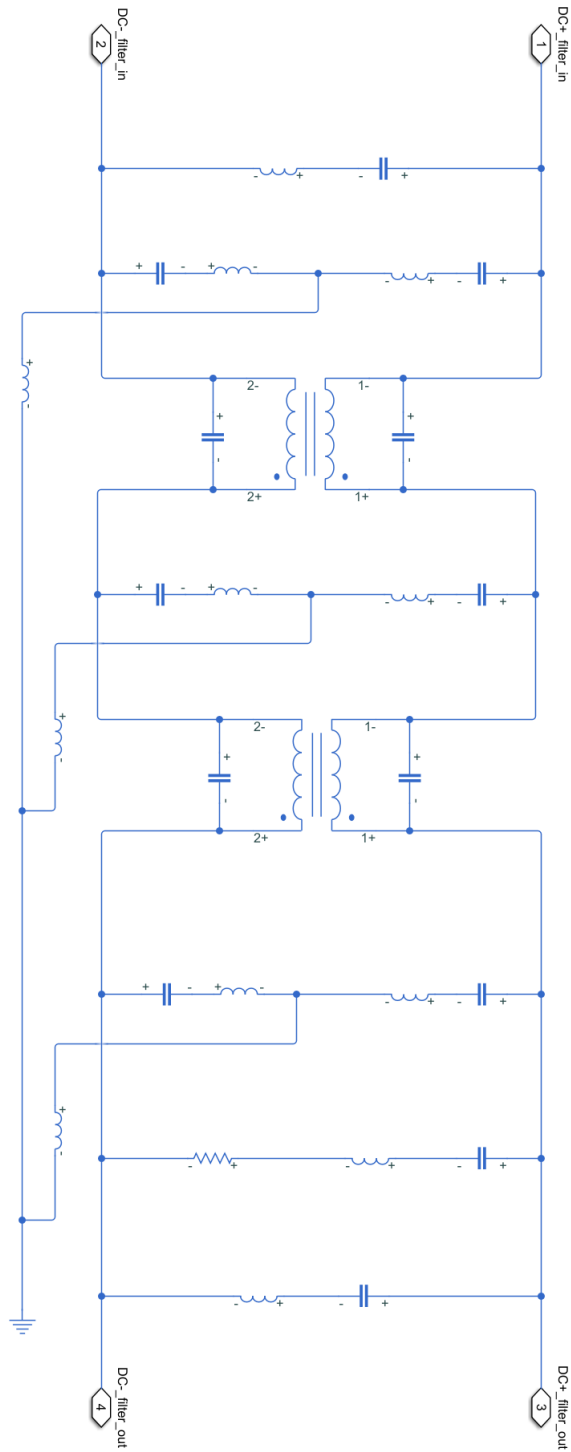


Figure B.6: EMI filter schematic.

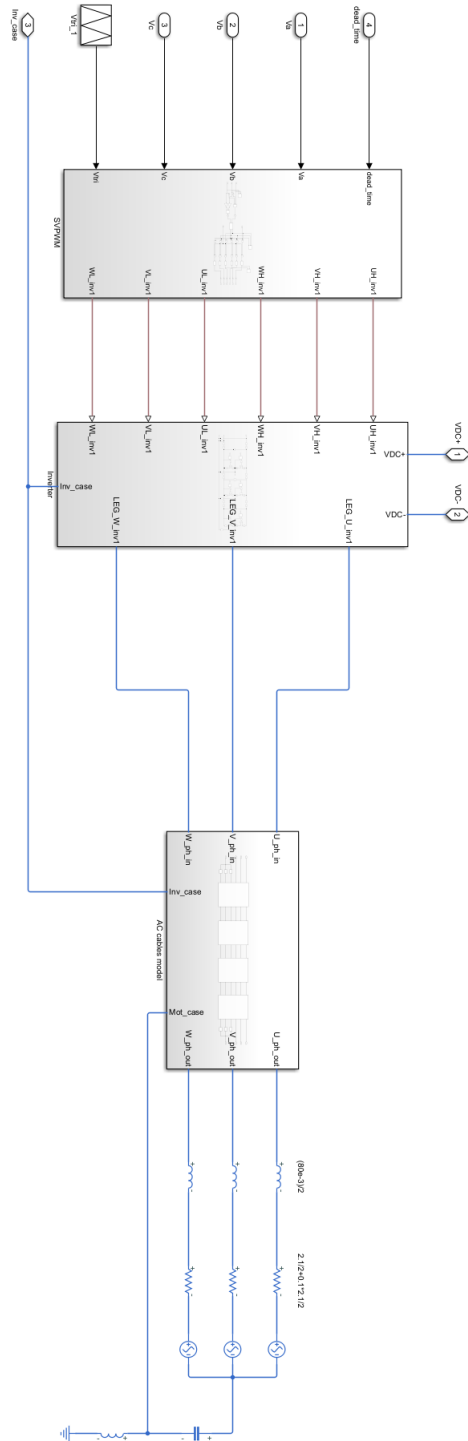


Figure B.7: Single inverter system model.

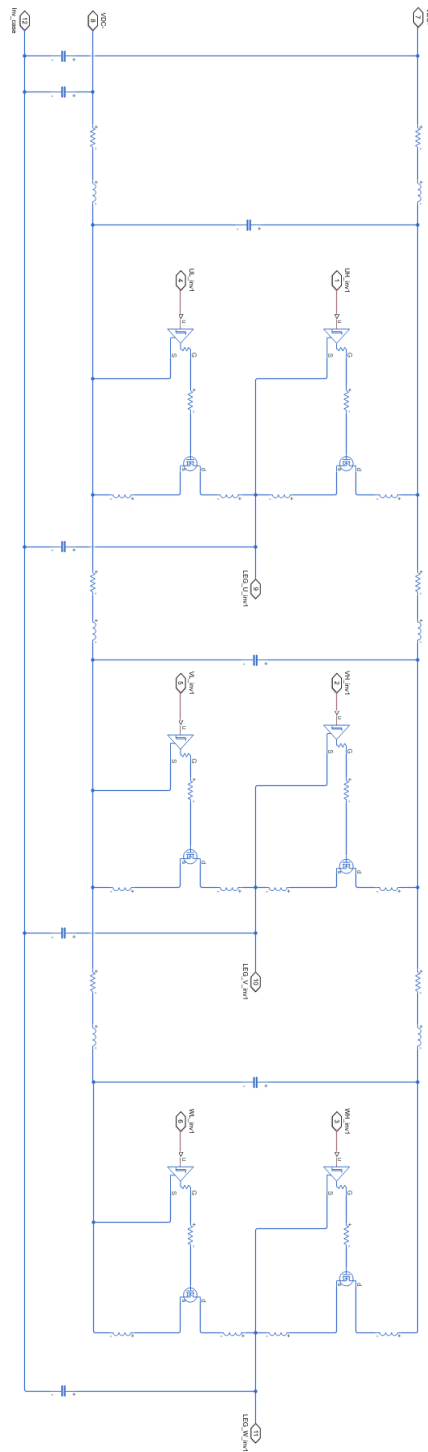


Figure B.8: Single inverter model.

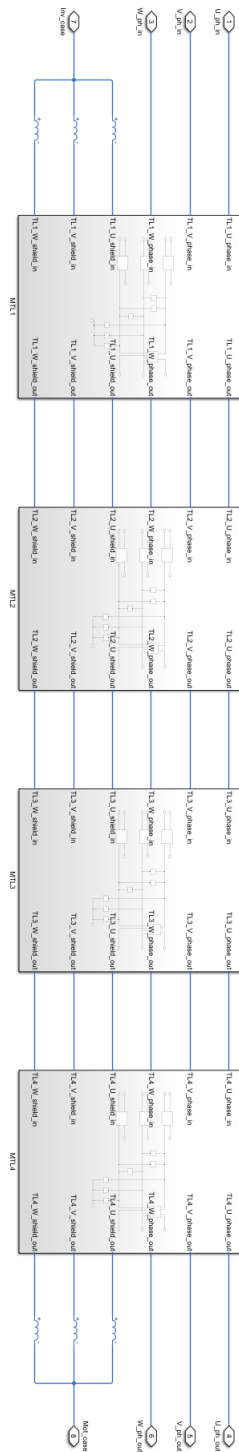


Figure B.9: Three-phase cables model.

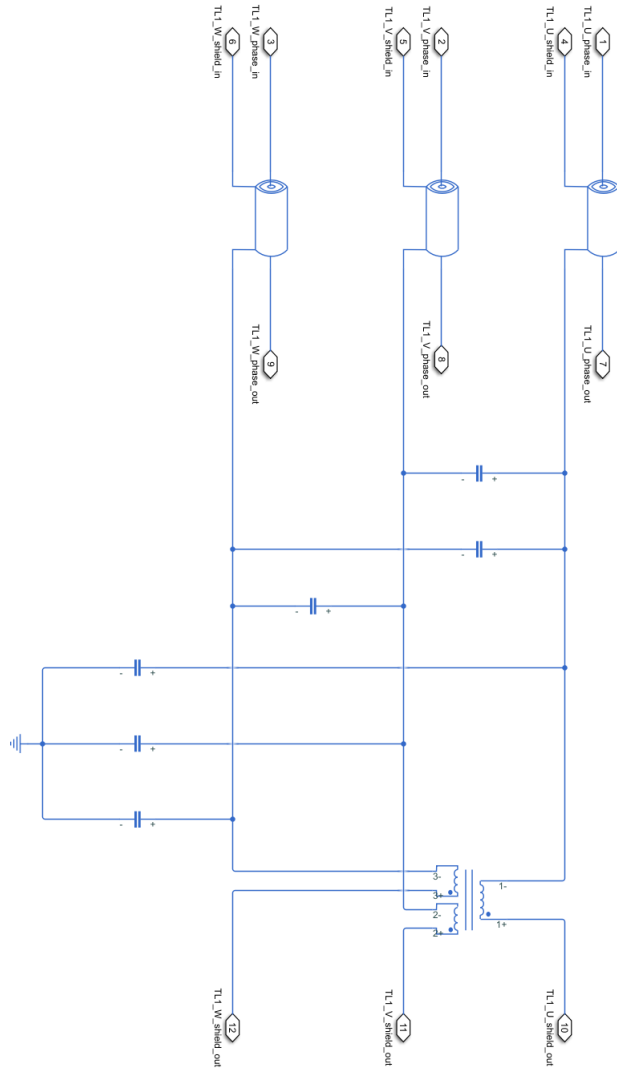


Figure B.10: Three-phase cables line section.

Appendix C

Ditcher data definiton

```
1 clc
2 clear all
3
4 %% Simulation data:
5
6 fmax=30e6;
7 fmin=150e3;
8
9 fsw=10e3;
10 dead_time=1e-6;
11
12 RBW=9e3;
13
14 %% Motor Data:
15
16 Rs = 0.1;           % [Ohm]
17 Lq = 0.003605;     % [H]
18 Ld = 0.003862;     % [H]
19 Ls=(Ld+Lq)/2;     % [H]
20 PP = 4;            % []
21 Ke_rpm = 140*2*sqrt(3); % [Vll/Krpm]
22 Kt_rms = 2.3;      % [Nm/A]
23 Phi_Mp = Kt_rms/(1.5*PP*sqrt(2)); % [Wb]
24
25 %% Control Data:
26
27 Vdc = 700;
28 Iq_ref = 27;
29 Id_ref = 0*sqrt(2);
30 Speed = 3000; % [rpm]
31
```

```

32 fm=PP*Speed/60;
33
34 modulation = sqrt(3); % 2 for sinusoidal modulation, sqrt(3) for svm
35
36 %% Eq solving (Steady state):
37
38 Vq = Rs*Iq_ref + Phi_Mp*Speed*PP*pi/30 + Ld*Id_ref*Speed*PP*pi/30;
39 Vd = Rs*Id_ref - Lq*Iq_ref*Speed*PP*pi/30;
40 ma = sqrt(Vq^2 +Vd^2)*modulation/Vdc; % modulation with space
    vector
41 AP = 1.5*(Vq*Iq_ref + Vd*Id_ref); % Active Power
42 RP = 1.5*(Vq*Id_ref - Vd*Iq_ref); % Reactive Power
43 TP = sqrt(AP*AP + RP*RP); % Total Power
44
45 if Id_ref == 0
46     cosphi = cos(atan2(Vd,Vq)); % cos phi
47 else
48     cosphi = AP/TP; % cos phi
49 end
50
51 Idc = 1.5*sqrt(Vq^2 +Vd^2)*sqrt(Iq_ref^2+Id_ref^2)/Vdc*cosphi;
52 Pdc = Idc*Vdc;
53 P_joule = 1.5*Rs*(Iq_ref*Iq_ref +Id_ref*Id_ref); % joule losses
    on motor
54 Tm = 1.5*PP*(Phi_Mp+(Ld-Lq)*Id_ref) *Iq_ref; % Produce torque
55 Pm = Tm*Speed/30*pi; % Mechanical
    power
56
57
58 %% Cable modeling data:
59
60 rho_c = 1.68e-8; % [Ohm*m] Copper resistivity
61 sigma_c=5.98e7; % [S/m] Copper conductivity
62
63 k=1/(3.16e11); % [W/mK] Silicone rubber electrical conductivity
64
65 eps_0=8.85e-12; % [F/m] Vacuum permittivity
66 eps_r_s=4; % [] Silicone rubber relative permittivity
67 eps_r_w=2.5; % [] Wood relative dielectric permittivity
68
69 u_0=1.25663706e-6; % [H/m] Vacuum magnetic permeability
70 u_r=1; % [H/m] Relative permeability in typical coaxial
    cables
71
72 f=30e6; % [Hz]
73 c=3e8; % [m/s]
74 lambda=c/f; % [m]
75 piece_l=lambda/20; % [m]
76

```

```

77 D=0.03;           % [m] => Line-to-line distance (HP)
78 h=0.1;           % [m] => Line-to-gnd distance
79
80 %% DC wires geometry:
81
82 r_out_DC=(15.8e-3)/2;           % [m] => Outer radius (
      screen->sheathing)
83 r_in_DC=(10.5e-3)/2;           % [m] => Inner radius (
      conductor)
84 t_shield_DC=(0.21e-3)/2;       % [m] => Shield thickness
85 r_shield_DC=r_out_DC-0.6e-3-t_shield_DC; % [m] => Shield radius
86
87 total_l_DC=1;           % [m]
88
89 %% DC wires modeling:
90
91 n_of_lines_DC=total_l_DC/piece_l;
92
93 R_wire_DC=0.368e-3;           %
      Conductor resistance [Ohm/m]
94 L_wire_DC=u_0*u_r/(2*pi)*log(r_out_DC/r_in_DC);           %
      Conductor inductance [H/m]
95 C_cs_DC=2*pi*eps_0*eps_r_s/(log(r_shield_DC/r_in_DC));           %
      Conductor-to-shield capacitance [F/m]
96 G_cs_DC=(2*pi*k)/log(r_shield_DC/r_in_DC);           %
      Conductor to shield conductance [S/m]
97
98 R_shield_DC=1/(sigma_c*2*pi*r_shield_DC*t_shield_DC);           %
      Shield self-resistance [Ohm/m]
99 L_shield_DC=u_0*u_r/(2*pi)*log(2*h/(r_shield_DC+t_shield_DC));           %
      Shield self-inductance [H/m]
100
101 L_ab=u_0*u_r/(4*pi)*log(1+4*h^2/(D^2));           % Shield-to-
      shield mutual-inductance [H/m]
102 C_ab=u_0*eps_0*eps_r_s*L_ab/(L_shield_DC^2-L_ab^2);           % Shield-
      to-shield mutual-capacitance [F/m]
103
104 C_sn_DC=2*pi*eps_0*eps_r_s/(acosh(h/r_out_DC));           % Shield-
      to-gnd mutual-capacitance [F/m]
105
106 L_sn_conn_DC=(1e-6)*h;           % Inductance
      of shield-to-gnd connection [H] => HP 1nH/mm
107
108 %% Three-phase wires geometry:
109
110 r_out_AC=(10.2e-3)/2;           % [m] => Outer radius (
      screen->sheathing)
111 r_in_AC=(5.8e-3)/2;           % [m] => Inner radius (
      conductor)

```

```

112 t_shield_AC=(0.16e-3)/2; % [m] => Shield thickness
113 r_shield_AC=r_out_AC-0.6e-3-t_shield_AC; % [m] => Shield radius
114 total_l_AC=1.5; % [m]
115
116 %% Three-phase wires modeling:
117
118 n_of_lines_AC=total_l_AC/piece_l;
119
120 R_wire_AC=4.71e-3; %
    Conductor resistance [Ohm/m]
121 L_wire_AC=u_0*u_r/(2*pi)*log(r_out_AC/r_in_AC); %
    Conductor inductance [H/m]
122 C_cs_AC=2*pi*eps_0*eps_r_s/(log(r_shield_AC/r_in_AC)); %
    Conductor to shield capacitance [F/m]
123 G_cs_AC=(2*pi*k)/log(r_shield_AC/r_in_AC); %
    Conductor to shield conductance [S/m]
124
125 R_shield_AC=1/(sigma_c*pi*(r_out_AC^2-r_in_AC^2)); %
    Shield self-resistance [Ohm/m]
126 L_shield_AC=u_0*u_r/(2*pi)*log(2*h/10/(r_shield_AC+t_shield_AC));
    % Shield self-inductance [H/m]
127
128 L_uv=u_0*u_r/(4*pi)*log(1+4*(h/10)^2/(D^2)); % UV
    phases mutual inductance [H/m]
129 C_uv=u_0*eps_0*eps_r_s*L_uv/(L_shield_AC^2-L_uv^2); % UV phases
    mutual capacitance [F/m] =>
130
131 L_vw=L_uv; % VW phases
    mutual inductance [H/m]
132 C_vw=C_uv; % VW phases
    mutual capacitance [F/m]
133
134 L_uw=2*L_uv; % UW phases
    mutual inductance [H/m]
135 C_uw=2*C_uv; % UW phases
    capacitance [F/m]
136
137 C_sn_AC=2*pi*eps_0*eps_r_s/(acosh(h/10/r_out_AC)); % Shield
    -to-gnd mutual-capacitance [F/m]
138
139 L_sn_conn_AC=(1e-6)*h/2; % Inductance
    of shield-to-gnd connection [H] => HP 1nH/mm
140 L_motcase_ref=10e-9; % Inductance
    for motor case to ref connection (hp 1cm)
141 L_invcase_ref=100e-9; % Inductance
    for inv case to ref connection (10cm)
142 A_case=0.122*0.278;
143 C_invcase_ref=eps_0*eps_r_w*A_case/h; % Cap
    coupling between inv case and ref (with wood)

```

```
144
145 %% Real filter parameters
146
147 Cx=1e-6;
148 Cx_ESR=45e-3;
149 Cx_ESL=4.8e-9;
150
151 % Parameters for Cy=47nF:
152 Cy=47e-9;
153 Cy_ESR=90e-3;
154 Cy_ESL=6.65e-9;
155
156 % Parameters for Cy=68nF:
157 % Cy=68e-9;
158 % Cy_ESR=125e-3;
159 % Cy_ESL=7.4e-9;
160
161 C_damp=4.7e-6;
162 C_damp_ESR=10e-3;
163 C_damp_ESL=1.1e-8;
164 R_damp=3.3;
165
166 Lcm=160e-6;
167 coup_k=0.98; %Lleak=2uH;
168 Rdc_choke=0.5e-3;
169 Rcore_choke=0.8e3;
170 Cw_choke=108e-12;
```


Appendix D

Ditcher system model

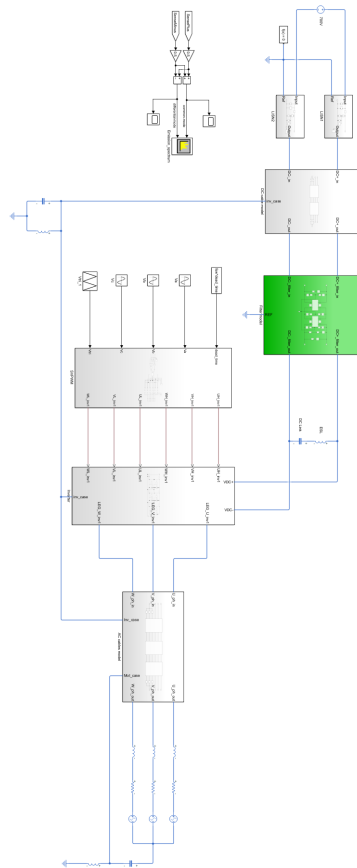


Figure D.1: Model of the ditcher system.

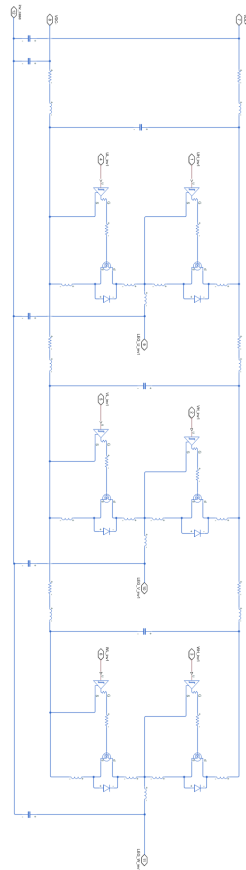


Figure D.2: Inverter model.

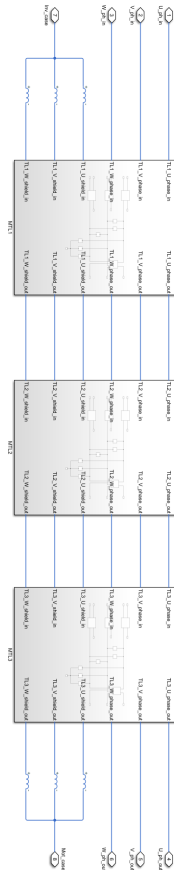


Figure D.3: Three-phase cables model.

Bibliography

- [1] Jaroslaw Luszcz. *High Frequency Conducted Emission in AC Motor Drives Fed by Frequency Converters*. Hoboken, New Jersey: JohnWiley & Sons, Inc., 2006 (cit. on pp. 2, 6, 13, 15, 16, 19).
- [2] *Uniform provisions concerning the approval of vehicles with regard to electromagnetic compatibility*. Electromagnetic compatibility regulation. Economic Commission for Europe of the United Nations (UN/ECE), Nov. 2019 (cit. on pp. 2, 9–11).
- [3] Clayton R. Paul. *Introduction to Electromagnetic Compatibility*. Hoboken, NJ: John Wiley & Sons, Inc., 2006 (cit. on pp. 5, 97).
- [4] Keysight Technologies. «Spectrum Analysis Basics». In: (Oct. 2020) (cit. on p. 12).
- [5] F. Musolino. «Advanced Electronic Drive - Course Notes». In: (Sept. 2020) (cit. on p. 23).
- [6] Yngve Solbakken. «Space Vector PWM Intro». In: (May 2017) (cit. on p. 27).
- [7] Emil Rachev and Vladislav Petrov. «DC link capacitor selection for DC-DC converters». In: *2020 12th Electrical Engineering Faculty Conference (BulEF)*. 2020, pp. 1–5. DOI: 10.1109/BulEF51036.2020.9326085 (cit. on p. 27).
- [8] *Metallized Polypropylene Film Capacitors (MKP)*. Series B32774 ... B32778. TDH. June 2018 (cit. on pp. 28, 29).
- [9] Rudy Ramos. «Selecting Film or Electrolytic Capacitors for Power-Conversion Circuits». In: (Aug. 2018) (cit. on p. 27).
- [10] Wolfspeed - Cree company. «Comparing Silicon Carbide MOSFETs to Si MOSFETs». In: (Nov. 2019) (cit. on p. 29).
- [11] *Silicon Carbide Power MOSFET*. C3MTM MOSFET Technology. Cree. Apr. 2019 (cit. on pp. 30, 51–53).

- [12] Ana Carolina Moreira, Daniel Cesar Piccoli, Júlio Cesar Lopes de Oliveira, Luiz Fernando Henning, and Rodrigo Jose Piontkewicz. «Comparative study of RC snubber configurations in switching circuits». In: *2019 IEEE 15th Brazilian Power Electronics Conference and 5th IEEE Southern Power Electronics Conference (COBEP/SPEC)*. 2019, pp. 1–6. DOI: 10.1109/COBEP/SPEC44138.2019.9065774 (cit. on p. 30).
- [13] Rahul Chokhawala Yi Zhang Saed Sobhani. «Snubber Considerations for IGBT Applications». In: (July 2019) (cit. on p. 30).
- [14] Mateo Begue. «External Gate Resistor Design Guide for Gate Drivers». In: (May 2018) (cit. on p. 31).
- [15] *EasyDUAL module with CoolSiC™ Trench MOSFET and PressFIT/NTC/-TIM*. FF6MR12W2M1P-B11. Infineon Technologies AG. Aug. 2019 (cit. on pp. 31, 32, 90).
- [16] Hao-Chieh Yeh and Sheng-Ming Yang. «Phase Inductance and Rotor Position Estimation for Sensorless Permanent Magnet Synchronous Machine Drives at Standstill». In: *IEEE Access* 9 (2021), pp. 32897–32907. DOI: 10.1109/ACCESS.2021.3060774 (cit. on p. 40).
- [17] *Spectrum Analysis Basics*. Part 3: Detector Types. Keysight. Aug. 2020 (cit. on p. 46).
- [18] Wikipedia contributors. *Welch's method* — *Wikipedia, The Free Encyclopedia*. [Online; accessed 2-November-2021]. 2021. URL: https://en.wikipedia.org/w/index.php?title=Welch%27s_method&oldid=1028726658 (cit. on p. 46).
- [19] Wikipedia contributors. *Window function* — *Wikipedia, The Free Encyclopedia*. [Online; accessed 2-November-2021]. 2021. URL: https://en.wikipedia.org/w/index.php?title=Window_function&oldid=1051944138 (cit. on p. 47).
- [20] *UCC21750-Q1 10-A Source/Sink Reinforced Isolated Single Channel Gate Driver for SiC/IGBT with Active Protection, Isolated Analog Sensing and High-CMTI*. 2. Texas Instrument. Mar. 2020 (cit. on p. 51).
- [21] *Wires and Cables for automotive applications*. Coroplast (cit. on pp. 56, 57, 59).
- [22] Thorne and Derrick International. «SVL's Sheath Voltage Limiters for Protection of MV HV Cables». In: (Apr. 2019) (cit. on p. 57).
- [23] F. Canavero. «Advanced Design for Signal Integrity and Compliance - Course Notes». In: (Sept. 2018) (cit. on p. 60).
- [24] EMI analyst software. *EMI software toolbox*. URL: <https://www.emisoftwar.e.com/toolbox/> (cit. on p. 61).

-
- [25] Wenzhi Zhou, Mohamed S. Diab, and Xibo Yuan. «Mitigation of Motor Overvoltage in SiC-Device-Based Drives using a Soft-Switching Inverter». In: *2020 IEEE Energy Conversion Congress and Exposition (ECCE)*. 2020, pp. 662–669. DOI: 10.1109/ECCE44975.2020.9236099 (cit. on p. 62).
- [26] Lei Xing and Jian Sun. «Motor drive system EMI reduction by asymmetric interleaving». In: *2010 IEEE 12th Workshop on Control and Modeling for Power Electronics (COMPEL)*. 2010, pp. 1–7. DOI: 10.1109/COMPEL.2010.5562372 (cit. on pp. 75, 77, 78).
- [27] G. Grandi, D. Casadei, and U. Reggiani. «Common- and differential-mode HF current components in AC motors supplied by voltage source inverters». In: *IEEE Transactions on Power Electronics* 19.1 (2004), pp. 16–24. DOI: 10.1109/TPEL.2003.820564 (cit. on p. 84).
- [28] Jun-Kyu Park, Se-Hyun Rhyu, and Jin Hur. «Shaft-to-frame voltage mitigation method by changing winding-to-rotor parasitic capacitance of IPMSM». In: *2017 IEEE Energy Conversion Congress and Exposition (ECCE)*. 2017, pp. 3571–3576. DOI: 10.1109/ECCE.2017.8096635 (cit. on p. 84).
- [29] Norbert Doerry and John Amy. «Medium Voltage DC Common Mode Current Control and Grounding». In: *Naval Engineers Journal* 130 (June 2018), pp. 85–104 (cit. on p. 84).
- [30] H.W. Ott. *Electromagnetic compatibility engineering*. Wiley, 2009 (cit. on pp. 84, 85, 97, 98, 113, 114).
- [31] *EN 61140*. CEI 0-13. Oct. 2018 (cit. on p. 88).
- [32] *Industrial IGBT Modules Explanation of Technical Information*. Infineon. Sept. 2011 (cit. on p. 91).
- [33] Mark J. Nave. *Power Line Filter Design for Switched-Mode Power Supplies*. Van Nostrand Reinhold, 2003 (cit. on p. 94).
- [34] Maksimović D. Erickson R.W. «Fundamentals of Power Electronics». In: *Basic Magnetism Theory*. 2020, pp. 409–505. DOI: https://doi.org/10.1007/978-3-030-43881-4_10 (cit. on pp. 95, 96).
- [35] Wikipedia contributors. *Toroidal inductors and transformers* — *Wikipedia, The Free Encyclopedia*. [Online; accessed 18-November-2021]. 2021. URL: https://en.wikipedia.org/w/index.php?title=Toroidal_inductors_and_transformers&oldid=1016198070 (cit. on p. 98).
- [36] Inc. Coil Winding Specialist. «Application Notes: How To Select And Use Ferrite / Nanocrystalli». In: (2013) (cit. on p. 98).
- [37] Nick Davis. *Safety Capacitors First: Class-X and Class-Y Capacitors*. 2019. URL: <https://www.allaboutcircuits.com/technical-articles/safety-capacitor-class-x-and-class-y-capacitors/> (cit. on p. 99).

- [38] *Electrically propelled road vehicles — Safety specifications*. Protection of persons against electric shock. INTERNATIONAL STANDARD, Dec. 2011 (cit. on p. 99).
- [39] R. David Middlebrook. «Input filter considerations in design and application of switching regulators.» In: 1976 (cit. on p. 100).
- [40] National Semiconductor Corporation. «Input Filter Design for Switching Power Supplies». In: 2010 (cit. on p. 100).
- [41] *Common-mode Chokes*. RB series. Schaffner. Oct. 2020 (cit. on p. 103).
- [42] *EMI Suppression Capacitors (MKP)*. B32912*5 ... B32918*5. TDK. June 2020 (cit. on p. 104).
- [43] Shuo Wang, F.C. Lee, D.Y. Chen, and W.G. Odendaal. «Effects of parasitic parameters on EMI filter performance». In: *IEEE Transactions on Power Electronics* 19.3 (2004), pp. 869–877. DOI: 10.1109/TPEL.2004.826527 (cit. on p. 105).